"El saber de mis hijos
hará mi grandeza"

UNIVERSIDAD DE SONORA
División de Ciencias Exactas y Naturales
Departamento de Investigación en Física

Modeling of Radiosensitization Effect in Photon Irradiated Cells with Embedded High-Z Nanoparticles

Thesis to Obtain the Degree of
Doctor of Science (Physics)

Presented by
Wilmer Ferney Melo Bernal

Thesis Director
Dr. Valery Chernov

Hermosillo, Sonora, México noviembre de 2022

Abstract

Radiotherapy is one of the most important methods of cancer treatment. Despite that, radiotherapy possesses one major limitation: ionizing radiation does not discriminate between normal tissue and malignant tissue, which results in high morbidity of healthy tissue near the tumor. Combining radiotherapy with high-Z nanoparticle (NP) radiosensitizers provides great opportunities for increasing treatment efficiency and widening the therapeutic window. In order to predict the radiosensitization effect of NPs, a modification of the local effect model, in which the energy deposition from NPs is assessed by Monte Carlo (MC) radiation transport codes, has been employed in the past. In this thesis, a combined framework that splits the consideration of the radiosensitization effect into two steps is developed in order to have an approach to the biological outcomes of the radiation treatment assisted with high-Z NPs.

The first step is the evaluation of the radial dose distribution (RDD) around a single NP ionized by a photon beam with a given energy spectrum using MC simulation. MC simulations were performed using TOPAS (TOol for PArticle Simulation), which is based on Geant 4, a toolkit for the simulation of the passage of particles through matter. To simulate the RDD, single spherical gold NPs of various diameters suspended in water were irradiated with mono-energetic and poly-energetic photon beams, and produced secondary electrons were scored at the NP surface as phase space. After that, the scored electron spectra were used to evaluate the deposited doses in water-like tissue around irradiated NPs, which, in turn, were fitted by a power law function.

In the second stage, an analytical approach based on the local effect model and the simulated RDDs was used to evaluate the average dose and the average number of lethal lesions in a cell target due to a set of irradiated NPs. The general expressions (in the integral form) for the average number of lesions and the survival probability of irradiated cells loaded with high-Z NPs were derived. For the case of a spherical cell target and the power law RDD the integrals were taken using the Maple package and the explicit analytical expressions describing the average doses and the average of the squared doses per one ionized NP located at a given distance from the target center were derived. The expressions contain only four parameters: the target (nucleus) radius and the other three related to the power law approximation of the NP RDDs, which are the NP radius, the dose per one ionization at the NP surface, and two parameters describing the power law RDD. Integration of these expressions over a cell volume with a given distribution of NPs allowed us to

derive an expression from calculating the survival probability and related metrics quantifying the biological effects (relative biological effectiveness and other similar).

The derived expressions were applied to calculate the survival curves and relative biological effectiveness for a culture of spherical cells loaded with gold NPs and irradiated with monoenergetic photons of 10 - 150 keV. The proposed framework provides a practical alternative to time-consuming MC simulations, enabling the assessment of the response of cell cultures to an irradiation treatment assisted with NPs for a wide variety of cell geometries, NP distributions, and irradiation schemes. The validation of the proposed model was performed, evaluating the dependence of RBE on the GNP radius and the variation of RBE with the photon energy. The results present an excellent agreement with results reported in the literature, allowing a successful approach to predicting the radiosensitization effect of irradiated high-Z NPs on human cancer cells.

Resumen

La radioterapia es uno de los métodos más importantes en el tratamiento de cáncer. Sin embargo, la radioterapia posee una gran limitante dado que la radiación ionizante no discrimina entre el tejido sano (normal) y el tejido maligno, lo que resulta en una gran afección del tejido sano alrededor del tumor. La combinación de la radioterapia con nanopartículas (NP) de elementos gran número atómico, a manera de sensibilizador a la radiación proporciona grandes oportunidades de aumentar la eficiencia de los tratamientos y de ampliar la ventana terapéutica. Con el objetivo de predecir los efectos de sensibilización a la radiación de las NPs una modificación del modelo de efecto local (LEM por sus siglas en inglés), en el que la energía depositada por las NPs se evalúa mediante simulaciones de transporte de radiación Monte Carlo (MC) se ha empleado en el pasado. En esta tesis, desarrollamos un marco que divide la consideración de los efectos sensibilizadores de la radiación en dos pasos buscando así una aproximarnos a los resultados biológicos de los tratamientos de radiación asistidos con NPs.

El primer paso es la evaluación de la distribución radial de la dosis (RDD) alrededor de una NP individual, ionizada por un haz de fotones con un espectro energético determinado usando una simulación MC. Las simulaciones MC se realizaron usando TOPAS (TOol for PArticle Simulation), el cual se basa en Geant4, una herramienta para la simulación del paso de partículas a través de la materia. Para simular la RDD, una nanopartícula individual de diferentes radios suspendida en agua fue irradiada con haces de fotones monoenergéticos y poli energéticos, y los electrones secundarios producidos se registraron al cruzar la superficie de la NP como un espacio de fase (un tamaño de NP y haz a la vez). A continuación, el espectro de electrones registrados se usó para evaluar la dosis depositada en tejido (similar a agua) alrededor de las NPs irradiadas. Estas RDD fueron posteriormente ajustadas a funciones con dependencia en forma potencia.

En la segunda etapa, usamos una aproximación analítica basado en el modelo de efecto locar (LEM) y las RDD simuladas para evaluar la dosis media y el número medio de lesiones letales debidas a las NPs en un grupo de células irradiadas. Derivando así las expresiones generales (en forma de integrales) para el número medio de lesiones y la probabilidad de supervivencia de

células irradiadas con NPs embebidas. Se evaluaron las integrales usando el paquete de Maple para el caso en el que el objetivo de la radiación sea una célula esférica y la RDD sea la propuesta en la función de potencia y se derivaron las expresiones analíticas explicitas que describen la dosis media y la dosis media cuadrada para una NP ionizada a una distancia específica del centro del objetivo. Las expresiones contienen solo cuatro parámetros: el radio del objetivo (núcleo celular) y otros tres parámetros relacionados con la aproximación a una función con dependencia potencial de la RDD al redor de la NP, los cuales son el radio de la NP, la dosis evaluada en la superficie de la NP debida a una sola ionización y dos parámetros que describen la función de potencia de las RDD. La integración de estos parámetros sobre el volumen celular con una distribución especifica de NPs nos permite derivar la expresión para calcular la probabilidad de supervivencia y otras métricas relacionadas para cuantificar los efectos biológicos (Eficiencia biológica relativa y otras similares).

Las expresiones derivadas se aplicaron al cálculo de las curvas de supervivencia y la eficiencia biológica relativa para un cultivo de células esféricas con NP embebidas e irradiadas con fotones monoenergéticos de 10 – 150 keV. El marco propuesto proporciona una alternativa practica a las simulaciones MC, las cuales demandan de tiempo considerable, permitiendo la evaluación de la respuesta de cultivos celulares a un tratamiento de irradiación asistida con NPs para una amplia variedad de geometrías celulares, distribución de NP y esquemas de irradiación. La validación del modelo propuesto se realizó evaluando la dependencia de la eficiencia biológica relativa (RBE por sus siglas en inglés) en el radio de las nanopartículas de oro (GNP) y la variación de la RBE con la energía del haz de fotones. Los resultados presentan una excelente concordancia con los resultados reportados en la literatura, permitiendo una buena aproximación a la predicción de los efectos de sensibilización a la radiación generados por las NPs de gran número atómico en células cancerígenas humanas.

Contents

Acknowledgments

I would like to acknowledge and give my warmest thanks to my advisor, Dr. Valery Chernov, who made this work possible. His guidance, hard work, and thoughtful advice carried me through all the stages of constructing this thesis. I would also like to thank the DIFUS, its director, coordinator, and researchers, thank you for the opportunity that you entrusted me to access grad school.

Finally, I acknowledge the financial support from CONACyT student fellowships.

Original publications, conference presentations, and participation in scientific projects

The publications based on the results presented in the thesis are the following:

Melo-Bernal, W., Chernov, V., Chernov, G., Barboza-Flores, M., 2018. Nanoscale dose deposition in cell structures under X-ray irradiation treatment assisted with nanoparticles: An analytical approach to the relative biological effectiveness. Applied Radiation and Isotopes, Proceedings of the XVI International Symposium on Solid State Dosimetry 138, 50–55. https://doi.org/10.1016/j.apradiso.2017.05.020

Melo-Bernal, W., Chernov, G., Barboza-Flores, M., Chernov, V., 2021. Quantification of the radiosensitization effect of high-Z nanoparticles on photon irradiated cells: combining Monte Carlo simulations and an analytical approach to the local effect model. Phys. Med. Biol. https://doi.org/10.1088/1361-6560/abfce4

The main results of the thesis were presented at the following international scientific conferences:

XVI International Symposium on Solid State Dosimetry, Tuxtla Gutierrez, Chiapas, September 24 -28, 2016

W. Melo-Bernal, V. Chernov, G. Chernov, M. Barboza-Flores. Nanoscale dose deposition in cell structures under X-ray irradiation treatment assisted with Nanoparticles for a range of elements. An analytical approach to cell survival

LIX Congreso Nacional de Física, Leon, Guanajuato, October 2 – 7, 2016.

G. Chernov, M. Barboza-Flores, R. Carillo-Torres, J. L. Ibarra-Valdez, T. Medrano-Pesqueira, W. Melo-Bernal, V. Chernov. 632 nm laser heating of gold nanoparticles in water: experiment and computer simulations

Nano Word Conference, San Francisco, CA, April 23 – 25, 2018.

W. Melo-Bernal, M. Barboza-Flores, V. Chernov. Survival fraction and RBE for x-ray irradiated MDA-MB-231 cell culture with intracellular Gold Nanoparticles: An analytical framework for the assessment of the cell survival.

List of abbreviations

Abbreviation	Meaning
DEF	Dose enhancement factor
GNP(s)	Gold nanoparticle(s)
LEM	Local effect model
LQ	Linear-quadratic
MID	Mean inactivation dose
NP(s)	Nanoparticle(s)
RBE	Relative biological effectiveness
RDD	Radial dose distribution
SER	Sensitizer enhancement ratio
TOPAS	TOol for PArticle Simulation, a software project which extends the Geant4 toolkit

CHAPTER 1

Introduction to the thesis

1.1 Background and motivation

Radiotherapy is one of the most important methods of cancer treatment (Delaney and Barton, 2015). Despite that, radiotherapy possesses one major limitation: ionizing radiation does not discriminate between normal tissue and malignant tissue, which results in high morbidity of healthy tissue in the vicinity of the tumor. In particular, normal tissue damage cannot be completely avoided because normal and malignant tissue have almost the same X-rays and gamma rays absorption characteristics. The doses necessary to achieve tumor control usually overlap with those that can cause complications (Beasley et al., 2005). Thus, treating a tumor with radiotherapy must consider the balance between damage to the tumor and damage to healthy tissue.

A combination of radiotherapy with radiosensitizers provides great opportunities for increasing treatment efficiency and widening the therapeutic window. In particular, high atomic number (Z) nanoparticles (NPs) have proven to be promising radiosensitizers because they can effectively absorb, scatter, and emit radiation energy (Wang et al., 2018). The concept of using high-Z materials for dose enhancement in cancer treatment by radiotherapy was advanced over 40 years ago by Matsudaira et al. 1980, who found radio enhancing effect of iodine on cultured cells. Since then, there have been many studies on the application of high-Z NPs for radiotherapy. The most studied high-*Z* material is gold due to its high atomic number (Z = 79,) biocompatibility, and enhanced permeation into the tumor tissue (Kwatra et al., 2013). Hainfeld et al., 2004 have provided the first *in vivo* experiment with gold NPs and 250 kVp X-rays to control a malignant tumor in mice, reaching 86% one-year survival versus 20% with X-rays alone and 0% with gold alone. This pioneering work has stimulated the exponential (sharp) growth of studies in the field of NP radiosensitization. A summary of *in vitro* and *in vivo* studies on gold NP radiosensitization can be found in a review by Her et al., 2017. Kuncic and Lacombe, 2018 have presented a topical review describing *in vivo* studies, and their key findings carried out with Au, Gd, Hf, and iron oxide-based NPs. Clinical trials with NP radiosensitizers are currently limited by two NPs: NBTXR3, a hafnium-based intratumorally administered NP, and AGuIX, a gadolinium-based intravenously administered NP (Wang et al., 2019).

Irradiation of any biological system generates a succession of processes, which can be divided into three phases: physical, chemical, and biological (Her et al., 2017; Joiner and Van der Kogel, 2018, p.3). The physical phase is the period in which biological molecules are ionized or excited by radiation to generate free radicals. In the chemical phase, these highly reactive free radicals react with other molecules to ‘‘restore electronic charge equilibrium’’. The biological phase refers to the stage in which the effects of radiation on cells lead to events such as irreparable DNA damage, permanent cell cycle arrest, and finally, cell death (Cui et al., 2014).

There are a great number of Monte Carlo (MC) studies devoted to the simulation of the physical phase of the interaction of photons (X-rays and MV beams) with gold NPs embedded in water (see, for instance, Chow, 2018, and references therein) while the MC simulation for other high-*Z* radiosensitizers is limited (McMahon et al., 2016, Alejo-Martinez et al., 2019). The enhancement of physical dose due to NPs was also studied by employing approximate analytical formulations. Ngwa et al., 2010 have carried out analytic calculations based on the electron energy loss formula of Cole, 1969 to estimate the endothelial dose enhancement caused by radiation-induced photo/Auger electrons originating from gold NPs targeting the tumor endothelium. The endothelial dose enhancement factor representing the dose ratio to the endothelium with and without NP was calculated for ^{103}Pd, ^{125}I, and ^{169}Yb as well, as 50 kVp X-rays sources, different NP local concentrations, and endothelial cell thicknesses. (Berbeco et al., 2011) and (Detappe et al., 2013) have provided similar analytic calculations to estimate the localized dose enhancement to tumor blood vessel endothelial cells via megavoltage X-rays and targeted GNPs. The results of (Berbeco et al., 2011) for both Monte Carlo and analytical approaches were compared and found to be remarkably similar. (Hossain and Su, 2012) Used an analytical approach developed by (Ngwa et al., 2010) to derive the radiosensitizing abilities of Bi, Au, and Pt NPs under 50, 110, and 300 kVp X-rays.

The main factor for the dose increases in NP-assisted radiotherapy is the generation of secondary electrons in a high-Z NP under photon irradiation and their emission from the NP with sufficiently high energy, which is thereafter efficiently deposited in the surrounding medium. Therefore, the quantitative determination of the energy and angular distribution of emitted electrons from NPs of different materials and sizes is the most important step in predicting the dose enhancement in the NP vicinity. All articles available the in literature and devoted to MC simulations of the dose enhancement due to NPs include the evaluation of secondary electron

spectra as an intermediate step of the simulation. However, only a few of them have presented the energy spectra of electrons emitted from the NP surface (McMahon and Currell, 2013; McQuaid et al., 2016; Chow, 2016; Jung et al., 2018; Li et al., 2020). Moreover, the published energy spectra were integrated over emission angles, limiting their application to estimate the dose enhancement around NPs.

In contrast to a significant number of MC studies devoted to describing RDD around irradiated NPs, analytical consideration of this problem is practically absent. The main advantage of analytical modeling compared to computer simulations is the possibility to derive implicit or explicit equations, which are much simpler than the table results of computer simulations and more convenient for the quantitative description of any given application. Moreover, analytical equations are useful for finding the most important parameters that influence a considered system and allow one to optimize experimental conditions in order to achieve a maximum effect. Of course, MC studies of complex problems provide more precise numerical results than an analytical consideration, which unavoidably simplifies a physical model under study due to the inability to take into account all needed physical effects. However, if an analytical review correctly describes the main features of the problem being studied, it will provide valuable information about the nature of the problem and will make it possible to change the parameters and conditions without having to re-run expensive and time-consuming MC simulations.

1.2 Hypothesis and objectives

The thesis aims to contribute to the theoretical study of radiation therapy assisted with high-Z NPs and propose a framework for estimating the survival of NP-loaded tumor cell cultures irradiated with monoenergetic and therapeutic photon beams. The framework is based on the local effect model (LEM) that was initially applied to predict the survival probability for individual cells irradiated by heavy charged particles using the cells' response to photon radiation (Pfuhl et al., 2020). The fundamental assumption of the LEM is that the local biological effect is determined by the local dose but is independent of the particular radiation type leading to a given local dose (Scholz, 2006). The absence of the principal difference between the biological effect of radiation with low and high linear energy transfer (LET), since, from a biological point of view, it does not matter whether secondary electrons are produced by primary low LET photons or by high LET charged particles. Therefore, the biological effect is simply determined by the total amount of

energy released in a specific sub-region of a cell of a suitable size. Because the secondary electrons ejected from irradiated high-Z NPs are similar to those produced by protons, the LEM was also applied for assessment of the radiosensitizing effects on cells with the NPs (McMahon et al., 2011a; McMahon et al., 2011b; Lechtman et al., 2013; Zygmanski et al., 2013a; Lin et al., 2015; McMahon et al., 2016; Brown and Currell, 2017; Sung et al., 2017; Ferrero et al., 2017; Melo et al., 2018). The hypothesis that is stated in the thesis is the following: the proposed framework, which combines MC simulation of the RDD around a single high-Z NP and analytical evaluation of the average dose and the average number of lethal lesions in a cell target by a set of ionized NPs, provides a prediction of the NPs radiosensitization effects

The **general objective** of the thesis is the development and validation of the theoretical framework for modeling the radiosensitization effect in photon-irradiated cells with embedded high-Z NPs. The **specific objectives** are the following:

1. To consider the radiation transport from a radiation source to a tumor region and to develop a general approach accounting for the sharply inhomogeneous dose distribution within a single cell and its surroundings due to the presence of irradiated NPs.
    1.1. To derive analytical expressions for calculation of the probability of ionization in a single NP irradiated by mono- and poly-energetic photon beams.
    1.2. To describe the dose distribution in a cell loaded with NPs.
    1.3. To derive integral expressions describing the average number of lethal lesions in an irradiated cell loaded with NPs and the cell survival probability.
2. To develop a Monte Carlo approach for the simulation of the passage of ionizing radiation through matter using the TOPAS tool.
    2.1. To study the interaction of incident photon fluence with a NP and determine the energy and angular spectra of escaped photo and Auger electrons on the NP surface.
    2.2. To evaluate by MC simulation the probability of ionization in a single NP irradiated by mono- and poly-energetic photon beams per irradiation dose.
    2.3. To evaluate the radial dose distributions around high-Z NPs irradiated with mono- and polyenergetic photon beams and to fit them by a power law function.
3. To consider the dose deposition in a spherical cell target and to develop an analytical approach for evaluating the NPs radiosensitization effects.

3.1. To derive the explicit analytical expressions describing the average doses and the average of the squared doses per one ionized NP located at a given distance from the target center.

3.2. To derive analytical expressions describing the energy deposition in a spherical cell nucleus by ionized NPs randomly distributed in the nucleus, cytoplasm, and extracellular media.

3.3. To derive analytical expressions for metrics quantifying the biological effects of the radiation treatment assisted with NPs describing the cell survival, the relative biological efficiency, the sensitizer enhancement ratio, the mean inactivation dose, and the relative biological enhancement.

4. To perform specific calculations for a spherical MDA-MB-231 cell with embedded gold GNPs irradiated with mono- and polyenergetic photon beams and validate the proposed combined framework.

4.1. To derive analytical expressions describing the energy deposition in a spherical cell nucleus by ionized NPs randomly distributed in the nucleus, cytoplasm, and extracellular media.

4.2. To perform the systematic MC study of RBE for X-ray irradiated MDA-MB-231 cells loaded with high Z NPs and irradiated with mono- and polyenergetic photon beams and to compare the calculated RBE with literature data.

1.3 Thesis Outline

This thesis consists of seven chapters. The introductory **Chapter 1** presents background information in the form of a brief review of the existing literature related to radiation therapy assisted with high-Z NPs and provides motivation for the development of a framework for the estimation of the survival of NP-loaded cell cultures irradiated with photon beams and describes the hypothesis stated in the thesis as well as the general and specific objectives that were undertaken in order to develop the framework.

Chapter 2 presents the comprehensive literature survey devoted to the theoretical consideration of the radiosensitization effect of high-Z NPs on cells exposed to keV and MeV photons. The subchapters describe the physical, chemical, and biological phases of the impact of ionizing radiation on a biological system, the calculation of dose enhancement by NPs at macro- and nanoscales, and radiobiological models, which relate the nanoscale energy deposition from photon-irradiated NPs to biological outcomes.

An analytical approach for quantification of the radiosensitization effect (general scheme) is developed in **Chapter 3**. The first and second subchapters present equations for quantifying NP concentration in a cell and calculating the probability of ionization of a single NP per irradiation dose. In the next four subchapters (third to sixth), the LEM extension of the LQ model for NPs loaded cells is used for the derivation of equations describing dose distribution, the average number of lethal lesions, and the survival probability in a cell loaded with NPs.

The energy deposition in a spherical cell target from an irradiated NP of a given radius is considered in **Chapter 4**. Using the additional assumption that the dose distribution around the NP is spherically symmetric and is described by a power law function, the general equations containing triple integrals are taken, and explicit expressions for the average dose and the average of the squared dose in the cell target are obtained.

Chapter 5 describes MC simulations of RDD around an irradiated gold NP. The subchapters present MC simulations of the probability of ionization of a single GNP per Gy, RDD around a 20 nm GNP irradiated with 100 keV photons, and RDD around ionized GNPs of various radii irradiated with keV and MeV photon beams.

In **Chapter 6**, the explicit expressions derived in Chapter 4 and RDDs simulated in Chapter 5 are applied to predict radiosensitization effects in spherical cells with embedded GNPs irradiated with X-rays. The first and second subchapters present calculated average doses deposited in the

cell nucleus and the average number of additional lesions per one ionized GNP of 20 nm diameter irradiated with 100 keV photons. The third subchapter estimates the NP-related LQ model parameters and corresponding cell survival curves for irradiated with 100 keV photons cells containing 1, 3, and 10 mg g^{-1} randomly distributed 20 nm GNPs. The fourth subchapter provides the validation of the proposed framework by comparing predicted RBE values for irradiated MDA-MB-231 cells in the presence of 0.5 mg g^{-1} of GNPs calculated in this work and MC simulated by (McMahon et al., 2011a).

The final **Chapter 7** summarizes the work presented in this thesis and discusses possible promising topics for continued research into high-Z NP radiosensitization. Furthermore, an appendix (**Appendix 1)** shows a brief introduction to TOPAS and examples of the simulation files that were used to obtain the results of chapter 5.

CHAPTER 2

High-Z nanoparticles enhanced radiotherapy (Literature Survey)

Radiotherapy with external and internal ionizing radiation sources is extensively employed for the treatment of almost all types of solid tumors (Mesbahi, 2010). Given that radiation therapy does not discriminate between cancerous cells and normal cells, the main challenge during the treatments is to increase its therapeutic efficacy without increasing damage to the surrounding healthy tissue (Retif et al., 2015). Advances in radiotherapy focus on improving the positioning and precision of radiation fields to the tumor target and reducing the consequential toxicities caused by irradiation of surrounding organs. The implementation of advanced radiotherapy modalities such as intensity-modulated radiation therapy, image-guided radiotherapy, stereotactic ablative body radiotherapy, proton therapy, electron beam therapy, and so on, all aimed at achieving greater therapeutic efficacy, fewer side effects, and less time under treatment (Butterworth et al., 2012; Ngwa et al., 2017). Nonetheless, these advanced radiotherapy modalities alone are insufficient to treat cancers because they fail to kill developed metastases outside the targeted volume (Misawa and Takahashi, 2011).

A promising way to increase the differential effect between cancerous and normal tissues is the incorporation of high-Z NPs into the tumor tissue or even into the tumor cells. There are dozens of excellent reviews (see most recent and references therein: Bromma and Chithrani, 2020; Choi et al., 2020; Schuemann et al., 2020; Vlastou et al., 2020; Abdollahi et al., 2021; Gong et al., 2021; Kempson, 2021; Moradi et al., 2021; Thanekar et al., 2021; Zheng et al., 2021) and several books (Mirkin et al.; Guo, 2018; Sajo and Zygmanski, 2020), in which the experimental and theoretical studies devoted to high-Z NPs radiosensitizers are summarized. Below, the literature survey limited by only theoretical consideration of the radiosensitization effect of high-Z NPs on cells exposed to keV and MeV photons is presented.

2.1. Theoretical consideration of the radiosensitization effect: general discussion

The effect of ionizing radiation on a biological system can be considered as a succession of processes that differ enormously in timescale (Fig. 2.1) and is usually split into physical, chemical, and biological phases (Joiner and van der Kogel, 2018, p. 3).

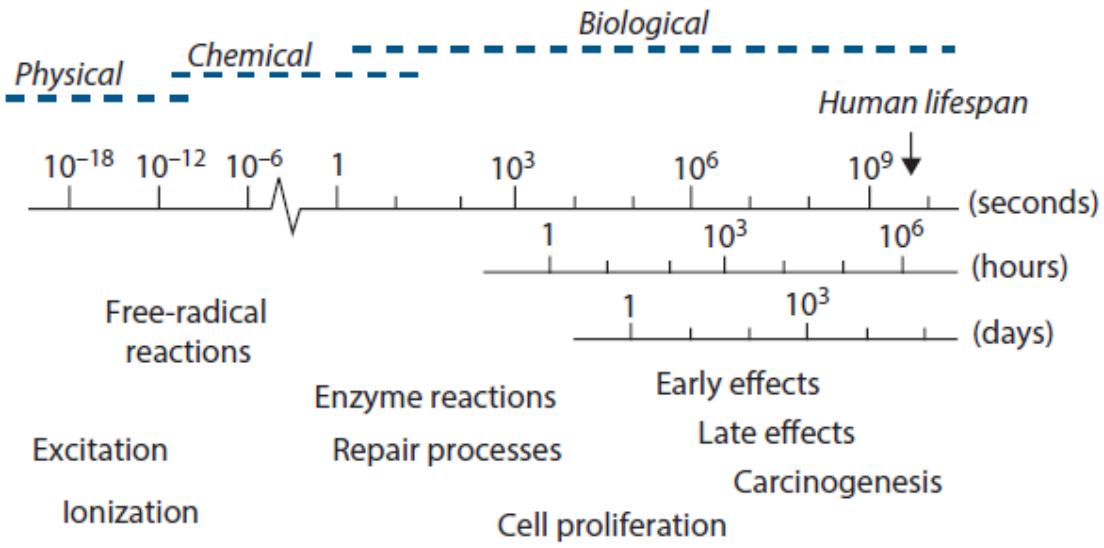

Figure 2.1. The timescale of the effects of radiation exposure on biological systems. Borrowed from Joiner and van der Kogel, 2018, p. 3.

The physical phase is the period in which high-energy particles (keV - MeV photons, electrons, protons, or heavy ions) travel through biological targets and cause ionization and/or excitation of the molecules, creating the breakage of chemical bonds and generation of free radicals. The chemical phase describes the period in which these ionized or excited atoms and molecules react with other cellular components in rapid chemical reactions. Ionization and excitation lead to the breakage of chemical bonds and the formation of broken molecules, known as 'free radicals'. These are highly reactive and engage in a succession of reactions that eventually lead to the restoration of electronic charge equilibrium. Free-radical reactions are completed within approximately 1 ms after radiation exposure. The biological phase follows the physical and chemical ones and consists of the responses of the biological targets to irradiation treatments at the molecular, cellular, and tissue levels.

2.1.1. Physical phase

The vast majority of the articles devoted to the theoretical consideration of the radiosensitization effect are limited to the physical stage and are focused on the quantitative description of the dose enhancement due to the presence of NPs in cells and cell structures. The NP dose enhancement is a multiscale computational problem, spanning seven orders of magnitude in the spatial distance, from nanometers to centimeters, and six orders of magnitude in energy,

from eV to MeV (Sajo et al., 2020). To overcome this problem, simulations of energy deposition are carried out separately at macroscopic (mm – cm) and submicroscopic (or nanoscopic) levels (Zygmanski et al., 2013b; Zygmanski and Sajo, 2016). In the macroscopic stage of the simulation, the keV or MeV photons are transported across macroscopic depths (mm to cm) in a homogeneous medium to a location near tumorous cells loaded with NPs where the phase space is determined. Phase space incorporates all particle types, their numbers, energy, and direction of motion. The phase space is scored after some phantom penetration, commonly the phantom is simulated as a geometrical water volume (Lin et al., 2014), or in some cases, a specific material with closer properties to real tissue is selected, like the ICRU four component soft tissue (Lechtman et al., 2011). In the nanoscopic stage, this phase space (or sometimes photon-electron spectrum) is used as the input radiation source for new simulations that allow one to describe the phase space's interaction with NPs and calculate the dose distribution around a single NP or their clusters. Thereafter, various dose enhancement metrics are calculated based on the dose deposition in cells and/or cell structures. Typically, in the context of high-Z NPs, macroscopic simulations of coupled photon–electron transport for clinical beams are performed using a wide variety of MC codes. The detailed review of transport capabilities for photons and charged particles (electrons, positrons) of MC simulation codes used for radiotherapy beam modeling is presented by Verhaegen and Seuntjens, 2003. Sub-micron (nanoscopic) simulations are carried out using MC simulation codes based on the condensed history or track structure, such as Penelope, GEANT4, TOPAS, MCNP6, MDM, PARTRAC, and NASIC (Li et al., 2020), whose energy cutoff permits the simulation of shorter electron ranges. The physical stage will be considered in more detail in subsections 2.2 and 2.3, devoted to the macro calculations of dose enhancement factor by NPs and nanoscale dose deposition in cells and cell structures, respectively.

2.1.2. Chemical phase

The radiosensitization effect at the chemical stage is considered in detail in the monograph by Guo, 2018. He defined chemical enhancement as the enhancement of the effectiveness of X-ray irradiation by catalytic nanomaterials dissolved or embedded in media. Because the principal constituent of the biological tissue is water, the primary pathways of radiation-induced cell killing are through the generation of free radicals and reactive oxygen species (ROS) such as superoxide

radicals (O_2^-), hydrogen peroxide (H_2O_2), and hydroxyl radicals ($^{\cdot}OH$) (Chatterjee and Magee, 1989). The ROS interact with various cellular components and cause cellular damage directly by interacting with biological molecules or indirectly by exerting oxidative stress and triggering cell death via apoptosis or necrosis (Her et al., 2017). As Her et al. (2017) pointed out, the chemical stage has not yet been fully investigated. While there have been many theoretical studies on the physical step, only a few MC simulations have been conducted on the chemical enhancement for GNP-enhanced radiation therapy (Xie et al., 2015; Tran et al., 2016; Rudek et al.,2019; Poignant et al., 2020).

2.1.3. Biological phase

The theoretical study of the radiosensitization effect of high-Z NPs at the biological stage is mainly performed in two directions. The first one is devoted to the consideration of DNA damage. Nuclear DNA is the most critical cellular target of ionizing radiation for causing mutations and cell death. DNA damage from ionizing radiation occurs via direct and indirect mechanisms to destroy cells and biological tissue. In direct action, radiation directly induces single-strand breaks (SSB) and double-strand breaks (DSB) in DNA, resulting in the termination of cell division and proliferation or even cell necrosis and apoptosis. The indirect effect refers to the interaction of radiation with bulk water, producing radical species that, in turn, react with DNA. The MC simulation of ionizing radiation tracks is the typical method for modeling DNA damage (Lampe et al., 2018; Sakata et al., 2020). The direct and indirect effects are proportional to the dose delivered in irradiated cells; therefore, the presence of high–Z NPs near or inside cells will enhance the DNA damage. He and Chow, 2017 and Jabeen and Chow, 2021 estimated the DNA damage due to the GNP dose enhancement using a Geant4-DNA MC simulation. By constructing a single GNP at different distances to the DNA molecule, they found a strong dependency of the dose enhancement on the GNP size and photon beam energy.

The second theoretical direction is the multiscale modeling of the biological effects of the radiation treatment assisted with high-Z NPs. This approach combines the chemical and biological phases and directly relates the dose deposited in cells and cell structures to their damage. McMahon et al., 2011a, presented the first calculations, which take into account the structure of energy deposition in the nanoscale vicinity of GNPs and relate this to biological outcomes using the LEM

extension of the LQ model, reporting a good agreement with experimentally observed cell killing by the combination of X-rays and GNPs. The further development of this methodology will be considered in subsections 2.4.

2.2. Macro calculations of dose enhancement ratio by NPs

In radiation oncology, dose enhancement due to the presence of high-Z NPs is quantified by the dose enhancement ratio or dose enhancement factor (DEF), defined by Cho, 2005 as the ratio of the dose with and without NPs in the tumor region. Numerous theoretical studies have investigated dose enhancement caused by the presence of high-Z NPs. This subsection discusses the macro calculations of DEF presented in the literature.

2.2.1. Interaction of ionizing photon radiation with gold NPs

Photons with energy in the ionizing radiation category have several options for interacting with matter. Podgorsak, 2014 (subchapter 8.5) indicates seven important interactions in medical physics and radiation dosimetry: Thomson scattering, Rayleigh (coherent) scattering, Compton (incoherent) scattering, photoelectric effect, nuclear pair production, triplet production, and photodisintegration. Among them, only three, the photoelectric effect, Compton scattering by "free" electron, and nuclear pair production, are of major importance due to their high probability of taking place. Only two of them (see figure 2.2) should be taken into account when considering X-ray dose enhancement: photoelectric effect and Compton scattering. After each successful interaction of one X-ray photon with a NP, a secondary photoelectron or Compton scattered electron is knocked out from an atom. Additionally, Auger and Coster–Kronig electrons (also usually designated as "Auger electrons"), as well as characteristic (fluorescence) photons, appear due to the atomic deexcitation cascades. The number of characteristic photons emitted per orbital electron shell vacancy is referred to as fluorescence yield ω. In contrast, the number of Auger electrons emitted per orbital electron vacancy equals (1 - ω). The characteristic photons absorbed sufficiently far from a NP do not significantly contribute to the dose around the NP and will not be considered here. On the other hand, low-energy Auger electrons are absorbed in and near the

NP and provide substantial and often major contributions to the dose deposition near the NP surface.

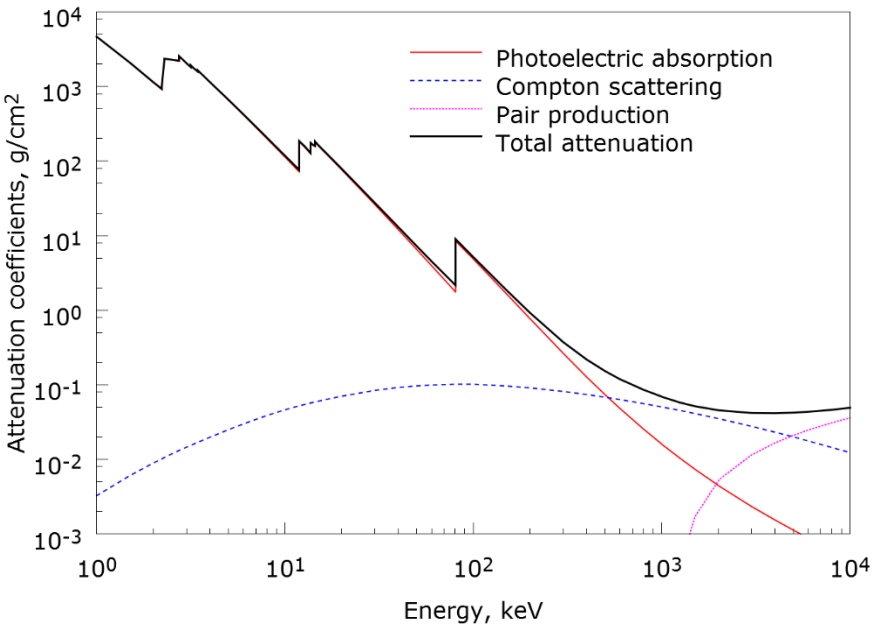

Figure 2.2: Mass attenuation coefficient of gold with contributing sources of attenuation: photoelectric absorption, Compton (incoherent) scattering, and pair production. The discontinuities of photoelectric absorption values are due to K-, L-, and M-edges. Data extracted from NIST's XCOM database: https://physics.nist.gov/PhysRefData/Xcom/Text/intro.html.

In the energy range of therapeutic interest, water is nearly a pure Compton scatterer, while gold and other high-Z materials are almost pure photoelectric absorbers. For Z = 64 – 79 (e.g., Gd, Tb, Dy, Ho, Hf, Ta) photoelectric effect dominates the X-ray interactions below about 400 keV. In the range of Z = 74 – 82, which includes Re, Os, Ir, Pt, Au, Tl, and Pb, photoabsorption is dominant below 500 keV. These materials are mainly Compton scatterers at higher energies, but their photoelectric cross-section remains relatively high. For example, at about 1 MeV photon energy, the ratio of Compton versus photoelectric cross-sections is between a factor of 5 and 10 in these materials, while in the water, this ratio is more than 10^4. Therefore, secondary electron production via the photoelectric mechanism in high-Z materials remains significant even at megavoltage energies.

2.2.2. Analytical calculations of macroscopic dose enhancement factor

Zygmanski and Sajo, 2016 define DEF for macroscopic regions or mass-equivalent mixtures of the NP substance with water for a specific concentration of NP in water as:

$$DEF_{macro}\left(\vec{x}\right)=\int_{V\left(\vec{x}\right)}D_{GNP}\left(\vec{x}_1\right)d^3x_1\Big/\int_{V\left(\vec{x}\right)}D_w\left(\vec{x}_1\right)d^3x_1\,, \tag{2.2.1}$$

where the dose $D\left(\vec{x}\right)$ is assumed to be computed with sufficient spatial resolution, and the integration (scoring) volume $V\left(\vec{x}\right)$ is centered at $\vec{x}$, which is measured in hundreds of micrometers to millimeters rather than nanometers. In (2.2.1) D_{GNP} is the dose deposited in the water medium when the GNPs are presented and D_w is the dose deposited in the same volume of water without GNPs for the same irradiation conditions. It is assumed that the volume size is much larger than the range of Auger electrons (the range of Auger electrons due to a gold K-shell vacancy in liquid water spans from a fraction of nm to about 100 mm).

Under charged-particle equilibrium and monoenergetic photon beam, the DEF_{macro} is simplified to (Corde et al., 2004):

$$DEF_{macro}=\frac{\left(\frac{\mu_{en}}{\rho}\right)_E^{water+NP}}{\left(\frac{\mu_{en}}{\rho}\right)_E^{water}}=\frac{w_{NP}\left(\frac{\mu_{en}}{\rho}\right)_E^{NP}+\left(1-w_{NP}\right)\left(\frac{\mu_{en}}{\rho}\right)_E^{water}}{\left(\frac{\mu_{en}}{\rho}\right)_E^{water}}\,, \tag{2.2.2}$$

where w_{NP} is the fraction by weight of the NP substance in the NP-water mixture, and $(\mu_{en}/\rho)_E$ is the mass energy-absorption coefficient at the photon energy E.

The formula describing DEF_{macro} for a polyenergetic photon beam can be found in the article by Roeske et al., 2007):

$$DEF_{macro}=1+w_{NP}\int\Phi(E)E\left[\frac{\mu_{en}\left(E\right)}{\rho}\right]_{NP}dE\Big/\int\Phi(E)E\left[\frac{\mu_{en}\left(E\right)}{\rho}\right]_{w}dE\,, \tag{2.2.3}$$

where Φ(E) is the photon fluence.

As follows from (2.2.3), the DEF_{macro} for a mixture of water and a uniformly distributed NP substance is directly proportional to the weight fraction of the substance and ratio of the mass energy-transfer coefficients of water and the NP substance both averaged over the photon fluence.

Theoretical calculations of macroscopic DEF values for MeV for various GNPs concentrations as a function of photon energy are shown in Figure 2.3. The curves presented on the left and right parts of Figure 2.3 are borrowed from the articles by Shahhoseini et al., 2018 and Rahman et al., 2014, respectively. The macroscopic DEFs for a range of photon energies between 1 keV and 2 MeV were calculated for monoenergetic photon beams using Eq. 2.2.2. The mass-energy absorption coefficients were obtained from the National Institute of Standards and Technology (Berger et al., 1998 [https://www.nist.gov/pml/xcom-photon-cross-sections-database]. The DEFs strongly depend on the photon energy and the concentration of the GNPs. The highest DEF was observed at a photon energy of around 40 keV, which is less than gold K-edge energy (80.7 keV). At K-edge energy, DEF increases sharply; beyond the K-edge, it gradually decreases with increasing energy; and above 1 MeV, the DEF comes to unity.

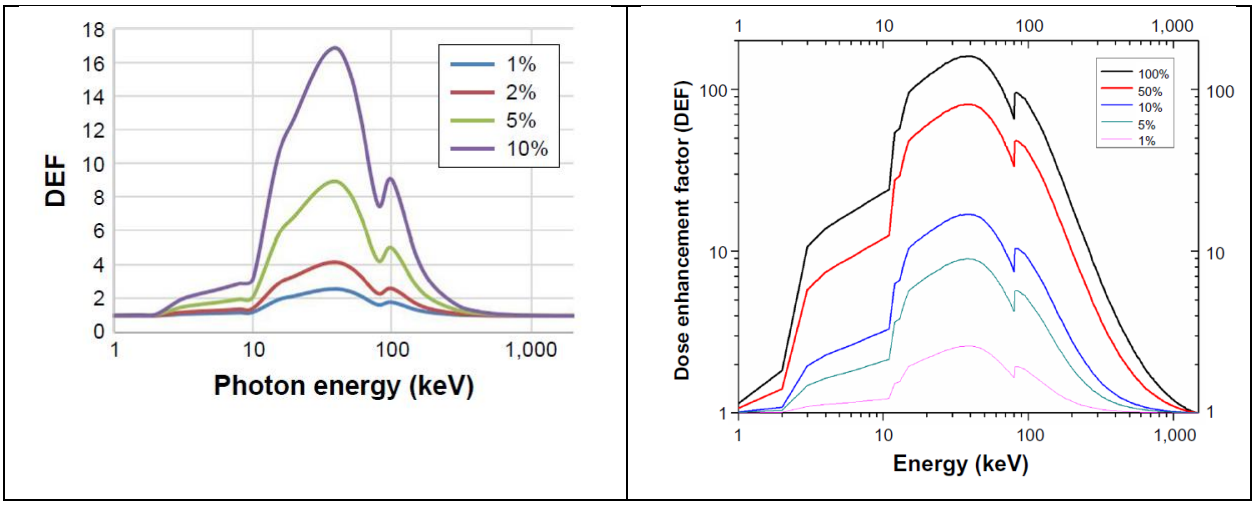

Figure 2.3. The dose enhancement factor was calculated for various concentrations of the gold mixture in water exposed to monoenergetic photon beams. Graphs borrowed from Shahhoseini et al., 2018 (left) and Rahman et al., 2014 (right).

The computationally determined values of the macroscopic DEF are not so high and often exhibit noticeable differences when compared with the corresponding experimental relative biological effectiveness. In particular, in vitro experimental studies of GNP radiosensitization present a rather different picture, with many reporting radiation-sensitizing effects substantially greater than the additional dose due to the presence of GNPs (Rahman et al., 2009; Jain et al., 2011; Butterworth et al., 2010). These discrepancies may have various causes. One of the most obvious is the highly inhomogeneous energy deposition around GNPs. This leads to the much

higher DEF in the vicinity of individual GNPs in comparison with the macroscopic DEF and, as result, to the increased radiation damage of cell structures near GNPs.

2.2.3. Monte Carlo simulation of macroscopic dose enhancement ratio

Subiel et al., 2016 have provided a comprehensive overview of MC calculations of the DEF from GNPs at the macroscopic level (mm to cm scales) in response to clinical X-ray beams. They have considered thirteen articles published between the years 2007 and 2013 and summarized in the corresponding columns of Table 5 the MC simulation codes (Geant4, Geant4-DNA, EGSnrc, MCNP5, MCNPX, NORTEC, PENELOPE), the simulation type of the electron transport approximation (condensed history method or step-by-step simulation) and the radiation source (the external monoenergetic photon beams (20 keV – 1.25 MeV), kVp and MV spectral X-ray sources, internal brachytherapy γ-ray sources (^{103}Pd, ^{125}I, ^{169}Yb, ^{192}Ir)). The dose enhancement effects were characterized by considering numerous physical interactions and quantities, such as photoelectric absorption, properties of secondary electrons ejected from nanoparticles, photoelectric energy conversion, and physical dose ratios between irradiation with and without NPs. The DEF values were determined for various simplified geometries approximating clinical conditions without accounting for the energy deposition at sub-micrometer scales.

There are two possible ways to simulate the presence of high-Z materials in the irradiated media. The first one is to consider a uniform mixture of gold-water with a given percentage weight of gold in tissue. The second way is to model a medium with a given number of NPs placed at specific locations in irradiated tissue. To compare these two approaches, Zhang et al. 20 studied the absorbed dose for the gold-water mixture and that of the uniform distribution of $\sim 10^{13}$ gold nanospheres of 100 nm diameter in a water phantom irradiated with ^{192}Ir brachytherapy source. They observed an overestimation of dose enhancement up to 16 % caused by modeling gold-water mixture rather than gold nanospheres geometry. Martinov and Thomson, 2017 obtained similar results. They introduced a heterogeneous multiscale model for Monte Carlo simulations of GNPs, including a phantom (cylindrical for a parallel beam of monoenergetic photons and spherical for a brachytherapy source) containing a homogeneous mixture of gold tissue with embedded GNPs. It was shown that for all concentrations and diameters of GNPs, DEFs calculated for the gold-tissue

mixture model overestimated those for their heterogeneous multiscale model by about 20% for a 20 keV beam, varying with the depth of penetration and photon energy.

On the whole, summarizing the macro calculations of the dose enhancement factor of high-Z NPs, it is possible to conclude that the assumption of homogeneous atomic gold distribution versus individual GNP clusters can significantly under- or overestimate the computed DEF in tumor subvolumes and near vascular deposits of GNPs (Sajo et al., 2020).

There are several similar works where the macroscopic enhancement of physical dose due to GNPs was studied by employing approximate analytical formulations (Ngwa et al., 2010, Berbeco et al., 2011, Hossain and Su, 2012, Detappe et al., 2013). Ngwa et al., 2010 have conducted analytic calculations based on Cole's electron energy loss formula (Cole, 1969) to estimate the endothelial dose enhancement caused by radiation-induced photo/Auger electrons originating from GNPs targeting the tumor endothelium. A tumor vascular endothelial cell was modeled as a slab of 2 μm (thickness) × 10 μm (length) × 10 μm (width) (see Figure 2.4a). A NP size of 400 nm diameter was chosen to keep GNPs small relative to the endothelial cells but large enough to be restricted within the vasculature (Maeda et al.2005). The average concentration in the vasculature was chosen to be 140 mg/g (assuming that the vasculature constitutes 5 % of the tumor volume Ryschich et al., 2004, the GNPs are restricted to the vasculature and the total tumor concentration of 7 mg/g). Considering a micro-segment of the tumor vasculature with a diameter of 20 μm and a thickness of about one endothelial cell length (10 μm) (see Figure 2.4b), the mass of the vasculature micro-segment is about 15.7 times the mass of one endothelial cell.

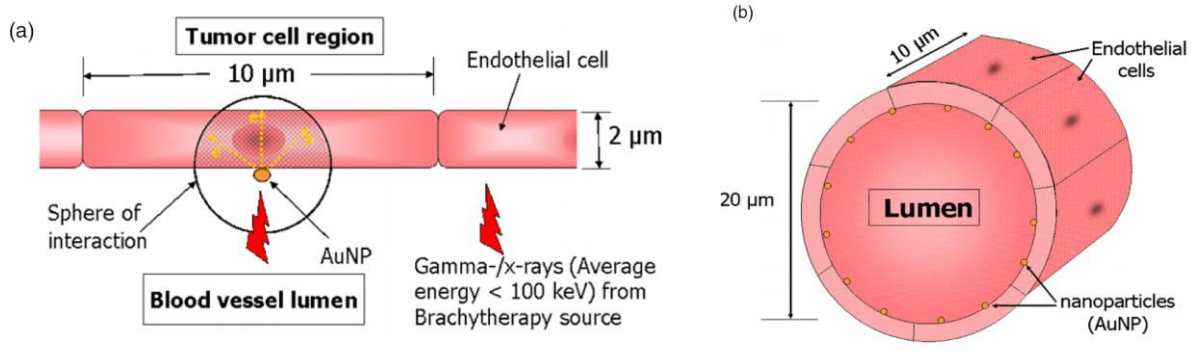

Figure 2.4. (a) Simplified slab model of the endothelial cell layer between the lumen and the tumor cells. The gold nanoparticles are attached to the lumen side of the endothelial cells. The range of photoelectrons is shown as a 'sphere of interaction' with the nanoparticle at the center. Only the dose deposited within the adjacent endothelial cell (shaded region) is used to calculate the dose enhancement. (b) Transverse view of an idealized micro-vascular segment with gold nanoparticles distributed along the interior endothelial cell wall. Images borrowed from Ngwa et al., 2010.

The endothelial dose enhancement factor representing the ratio of the dose to the endothelium with and without NP was calculated for ^{103}Pd, ^{125}I, and ^{169}Yb as well as 50 kVp X-rays sources, different NP local concentrations, and endothelial cell thicknesses. The results reveal that the ablative dose enhancement to tumor endothelial cells due to photo/Auger electrons from the GNPs can be achieved. The results also reveal that the highest contribution to the DEF comes from Auger electrons, apparently due to their shorter range.

Berbeco et al., 2011, have provided analytic calculations to estimate the localized dose enhancement to tumor blood vessel endothelial cells via megavoltage X-rays and targeted GNPs. Endothelial cells were modeled as thin slabs with 100-nm-diameter GNPs attached within the blood vessel. The number of photoelectrons emitted per GNP per gray of X-rays was computed using a MC–generated energy fluence spectrum. The energy deposited by photoelectrons escaping GNPs to the endothelium was calculated based on the same analytic method and formulas as proposed in (Ngwa et al., 2010). The additional dose that may be deposited in the endothelium via Auger electrons was not considered in this analytic calculation. It was shown that the DEF reach a value of 1.7 for an intravascular GNP concentration of 30 mg/g. Most of this dose enhancement arises from the low energy (below 100 keV) portion of the linear accelerator X-ray spectrum. Furthermore, for GNP concentrations ranging from 7 to 140 mg/g, DEF values of 1.2 to 4.4 are calculated.

Detappe et al., 2013 have provided similar analytic calculations to estimate the localized dose enhancement to tumor blood vessel endothelial cells via megavoltage X-rays and targeted GNPs. In the work by Berbeco et al., 2011, the results of both the Monte Carlo and the analytical approach were compared and found remarkably similar. Hossain and Su., 2012 used the analytical approach developed by Ngwa et al., 2010 to derive the radiosensitizing abilities of Bi, Au, and Pt NPs under 50, 110, and 300 kVp X-rays.

2.3. Nanoscale dose deposition around irradiated NPs

The macroscopic DEF calculations considered in the previous subsection could be applied to the estimation of the dose enhancement averaging the high-Z NP effect over volumes of about or more $(R_e)^3$, where R_e is the maximal range of secondary photoelectrons. Their mean ranges for

photon beams of 50 kVp and 250 kVp were found to be 2.7 and 26 μm, respectively (Lechtman et al., 2011) which is close to the typical size of a cell (about 10 μm diameter). As result, the macroscopic DEF presents the dose enhancement averaged over the cell that is not enough to predict biological damage at the subcellular level. Therefore, quantifying the nanoscopic energy deposition around an irradiated NP is an essential step to predict biological outcomes due to high-Z NP-assisted radiosensitization. In this subsection, we discuss the published articles, in which MC and analytical simulations were carried out to calculate the dose distribution in the nanoscale vicinity of GNPs.

2.3.1. Nature of the energy absorption by photon irradiated NPs

Kirkby and Koger, 2010 reviewed photon interactions with high-Z NPs and the subsequent dispersion of energy into the surrounding media. In subchapter 6.2, they highlighted how the energy is deposited within several hundred nm of NP and how it leads to some problems with dosimetry and modeling the biological effect in the presence of such NPs. Below, a summary of this subchapter is presented.

High-Z NPs present a larger interaction cross section to X-rays than soft tissue. Hence at keV energies, photons will interact in the high-Z material much more frequently than with tissue, releasing more ionizing electrons into the medium and thereby enhancing dose and subsequent radiation effects. It is important to bear in mind that NP dose enhancement is essentially a stochastic process on very small scales, and photon interactions within any given high-Z NP can be rare, simply because of their small size. For example, McMahon et al., 2011a reported that a 20 nm gold NP exposed to 100 keV X-rays would experience only 0.001 photon interactions per Gy deposited in the surrounding water volume. On the other hand, the number of NPs in or near a given cell can range from the hundreds to tens of thousands (Chithrani et al., 2009), thus exposing a given cell to a Poisson probability distribution of extra ionization events. Ionizations in the medium, the majority of which occur only within a few hundred nanometers of the NP, generate highly reactive radical species, which can then go on to interact with and potentially damage biologically sensitive structures such as DNA.

The physical quantity, absorbed dose, is a measure of the energy absorbed within a finite mass, making it a quantity well-defined only on relatively macroscopic scales (i.e., much larger

than typical cell dimensions) and for relatively high exposure levels. On small scales, the energy absorbed by the target volume (e.g., a cell nucleus, DNA macromolecule, mitochondrion, etc.) can vary drastically, making the absorbed energy a stochastic quantity (ICRU Report 86, 2011). Therefore, it becomes necessary to describe energy deposition in terms of well-parameterized probability distribution rather than a single quantity, bringing dose deposition into the realm of microdosimetry. On the other hand, despite the stochastic nature of photon interactions with an NP, once a photon does interact, the energy deposition patterns in the vicinity of the irradiated high-Z NP are predictable. When a photon interacts, it generates low-energy electrons. Though individual paths followed by electrons that escape high-Z NPs can be tortuous, their initial energy determines their ranges. A plot of the electron range in water as a function of the initial kinetic energy of the electron is presented in Figure 2.5, showing a comparison of results from the literature. It is clear from the figure that the initial kinetic energy of any electron escaping a high-Z NP dictates the spatial distribution of the energy they impart into the media surrounding the NP.

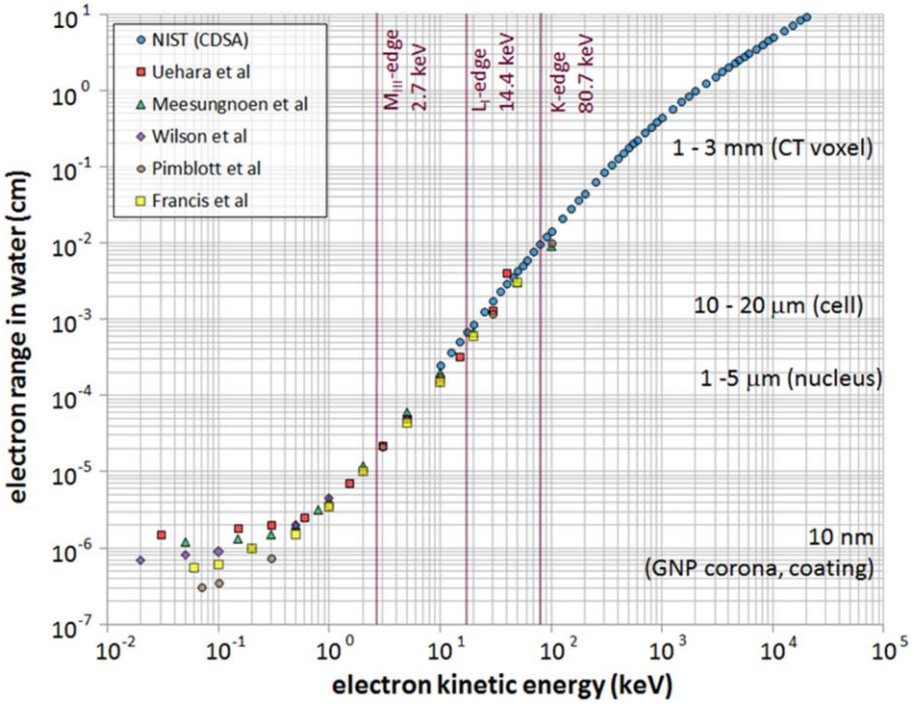

Figure 2.5. A plot of electron ranges in water as a function of kinetic energy is shown as taken from several sources. The NIST continuous slowing down approximation (CSDA) data (Berger et al., 2017) are shown down to 10 keV. Also shown are electron penetration ranges from Uehara et al., 1999, Meesungnoen et al., 2002, Wilson et al ., 2004, Pimblott et al., 2002, and Francis et al., 2011. The violet lines on the data show the approximate energies of K, L_I, and M_{III} edges, and pointed out the approximate dimensions of common objects of interest on the right for the context. Borrowed from Kirkby and Koger, 2010.

To illustrate the spatial distribution of the energy, the case of an isolated 25 nm radius spherical gold NP (GNP) in a water medium exposed to monoenergetic photons was investigated. Results from Monte Carlo simulations are shown in Figure 2.6. The dose per photon incident on the NP was scored in concentric spherical shells around the GNP. In a clinical scenario, the doses presented in Figure 2.6 would be superimposed on a background of dose that would result from radiation interacting in the surrounding medium. Interactions in the GNPs give rise to a spectrum of photo-electrons, Auger electrons, characteristic X-rays, and to a lesser extent, Compton electrons (Lechtman et al., 2011, Gadoue et al., 2017). In most cases, the secondary electrons will escape the GNP and go on to interact with the surrounding media.

The dose surrounding the GNP in Figure 2.6 falls off roughly as a power law relation with an exponent between -1.9 and -2.5, out to the maximum range of the emitted photoelectrons. A More subtle structure to each curve results from the emissions of much lower energy Auger electrons. When the photo-electron range is exceeded, the dose drops sharply over some orders of magnitude and then resumes with a tail due to emitted characteristic X-rays. A brief discussion of the available in literature RDDs around GNPs of various diameters and irradiated with different photon sources that were calculated using MC simulation is presented in the following subchapter.

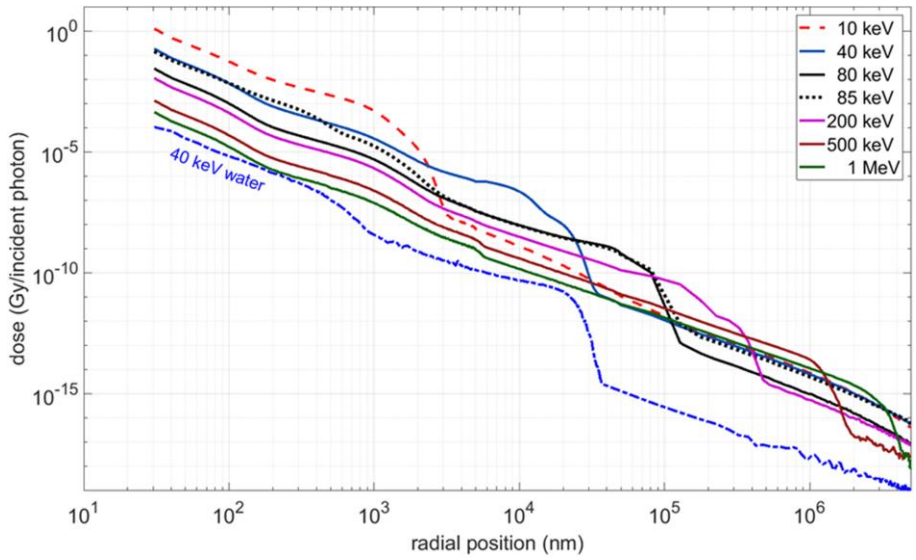

Figure 2.6. Monte Carlo predicted dose as a function of distance from a 25 nm radius GNP, normalized per photon incident on the GNP, shown for incident photons of selected energies. In the image, the dashed blue line is a similar curve for 40 keV photons incident on an equivalent volume of water (dashed blue). Image borrowed from Kirkby and Koger, 2010.

2.3.2. Monte Carlo simulation of RDD around GNPs

The lack of proper nanoscale experimental techniques to explore the dose-enhancing properties of gold nanoparticles (GNPs) interacting with radiation has led to the development of various MC-based nanodosimetry techniques that generally require considerable computational knowledge, time, and specific tools/platforms (Jayarathna et al., 2019). Nevertheless, there are some published articles devoted to MC simulation of the radial dose distribution (RDD) around GNPs within nano to microscale distances in response to X-ray beams (Carter et al., 2007; Jones et al., 2010; Leung et al., 2011; McMahon et al., 2011a; Lin et al., 2014; McMahon et al., 2016; Sung et al., 2017; Jung et al., 2018; Sung and Schuemann, 2018; Villagomez-Bernabe and Currell, 2019; Kirkby and Koger, 2010). These studies included monoenergetic photon beams as well as both external (Linac, X-ray tube) and internal (brachytherapy) X-ray sources.

The MC simulations of RDDs are usually obtained through three distinct steps. Firstly, a description of all the photons and electrons produced by a photon beam penetrating water phantom *is* recorded in the form of a phase space file. In the second step, the particles (predominantly photons and electrons) from this spectrum are allowed to interact with a single NP. Then, the outgoing phase space of all particles leaving the nanoparticle after any interaction is recorded. Finally, in the third step, these outgoing particles are transported through the water with the dose deposition as a function of the radius being recorded. This process gives rise to the RDDs, which are usually normalized on one incident photon or dose deposited in the water phantom. Below, several examples of simulated RDDs are presented.

Carter et al., 2017 were the first who calculate energy deposition in an aqueous solution with nanometer precision from low-energy electrons released from 3-nm GNP interacting with X-rays from a 100-kVp tungsten source. A large portion of the low-energy Auger and secondary electrons deposit their energy within a 5-nm-radius sphere after escaping the nanostructures, whereas photoelectrons from the GNP travel much farther.

Jones et al., 2010 had quantified dose point kernels (or RDDs) due to secondary electrons from GNPs on a nanometer scale around a 100 nm diameter GNP irradiated with ^{125}I, ^{103}Pd, ^{169}Yb, ^{192}Ir, 50 kVp, and 6 MV X-ray photon sources. The scaled dose point kernels in terms of dose per source photon per GNP are shown in the left panel of Figure 2.7. Once more, one can see the benefit of a lower energy source spectrum, as the increased contribution of photoelectric absorption in gold creates many more secondary electrons per incident photon. The right panel of

Figure 2.7 presents RDDs for 50 nm diameter GNP irradiated with mono-energetic kilovoltage X-ray sources (50, 100, 150, 200, and 250 keV) calculated by Lin et al., 2014. It is important to note that the RDDs in the right panel are presented as a function of the distance from the GNP surface, not from the GNP center. As a result, the calculated RRDs, which could be fitted by the power law, are not approximated by a straight line in the double logarithmic scale.

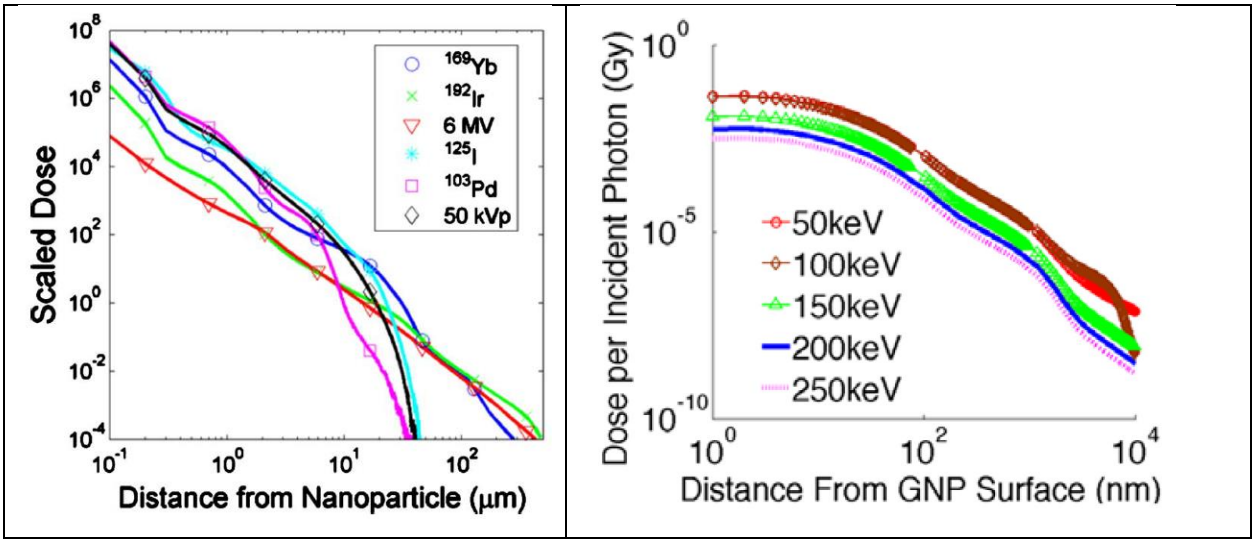

Figure 2.7. Left: scaled dose point kernels in a water medium for 100 nm diameter GNP irradiated with ^{125}I, ^{103}Pd, ^{169}Yb, ^{192}Ir, 50 kVp, and 6 MV X-ray photon sources. Image borrowed from Jones et al., 2010. Right: RDDs for 50 nm diameter GNP per incident photon of indicated energies. Image borrowed from Lin et al., 2014.

Leung et al., 2011 simulated the RDD around a 2, 50, and 100 nm in diameter GNP when irradiated with a 50 kVp, 250 kVp, cobalt-60, and 6 MV photon beam in water. The simulations have shown that most of the energy deposition was outside the GNP and Auger electrons are responsible for much of the additional deposited energy. McMahon et al., 2011a calculated the response of a single GNP suspended in water to monoenergetic X-ray radiation for a series of nanoparticle sizes (2 to 50 nm in diameter) and energies (20 to 150 keV) aiming to quantify the degree of dose inhomogeneity introduced by the presence of a GNP. *One remarkable* result was the very low rate of ionizing events in the GNPs - for example when a 20 nm GNP was exposed to 100 keV X-rays, approximately 0.001 ionisations were recorded per Gy deposited in the surrounding water volume. In addition, the substantial dose variation near the NP, with values on the order of thousands of Gy deposited in the vicinity of the NP following a single ionizing event,

was found. Such a combination of extremely high doses and extremely small volumes is relatively uncommon in X-ray radiotherapy, as the incident radiation is typically very sparsely ionizing.

McMahon et al., 2016 modeled radiation - NP interactions and resulting RDDs simulating individual 20 nm diameter NPs placed within the center of a 10 μm side length cube of water. NPs were modeled as pure spheres of individual elements ranging from Z = 14 to Z = 80. As ionization cross-sections and Auger spectrum depend strongly on photon energy for keV X-rays, individual X-ray energies were used for each material. Energies were set to 20 keV above the K-edge of the exposed material (ranging from 22 to 102 keV). This allows the comparisons between elements experiencing similar ionizing events, which primarily occur in inner shells, to allow the full impact of Auger electrons to be investigated. Figure 2.8 presents the nanoscale RDDs for an average ionizing event caused by either tuned keV X-rays (left) or a 6 MV Linac spectrum (right). The event is radiation - NP interaction which produces at least one secondary particle in NPs of a selection of elements.

Significant complexity is seen in keV irradiations, with differing energy distributions depending on the characteristic Auger cascade produced by the material. By contrast, MV irradiation produces similar energy distributions in all cases, as Auger electrons play a reduced role.

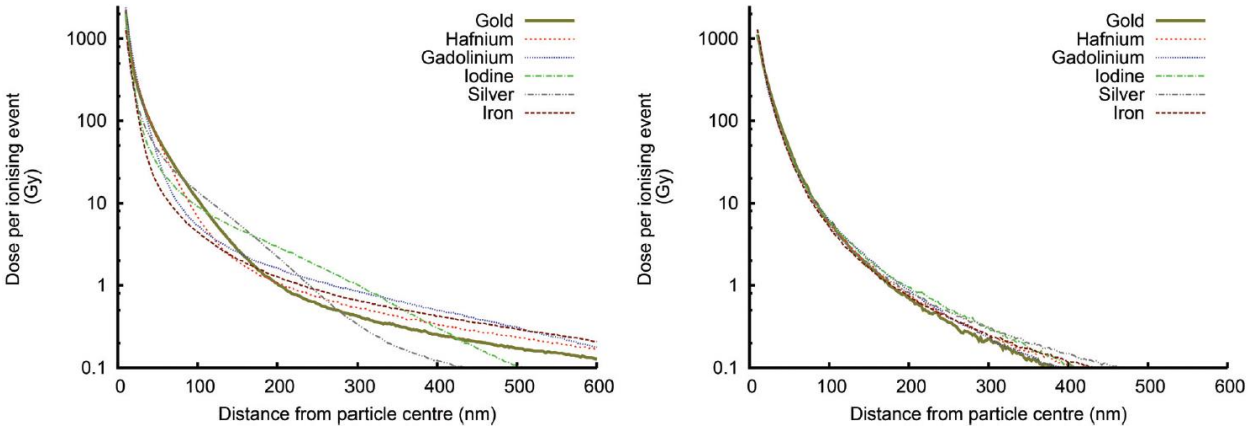

Figure 2.8. Nanoscale RDDs around 20 nm nanoparticles of various metals following a single ionizing event caused by either tuned keV X-rays (left) or a 6 MV Linac spectrum (right). Image borrowed from McMahon et al., 2016.

Sung et al., 2017 simulated RDDs around a single GNP (diameter = 2, 15, 20, 50 nm) irradiated with 150 kVp, 51 keV, and 6 MV photon beams. The RDD was calculated from the surface of GNP in spherical shells with a thickness of 1 nm up to 50 μm. Based on the obtained RDDs, analytic functions were derived to describe the radial dose originating from GNPs. The structure of the analytic functions was Dose = $a\times(\text{radius})^b + c$, where a, b, and c are constants for different sections of radial ranges. Jung et al., 2018 calculated nano-scale RDDs around 2 and 5 nm-diameter GNPs irradiated by 50 kVp X-rays. They used two MC simulation codes, MCNP6.1 and Geant4-DNA, and found that the relative differences in calculated radial doses were under 20% at the GNP surface and less than 5% for the distance from 200 nm to 1 μm.

Sung and Schuemann, 2018 calculated nanoscale doses per single ionizing event near a single GNP of 1.9 nm diameter for a 150 kVp polychromatic X-ray beam. The dose was calculated in spherical shells of 1 nm thickness around the source. From the data presented in the double logarithmic scale, it follows that the calculated RDD can be approximately fitted by the power law function for distances between 1 nm and 1 mm from the NP center. Villagomez-Bernabe and Currell, 2019 calculated RDDs for three nanoagents – auranofin (a small molecule containing a gold atom), a 1 nm radius core GNP, and a 25 nm radius core GNP irradiated with a 6 MV clinical radiation beam. It was shown that independently of the nanoagent, the RDDs can be fitted well by the power law. Kirkby and Koger, 2010 calculated RDDs around spherical GNP of 25 nm radius exposed to monoenergetic photons with energies from 10 keV to 1 MeV. The calculated RDDs that were discussed in the previous subchapter are shown in Figure 2.6. As all presented above RDDs, the dose surrounding the GNP falls off roughly as a power law relation with an exponent between -1.9 and -2.5, out to the maximum range of the emitted secondary electrons.

As it follows from the pattern of energy released into the surrounding medium, most of the energy is deposited within a few hundred nm of the NP. Because of this highly localized dose deposition pattern, the specific location of each NP relative to any sensitive structures within the cell can play a critical role in determining an individual cell's response when irradiated in the presence of high-Z NPs. Furthermore, this high-dose localization suggests that a cell's overall energy deposition pattern can be quite heterogeneous. Therefore, sophisticated models that can account for the dose heterogeneity, the stochastic nature of the ionization events, and the stochastic arrangements of GNPs within cells may be required to accurately predict the cellular response (Schuemann et al., 2016).

2.3.3. Analytical consideration of RDD around a photon-irradiated NP

In contrast to a significant number of MC studies devoted to simulation RDD around irradiated NPs, analytical consideration of this problem is practically absent. To our knowledge, the only article by Chernov et al., 2012 presents an analytical approach that can be used for fast and inexpensive estimation of the dose distribution around a NP embedded in a medium. Below, a short description of the proposed approach and a set of corresponding analytical expressions are presented.

The approach considers the energy deposition by one secondary electron liberated at a certain point of the NP with the kinetic energy of E_0. During travel toward the NP surface, the electron losses energy and slows down. If E_0 is sufficiently high, the electron crosses the NP surface, continues to travel in the medium, and eventually stops. The radial dose distribution, D(r), around the irradiated GNP is defined as the average energy deposited in a spherical shell centered at the NP center with the radii between r and r + dr, normalized to its mass:

$$D(r) = -\frac{dE_{av}(r)}{4\pi r^2 \rho_w dr}, \tag{2.3.1}$$

where ρ_w is the surrounding medium (water) density, $E_{av}(r)$ is the average energy of escaped electrons at the distance r from the GNP center. The minus sign comes from the fact that $E_{av}(r)$ always decreases when r increases.

Using the continuous slowing down approximation (CSDA) and the supposition that emitted electrons travel in a straight-line path, the remaining electron's energy at the GNP surface E_s is determined by its initial energy E_0 and distance l that the electron travels in the GNP and can be found from the equation:

$$R_{NP}(E_s) = R_{NP}(E_0) - l, \tag{2.3.2}$$

Here the function $R_{NP}(E)$ is the electron range - energy relationship for a NP material that relates a residual range of an electron of energy E. Some empirical expressions that relate the electron range to its energy were proposed. For instance, over a limited energy range, a power law is often used (Cucinotta et al., 1995): $R(E) = aE^b$, where a is a coefficient independent of the energy and b is the exponent. As it is possible to see from Figure 2.5, the plot of electron ranges in water as a function of kinetic energy is presented in the double logarithmic scale. It can be approximated

between 1 and 500 keV by a straight line. This evidences that electron ranges in water can be fitted by the power law.

It is convenient to eliminate the coefficient a using the equation $R_{NP}(E_0) = aE_o^b$. This allows one to solve (2.3.2) with respect to E_s:

$$E_s\left(E_0, l\right) = E_0\left[1 - \frac{l}{R_{NP}(E_0)}\right]^{\frac{1}{b_{NP}}}. \tag{2.3.3}$$

A similar set of steps can be followed to find the rest of electron energy E_r at a radius r from the NP center, which is determined by its remaining energy E_{sr} and the distance d that the electron passes in the medium. Therefore, the energy E_r can be found from the implicit equation:

$$R_m\left(E_r\right) = R_m\left(E_s\right) - d\,, \tag{2.3.4}$$

where the function $R_m(E)$ is the electron range - energy relationship for a surrounding medium (water) and d is the distance that the electron passes in the medium to reach the sphere of radius r centered at the NP center.

The solution of the implicit equation (2.3.4) can be presented as:

$$E_r\left(E_0, l, d\right) = E_0\left\{\left[1 - \frac{l}{R_{NP}(E_0)}\right]^{\frac{b_m}{b_{NP}}} + \frac{d}{R_m(E_0)}\right\}^{\frac{1}{b_m}}. \tag{2.3.5}$$

The distance *d* is equal to

$$d = -R_{NP}\cos\alpha + \sqrt{r^2 - R_{NP}^2\sin^2\alpha}\,, \tag{2.3.6}$$

where R_{NP} is the NP radius and α is the angle at which an electron escapes the NP (relative to the normal of the NP surface).

The average energy of one escaped electron at the distance r from the NP center is determined as the average energy of all electrons escaping the NP surface (with an angle α measure from the normal to the surface) after traveling different distances l from their creation point:

$$E_{av}\left(r, E_0\right) = E_0 \iint\limits_{E_r(r,E_0,l,\alpha)>0} E_r(r, E_0, l, \alpha)\psi(l, \alpha)\,dl\,d\alpha\,. \tag{2.3.7}$$

Here ψ(l,α)dldα is the probability that the electron liberated at a certain internal point of the NP has passed the distance between l and l + dl in the NP and left the NP at an angle between

α and α + dα relative to the normal of the NP surface at the point of escape. The integral (2.3.7) is taken over that l and α, for which the energy in the integral is positive.

The function $\psi(l,\alpha)$ depends on the distribution of the knocked-out electrons over the NP volume and their travel directions. In the case of isotropic photon irradiation and negligible attenuation of the photon beam over the NP volume, all points inside the NP and all directions of motion of liberated electrons will be equivalent. This allows one to find the probability function ψ(l,α) by using a simple geometrical consideration that results as follows (Chernov et al., 2012):

$$\psi(l,\alpha) = \frac{3\sin\alpha\cos\alpha}{2a_0}. \qquad (2.3.8)$$

The length l takes values from 0 to the maximal value $2R_{NP}$. The angle α varies from 0 to the maximal value $\alpha_{max} = \arccos(l/2R_{NP})$.

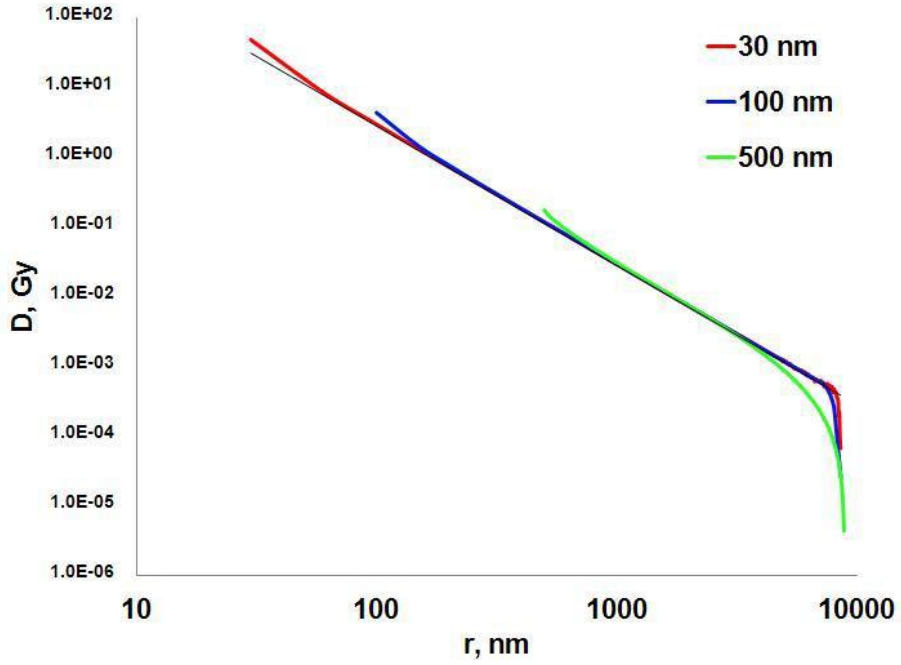

Figure 2.9. The dose distribution in the water around embedded gold NPs. The bold lines correspond to the additional dose delivered by one 19.7 keV electron liberated in the NPs of indicated radii. The thin line is the power fit with $D = 2.9\times10^4/r^2$ Gy, where *r* is the distance from the NP center in nm. Image borrowed from Chernov et al., 2012.

The derived expressions were applied to calculating the RDDs around 30, 100, and 500 nm radius GNPs embedded in water irradiated with 100 keV photons. Only secondary photoelectrons with an initial energy of 19.7 keV were considered. The calculated RDDs are shown in Figure 2.9.

It was shown that the dose distribution is close to the $1/r_2$ dependence and practically independent of the NP radius.

2.4. Radiobiological models describing the response of NP-loaded cells under X-rays irradiation

Prediction of radiobiological response is a major challenge in radiotherapy. Many phenomenological models have been developed to describe the response of cells under irradiation. Among several radiobiological models, the linear-quadratic (LQ) model has been best validated by experimental and clinical data (van Leeuwen et al., 2018). In this subchapter, we will consider radiobiological models, which relate the nanoscale energy deposition from photon-irradiated NPs to biological outcomes using the LEM extension of the LQ model.

2.4.1. Linear quadratic model

Cellular radiosensitivity was defined as the inability of irradiated cells to produce daughter colonies of cells. It is quantified experimentally by the clonogenic assays that consist in determining the number of colonies resulting from a given number of cells irradiated at a given dose. The survival fraction follows a decreasing exponential-like law; it is generally plotted on a semi-logarithm scale (Bodgi et al., 2016). Over time, different mathematical models have been proposed to describe the response of the cell cultures to the irradiation treatment through cell survival curves. These models center their hypothesis on the description of the basic interaction with the sensitive part of the target to obtain the survival of the irradiated cells. A comprehensive review of the mathematical model to describe radiation action on cells and relevant references can be found in the historical and critical review by Bodgi et al. 2016.

The LQ model, which may be the most important and most employed biomathematical model in radiotherapy, describes the surviving fraction of a population of irradiated cells dependence on the absorbed dose D as:

$$S = \exp\left(-\alpha D - \beta D^2\right), \tag{2.4.1}$$

where α and β are the dose independent parameters.

The LQ model was derived by Chadwick and Leenhouts., 1973. They proposed that the linear component (αD) represents cell death due to a single lethal hit to the DNA and that the quadratic (βD^2) component represents cell death that only happens with two hits. However, it is clear that this mechanism is incorrect, and the biological interpretation of the LQ parameters is unclear (Bodgi et al., 2016). Clinically, the LQ model is mainly used to estimate equivalent radiotherapy schedules (e.g., calculate the equivalent dose in 2 Gy fractions), but increasingly also to predict tumor control probability (TCP) and normal tissue complication probability (NTCP) using logistic models. Therefore, selecting accurate LQ parameters is pivotal for a reliable estimate of radiation response. An overview of published values of estimates of α, β and α/β, stratified by tumor site is presented in the review by van Leeuwen et al., 2018.

Several modifications of the LQ model have been proposed over the years, aiming to include hypoxia radio-resistance or high-dose modifications (Neira et al., 2020). The LQ model is highly empirical and not comprehensive. It does not attempt to correlate microscopic effects with cell survival rate and formally is not a mechanistic model. However, in the literature, there have been various attempts at mechanistic modeling of radiation responses (McMahon, 2019; McMahon and Prise, 2019).

2.4.2. Local effect model

The standard LQ model assumes a homogeneous dose distribution over the irradiated cells. On the other hand, the local effect model (LEM) is typically used to consider a heterogeneous dose distribution over irradiated cells. The LEM was initially developed for heavy ion therapy aiming to predict the effects of high-LET radiation based on the known effects of low-LET radiation (photons) in combination with the characterization of the inhomogeneous, localized energy deposition pattern of charged particles (Scholz et al., 2020). The LEM uses the concept of "local dose," defined as the expectation value of the energy deposition at any position in the radiation field for a given pattern of particle trajectories. The main assumption of the LEM is that equal local doses should lead to equal local effects, independent of the radiation quality. The basic formulation of the LEM, presented below, can be found in the article by Elsässer and Scholz.

The LEM is based on the assumption that the biological effect of radiation is determined entirely by the spatial local dose distribution inside the cell nucleus. Furthermore,

since biological damage mainly results from secondary electrons, which are generated by photons as well as ions, the damage caused by heavy ions can be derived from the corresponding experiments with X-rays.

The accumulated local dose from different ion tracks can be calculated individually for small subvolumes using a simple amorphous track structure model. The number of lethal events *N* after X irradiation follows Poisson statistics since, due to the energy deposition pattern of photons, the lethal events are expected to be distributed randomly in the sensitive target. Therefore, the fraction of surviving cells after X irradiation can be written as

$$S_x\left(D\right) = e^{-N_x(D)}, \tag{2.4.2}$$

where $S_x(D)$ is the result of a measurement and the average number of lethal events $N_x(D)$ generated by photons is readily derived by

$$N_x\left(D\right) = -\ln S_x\left(D\right). \tag{2.4.3}$$

Additionally the dose-dependent event density for X irradiation, $\nu_x(D)$ is introduced:

$$\nu_x\left(D\right) = \frac{N_x\left(D\right)}{V}, \tag{2.4.4}$$

with *V* being the target volume.

For particle radiation, the dose distribution is highly inhomogeneous, and the three-dimensional local dose d(x,y,z) to calculate the average number of lethal events generated by ions must be considered:

$$N_{ion} = \int_{V_{nucleus}} \nu_{ion}\left[d\left(x,y,z\right)\right]dV, \tag{2.4.5}$$

where ν_{ion} denotes the lethal event density after ion irradiation. According to the main idea of the local effect model, the local dose effect is independent of the radiation quality and $\nu_{ion}(d) = \nu_x(d)$. Using (2.4.3) and (2.4.4), the average number of lethal events generated by ions can be rewritten as:

$$N_{ion} = \int_V \ln S_x\left[d\left[x,y,z\right]\right]\frac{dV}{V}. \tag{2.4.6}$$

Equation (2.4.6) represents the most general formulation of the LEM and illustrates the dependence of particle radiation's biological effect on the photon radiation's damage efficiency. Figure 2.10 shows a sketch of the calculation using (2.4.6). The positions of ion tracks

are distributed randomly over the cell nucleus following Poisson statistics, with the average number of traversals as the mean value of the Poissonian.

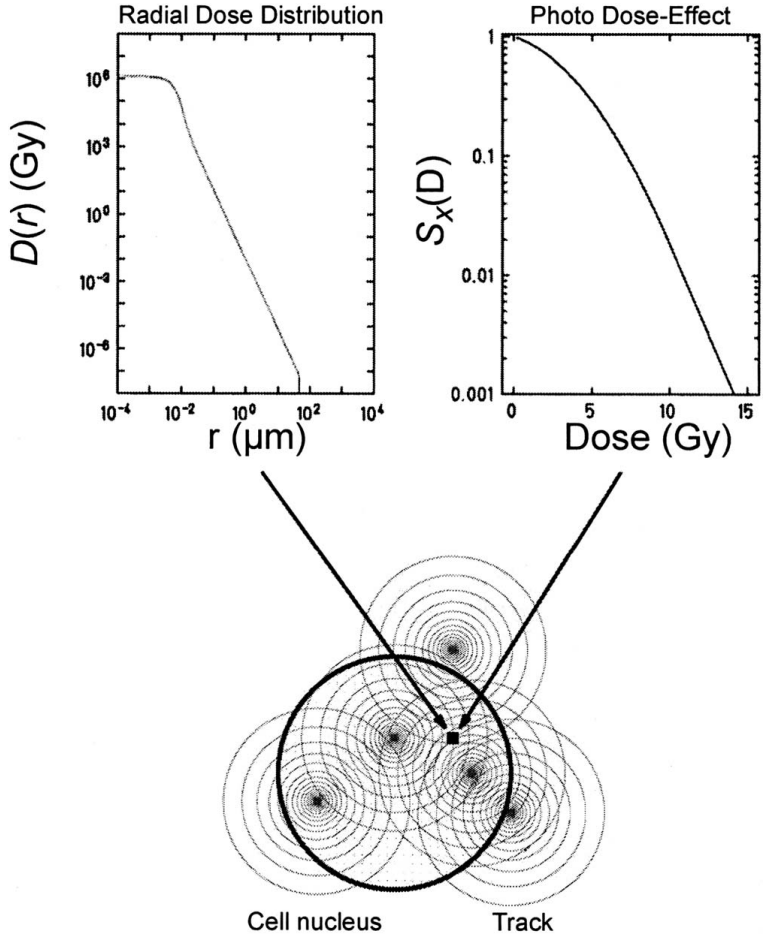

Figure 2.10. The dose is calculated at each position in the cell nucleus by simulating a number of ion traversals according to the desired fluence. The contribution of individual tracks is determined with the help of a simple radial dose distribution. The resulting local damage is taken from the experimental data for photon irradiation. Image borrowed from Elsässer and Scholz., 2007.

2.4.3. LEM extension of the LQ model for NP-loaded cells

As discussed in the previous subchapter, the LEM allows one to consider a heterogeneous distribution of dose around the trajectory of heavy charged particles. Methodologically, the dose distribution around a photon-irradiated NP could be considered the same way as around heavy charged particles. Therefore, the formulas derived in the LEM could be directly applied to the evaluation of the biological outcomes of the photon-irradiated NPs. Some articles present the NP extension of the LEM (McMahon et al., 2011a; McMahon et al., 2011b; Lechtman et al., 2013;

Lin et al., 2015; Brown and Currell, 2017; Ferrero et al., 2017). Below, a short description of these articles is presented.

McMahon et al., 2011a, were the first, who assume that the lesion density induced by a given microscopic dose is the same as that induced by sparsely ionizing radiation and have used Eq. (2.4.6) for calculation of the total number of lesions and prediction of the radiation response in the presence of GNPs. The RBE values predicted by them for irradiated MDA-MB-231 cells with monoenergetic X-rays photons in the presence of 0.5 mg/g of GNPs are shown in Figure 6.5. In a similar work, McMahon et al., 2011b, extended the model to consider 6 and 15 MV X-ray sources to determine if similar sub-cellular dose localization may be responsible for the experimentally observed ability of GNPs to sensitize cells to megavoltage radiation. They have modeled a GNP (2 nm diameter) embedded in a water volume and have found the dose distribution around the GNP. The dose distribution throughout a cell was then taken as a combination of a uniform background resulting from the X-ray dose (without GNPs) and sharp spikes resulting from the addition of GNPs, assuming their uniform distribution.

The model was applied to MDA-MB-231 cells, whose radiation response, both with and without GNPs, had been previously measured (Jain et al., 2011), and is plotted as the solid lines through the 'No Gold' data points in each panel of Figure 2.11. By combining the nanoscale dose distributions and ionization rates, predictions of the radiosensitizing effects of GNPs were obtained using the LEM. Corresponding curves are plotted as dashed lines through the 'With Gold' data points in each panel of Figure 2.11. It can be seen that the predicted (dashed) curves are in good agreement with the experimentally measured points. This suggests that the NP-extended LEM is a useful approach for predicting the radio-sensitizing effects of GNPs.

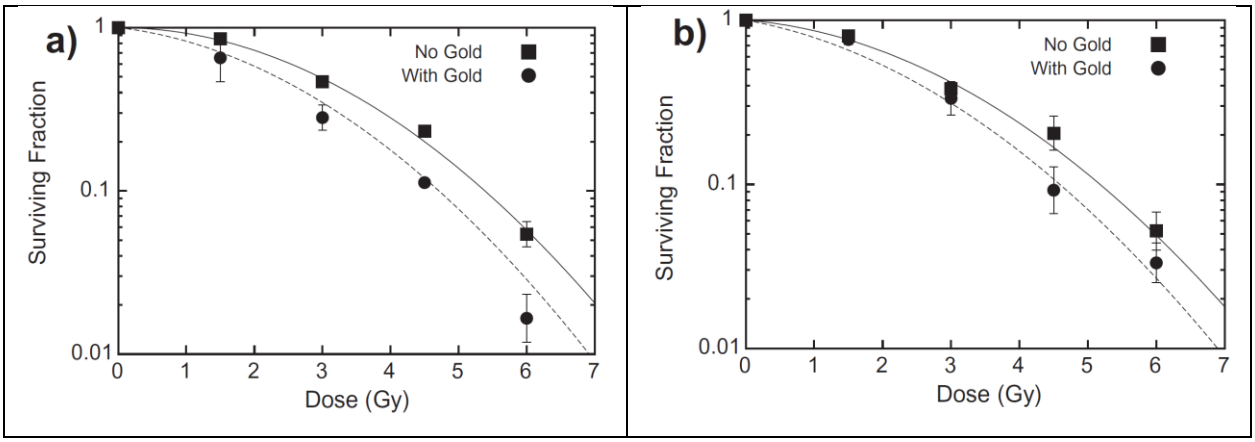

Figure 2.11. Comparison of LEM predictions and observed experimental results for MDAMB-231 cells exposed to 6 (left) and 15 (right) MV radiation, with and without GNPs. Points are measured values (squares: control, circles: with gold) from Jain et al., 2011. The solid line is a fit to the control cell response curve, while the dashed line is the LEM prediction for the radiation response in the presence of GNPs. Image borrowed from McMahon et al., 2011a

Lechtman et al., 2013 developed a radiosensitization predictive model, which considers the detailed energy deposition at the nano-scale. Detailed MC simulations were conducted, producing individual tracks of photoelectric products escaping GNPs, and energy deposition was scored in nano-scale voxels in a model cell nucleus. Cell survival was determined similarly to the LEM (Kraft et al., 1999) by integrating the radiation-induced lethal event density over the nucleus volume using Eqs. (2.4.2) and (2.4.6). The model was found to coincide well with experimental cell survival. Two fundamental distinctions from the LEM were incorporated. The first involves a more detailed simulation of the energy deposition at the sub-cellular scale rather than representing the energy deposition as a radial dose function (Kraft et al., 1999) or scoring dose in radial bins (McMahon et al., 2011a). This provides additional information on the Auger cascade and avoids variations in the calculation of dose associated with the increasingly large concentric volumes further away from the AuNP (Lechtman et al., 2011). Another distinction of the proposed model is the calculation of lethal event density within finite-sized voxel elements. Instead of a point response approach, this method may better represent radiobiological mechanisms that occur over finite distances, such as diffusion of free radicals, double-strand breaks, multiply damaged sites, and clustered effects.

Lin et al., 2015 applied the LEM and Eqs. (2.4.2) and (2.4.6) to describe the change in survival of irradiated MDA-MB-231 breast cancer cells and DU145 prostate cancer cells due to the radiosensitizing effect of GNPs irradiated with kV and MV photon beams. They considered

five GNP distribution geometries shown in Figure 2.12 and concluded that, in general, GNPs located inside of the cell nucleus contribute most significantly to cell killing.

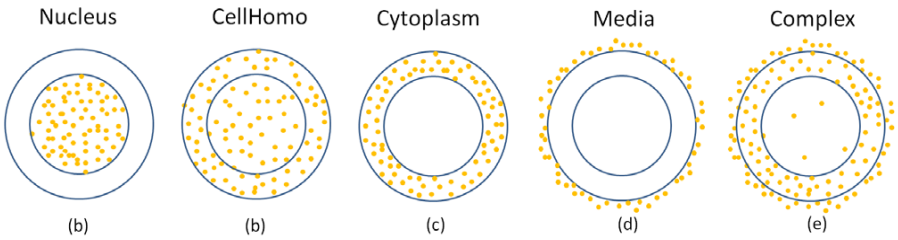

Figure 2.12. The cell geometry and five GNP distributions were used by Lin *et al.* 2015 as input for the GNP-LEM. (a) Nucleus geometry, GNPs randomly distributed in the cell nucleus. (*b*) CellHomo geometry, GNPs randomly distributed in the whole cell. (*c*) Cytoplasm geometry, GNPs randomly distributed in the cytoplasm. (*d*) Media geometry, GNPs randomly distributed in the extracellular media. (*e*) Complex geometry, GNPs randomly distributed inside the cell and extracellular media with the same concentration. Within the cell, 90% of GNPs randomly distributed in the cytoplasm and 10% of GNPs distributed in the whole cell volume, including the nucleus region. Image borrowed from Lin et al., 2015.

Brown and Currell, 2017 developed a LEM-based framework capable of interpolating nanoparticle-enhanced photon-irradiated clonogenic cell survival fraction measurements as a function of NP concentration. Based on the supposition that the spatial distribution of NP uptake within the cell line remains approximately constant with concentration. They proposed that the mean number of lethal lesions generated via high Z NP action at a concentration C can be scaled to that at the known reference concentration C_0:

$$\left\langle N_{NP}(C,D)\right\rangle \approx \frac{C}{C_0}\left\langle N_{NP}(C_0,D)\right\rangle, \tag{2.4.7}$$

As a result, the final form of the interpolation framework presents the survival fractions for cells loaded with NPs to concentration C:

$$SF[C,D] = \exp\left(-\left(\alpha_U + \frac{C}{C_0}\Delta\alpha\right)D - \left(\beta_U + \frac{C}{C_0}\Delta\beta\right)D^2\right), \tag{2.4.8}$$

where α_U and β_U are the linear-quadratic parameters describing the survival of cells (Eq. 2.4.1) without NPs; $\Delta\alpha$ and $\Delta\beta$ are the change of the parameters caused by NPs of concentration C_0.

This developed framework was experimentally benchmarked for GNP-doped bovine aortic endothelial cells under external kilovoltage X-ray irradiation. It was illustrated that the

performance of the developed framework is directly dependent on the quality of experimental input data.

Ferrero et al., 2017 developed a relatively simple approximation of the LEM called the Additive Model (LEM-AM). According to the LEM, the expected number of lethal lesions for a specific cell, $\overline{N}_{leth}$, resulting from the inhomogeneous energy deposition pattern induced by the GNP secondary emitted particles is obtained by evaluating the local dose at each point of the cell nucleus and then integrating over the whole volume

$$\overline{N}_{leth} = \frac{1}{V_t}\int_{V_N}\left(\alpha_\gamma \sum_{i=1}^{N_{NP}} D_j^{NP}\left(\vec{r}_j,\vec{r}\right) + \beta_\gamma\left(\sum_{i=1}^{N_{NP}} D_j^{NP}\left(\vec{r}_j,\vec{r}\right)\right)^2\right)d\vec{r}\,, \tag{2.4.9}$$

where $D_j^{NP}\left(\vec{r}_j,\vec{r}\right)$ is the inhomogeneous dose contribution from the j-th nanoparticle, whose center is located at point r_j, N_{NP} is the number of nanoparticles, and V_N is the volume of the cell nucleus. α_γ and β_γ represent the experimentally observed LQ parameters for the control irradiation, that is, for cells irradiated without of NPs.

The first simplification was introduced by considering the contribution of different nanoparticles in a cell as nonsynergistic. This assumption is supported by the fact that the ionization rates estimated from the Monte Carlo simulation are meager. This leads to a negligible probability of having the local dose distributions due to secondary electrons emitted from two or more different nanoparticles overlapping. Implying that the expected total number of lethal events in a cell can be approximated by summing the lethal events associated with each GNP evaluated independently (i.e., by interchanging the order of summation and integration in Eq. 2.4.9)

$$\overline{N}_{leth} \simeq \frac{1}{V_t}\sum_{i=1}^{N_{NP}}\int_{V_N}\left(\alpha_\gamma D_j^{NP}\left(\vec{r}_j,\vec{r}\right) + \beta_\gamma\left(D_j^{NP}\left(\vec{r}_j,\vec{r}\right)\right)^2\right)d\vec{r} = \sum_{i=1}^{N_{NP}}\overline{N}_{leth}\left(i_j\right). \tag{2.4.10}$$

where the notation $\overline{N}_{leth}\left(i_j\right)$ indicates the number of lethal events associated with the j-th nanoparticle, identified by the index j, that has experienced i_j ionization events. Explicitly, for a nanoparticle inside the nucleus, the radial symmetry of the dose can be exploited and $\overline{N}_{leth}\left(i_j\right)$ can be evaluated as

$$\overline{N}_{leth}\left(i_j\right) \simeq \frac{4\pi}{V_N}\int i_j \times r^2\left(\alpha_\gamma D^{NP}\left(r\right) + \beta_\gamma\left(D^{NP}\left(r\right)\right)^2\right)dr\,, \tag{2.4.11}$$

where $D^{NP}(r)$ is the radial dose per ionization event per GNP, we remark that the number of ionization events i_j is a stochastic variable varying among the nanoparticles, i_j =(0, 1, 2; …). Due to the low probability of ionization per Gy for a single nanoparticle, the majority of the i_j, and hence of the $\overline{N}_{leth}\left(i_j\right)$, is expected to be zero.

Taking into account that $\overline{N}_{leth} = \overline{N}_{leth}\left(D\right)$ implicitly depends on the nominal dose D due to primary photons, the resulting survival probability associated with the NP ionizations is then evaluated assuming Poisson statistics for N_{leth} and can be written as

$$S_{NP}\left(D\right) = \exp\left(-\overline{N}_{leth}\left(D\right)\right). \tag{2.4.12}$$

The second simplification is the supposition that a single GNP ionization event is very effective in killing the cell and that the survival probability can be directly derived from Poisson statistics, being the probability to observe 0 ionizations:

$$S_{NP} \simeq \exp\left(-\overline{N}_{ion}\right) = \exp\left(-\overline{N}^{0}_{ion}\,\overline{N}_{NP}D\right). \tag{2.4.13}$$

where $\overline{N}_{ion} = \overline{N}_{ion}\left(D\right) = \overline{N}^{0}_{ion}\,\overline{N}_{NP}D$ is the expected dose dependent number of ionizations per cell.

The resulting LQ parameters for the net survival can be written as:

$$\begin{aligned}\alpha &= \alpha_{\gamma} + \overline{N}^{0}_{ion}\,\overline{N}_{NP}\\ \beta &= \beta_{\gamma}\end{aligned}, \tag{2.4.14}$$

The proposed simplified LEM formulation was validated with MDA-MB-231 cell survival curves for 160 kVp, 6, and 15 MV photon beams (Jain et al., 2011). Cells treated with gold concentrations varying from 0 (control) to 24 μM. A simultaneous fit of the survival curves for the irradiated cell treated with a gold concentration of 12 μM was conducted, leaving only the average number of GNPs inside the cell nucleus as the free parameter, whose best fit value is N_{GNP} = (5.0 ± 0.3)×10^5. The empirical and simulated cell responses were found to coincide well.

CHAPTER 3

Analytical approach for quantification of the radiosensitization effect (general scheme)

The main objective of the theoretical study of radiation therapy assisted with high-Z NPs is to estimate the survival of tumor cells loaded with NPs and exposed to ionizing radiation by external or internal radiation sources. As was described in the literature survey (subchapter 2.1.1), three almost independent subsequent stages should be described to quantify the cell survival after irradiation (Zygmanski et al., 2013a; Zygmanski et al., 2013b; Zygmanski and Sajo, 2016).

The first stage simulates the radiation transport from a radiation source to a tumor region. Typically, macroscopic MC simulations of radiation transport for clinical beams are performed to relate the spectral characteristics of the incident beam to the photon fluence at the tumor location. In the second stage, this fluence is used as the input radiation source for new simulations that allow one to describe the interaction of photons with NPs and to calculate the dose distribution around a single NP or its clusters. Finally, the third stage relates the cell survival probability with the distribution of dose deposited in cell targets after irradiation of the cell loaded with NPs.

In this chapter, we will develop a general approach accounting for the sharply inhomogeneous dose distribution within a single cell and its surroundings due to the presence of NPs and derive analytical expressions for evaluating the cell survival curve. Similar to Zygmansky et al., 2013a, we will assume that all cells and the embedded NPs do not disturb the incident photon beam and are exposed to the same irradiation dose. As a result of this assumption, we will avoid the first stage mentioned above and suppose that the photon fluence delivers a homogenous dose of D_0 to a cell without NPs. The second stage will be reduced by us to calculate the number of photon interactions with NPs and to simulate by MC the RDD around those NPs that were ionized by impinging photons. Finally, the focus will be mainly on the third stage. We will derive general expressions for the average number of lesions and the survival probability of irradiated cells loaded with high-Z NPs.

3.1 Quantification of NP concentration in a cell

Accurate quantification of the spatial distribution of NPs in the cell and the cell targets is essential for predicting the NP's impact on cell survival. However, it is a challenging problem because, at the present stage of high-Z NP radiotherapy, the spatial distribution of NPs and their clustering cannot be easily controlled or even experimentally determined (Zygmanski et

al., 2013a). The quantification includes accurately determining the NP size, aggregate state, and number concentration. It is a challenging problem arising from the heterogeneity of NPs, which also highlights a key distinction between chemistry and nanotechnology. In nanotechnology, NPs are often considered artificial atoms or artificial molecules, while, in fact, they are as individual as people's prints (Shang and Gao, 2014). Despite this, here we will consider a heterogeneous mixture of identical NPs in a medium.

Based on this concept and assuming one NP as an artificial molecule, the total number of NPs in a cell, N_{NP} can be determined as:

$$N_{NP} = \frac{m_{NP}}{M_{NP}}, \tag{3.1.1}$$

where m_{NP} is the total mass of NPs and M_{NP} is the mass of one NP.

Three quantities are commonly used to indicate the concentration of NP in a cell or cell target. The number concentration of NPs, $C_{NP,n}$ determines the number of NPs per unit volume (in NPs/L or NPs/cm^3):

$$C_{NP,n} = \frac{m_{NP}}{M_{NP}V_c}, \tag{3.1.2}$$

where V_c is the volume of the mixture.

The molar concentration or molarity, $C_{NP,m}$, express the number of moles of the NP substance per liter (in M, μM or nM):

$$C_{NP,m} = \frac{m_{NP}}{M_{NP}N_A V_c}, \tag{3.1.3}$$

where N_A is the Avogadro constant.

The NP concentration in a cell or a cell target is often indicated as a mass fraction of the NP substance in water, $C_{NP,w}$ (in mg/g or mg/mL). Usually, NP concentration is sufficiently small, and the cell density is close to that of pure water, ρ_{water}. In this case

$$m_{NP} = \rho_{water} V_c C_{NP,w}, \tag{3.1.4}$$

and, assuming that all NPs have the same volume V_{NP} the number and molar concentrations can be related to the mass fraction:

$$C_{NP,n} = \frac{\rho_m}{\rho_{NP}V_{NP}} C_{NP,w}, C_{NP,m} = \frac{\rho_m}{\rho_{NP}V_{NP}N_A} C_{NP,w}. \tag{3.1.5}$$

Each of these three quantities can be used to quantify the NP concentration in a cell. The weight fraction depends only on the total amount of NPs in the cell and can be determined by suitable experimental techniques, for instance, by inductively coupled plasma mass spectrometry (Noireaux et al., 2019). To determine the other two quantities, it is necessary to know the NP mass, which can only be estimated from the NP's composition, volume, and crystal structure. NP volume is determined by its shape and size, which can be found by various methods, including TEM, X-ray diffraction, extended X-ray absorption fine structure, probe molecule absorption, magnetic measurements, optical absorption, dynamic light scattering, and small-angle neutron scattering (Pyrz and Buttrey, 2008). Each technique has advantages and disadvantages, but only TEM currently allows one the direct visualization of NPs.

3.2 Probability of ionization of a single NP per irradiation dose (analytical approach)

The probability of ionization in a single NP embedded in a cell is directly proportional to the prescribed dose D_0 and can be found similarly to the method described by (Ngwa et al., 2010 ; Hossain and Sum, 2012; Rabus et al., 2019). Let us suppose that a certain volume of water with a single NP is irradiated with the homogeneous photon fluence

$$\Phi = \int_0^\infty \frac{d\Phi}{dE_{ph}}\left(E_{ph}\right) dE_{ph}\,, \tag{3.2.1}$$

where $d\Phi/dE_{ph}$ is the energy distribution of the fluence or spectral fluence (particles per area per energy interval) and E_{ph} is the photon energy.

Considering the NP as a material with atomic number Z of uniform density, the mean number of photon interactions per NP atom in a certain small volume subjected to incident photons with energies between E and E + dE can be found from the definition of the cross-section presented in ICRU report 85 (ICRU85, Eq. 4.1.1):

$$\frac{dN_{\text{int}}\left(E_{ph}\right)}{dE_{ph}} = \sigma_Z\left(E_{ph}\right)\frac{d\Phi}{dE_{ph}}\left(E_{ph}\right), \tag{3.2.2}$$

where $\sigma_Z(E_{ph})$ is the total cross section of photon interaction with the chemical element atom.

The total number of atoms in a NP is equal to

$$N_{NP} = \rho_{NP} V_{NP}\,\frac{N_A}{M}\,, \tag{3.2.3}$$

where M is the molar mass of the NP material.

Supposing that the fluence is the same over the NP volume, the mean number of photon interactions per NP per energy interval can be presented as follows:

$$\frac{dN_{\mathrm{int},NP}\left(E_{ph}\right)}{dE_{ph}} = \rho_{NP} V_{NP} \frac{\sigma_Z\left(E_{ph}\right) N_A}{M} \frac{d\Phi}{dE_{ph}}\left(E_{ph}\right). \tag{3.2.4}$$

By definition (ICRU85, Eq. 4.2.1), the product of $\sigma_Z(E)$ and N_A/M is the mass attenuation coefficient, $[\mu(E_{ph})/\rho]_{NP}$ of the NP material, thus

$$\frac{dN_{\mathrm{int},NP}\left(E_{ph}\right)}{dE_{ph}} = \rho_{NP} V_{NP} \left[\mu\left(E_{ph}\right)/\rho\right]_{NP} \frac{d\Phi}{dE_{ph}}\left(E_{ph}\right). \tag{3.2.5}$$

The total mean number of photon interactions in the NP volume irradiated with the homogeneous photon fluence can be found by the integration of (3.2.5) over the photon energy:

$$N_{\mathrm{int},NP} = \rho_{NP} V_{NP} \int_0^\infty \left[\mu\left(E_{ph}\right)/\rho\right]_{NP} \frac{d\Phi}{dE_{ph}}\left(E_{ph}\right) dE_{ph}. \tag{3.2.6}$$

For a monoenergetic photon beam of energy E_0, $d\Phi/dE_{ph} = \delta(E_{ph} - E_0)$ and Eq. (3.2.6) is simplified to:

$$N_{\mathrm{int},NP}\left(E_0\right) = \rho_{NP} V_{NP} \left[\mu\left(E_0\right)/\rho\right]_{NP} \Phi\left(E_{ph}\right). \tag{3.2.7}$$

Direct calculations (see subchapter 5.2) and the data from the literature (Ferrero et al., 2017; Lechtman et al., 2013; Lin et al., 2015; McMahon et al., 2011a; Melo-Bernal et al., 2018; Sung et al., 2017) show that the mean number of photon interactions in a single NP is very low for doses used in the radiotherapy. This means that the number of interactions with any single NP is expected to be only zero or one, and Eqs. (3.2.6) and (3.2.7), in fact, present the ionization probability of one NP irradiated with a given photon fluence Φ.

Relating the number of photon interactions to the absorbed dose delivered in pure water (without NPs) is important. In conditions of secondary electron equilibrium, the absorbed dose is closed to the kerma, therefore for a polyenergetic photon beam (ICRU85, p. 24, Eq. 5.1.2)

$$D_0 \approx K = \int_0^\infty E_{ph} \left[\mu_{en}\left(E_{ph}\right)/\rho\right]_w \frac{d\Phi}{dE_{ph}}\left(E_{ph}\right) dE_{ph}, \tag{3.2.8}$$

where $[\mu_{en}(E_{ph})/\rho]_w$ is the energy-absorption coefficient of water, which is supposed to be equal to the mass energy-transfer coefficient.

Dividing (3.2.6) by (3.2.8) gives the probability of ionizations in a single NP per irradiation dose, P_{Gy} for a polyenergetic photon beam:

$$P_{Gy} = \frac{N_{\text{int},NP}}{D_0} = \frac{\rho_{NP} V_{NP} \int_0^{\infty} \left[\mu\left(E_{ph}\right)/\rho \right]_{NP} \frac{d\Phi}{dE_{ph}}\left(E_{ph}\right) dE_{ph}}{\int_0^{\infty} E_{ph} \left[\mu_{en}\left(E_{ph}\right)/\rho \right]_{w} \frac{d\Phi}{dE_{ph}}\left(E_{ph}\right) dE_{ph}}, \tag{3.2.9}$$

For monoenergetic photon beam of energy E_0 Eq. (3.2.9) is simplified to:

$$P_{Gy}\left(E_0\right) = \frac{\rho_{NP} V_{NP} \left[\mu\left(E_0\right)/\rho \right]_{NP}}{E_0 \left[\mu_{en}\left(E_0\right)/\rho \right]_{w}}. \tag{3.2.10}$$

As it follows from Eqs. (3.2.9) and (3.2.10), the probability of ionizations is directly proportional to the NP mass and inversely proportional to the photon energy. Another crucial factor is the ratio of the NP material's mass attenuation coefficient to the water's mass energy-transfer coefficient. The mass attenuation coefficient of gold and the mass energy-transfer coefficient of water are shown in Fig. 3.1. The points represent the tabulated data obtained from the National Institute of Standards and Technology (https://www.nist.gov/pml/x-ray-mass-attenuation-coefficients). The solid lines present the intermediate data calculated by linear interpolation in the double logarithmic scale (https://physics.nist.gov/PhysRefData/FFast/Text1995/chap08.html).

The photon energy dependence of the coefficients' ratio is shown in the inset of Fig. 3.1. The ratio strongly depends on the photon energy and can be approximately described by a bell-shaped curve between 5 and 500 keV. Additionally, a sharp peak at 80.7 keV due to the strong growth of photon absorption near the K-edge of gold is observed.

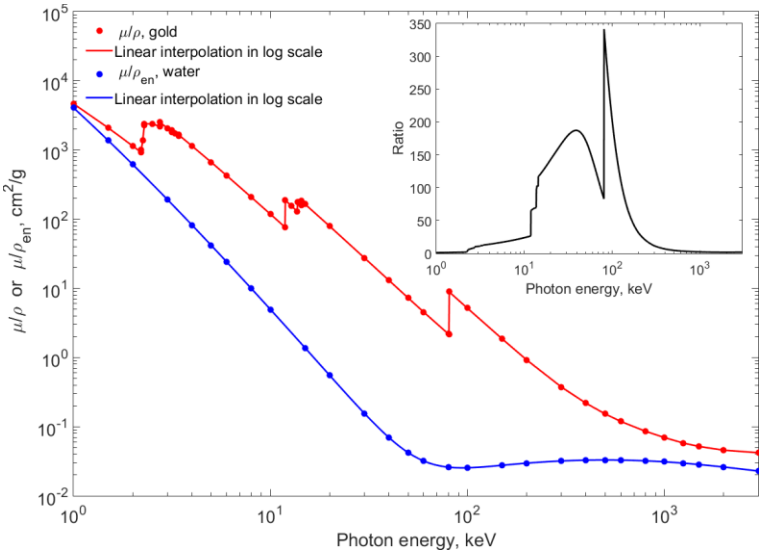

Figure 3.1. The mass attenuation coefficient of gold and the mass energy-transfer coefficient of water as a function of photon energy. The inset shows the ratio of the coefficients.

3.3 LEM extension of the LQ model for NPs loaded cells

Among a number of models proposed to predict radiobiological response, the LQ model is the best validated by experimental and clinical data and the most used for the representation of the cell response to the irradiation treatment, to estimate equivalent radiotherapy schedules, to predict tumor control probability and normal tissue complication probability (van Leeuwen et al., 2018). The basic LQ model presents the fraction of surviving cells S as a function of the delivered dose D in the following form:

$$S(D) = \exp(-N_{les}) = \exp(-\alpha D - \beta D^2), \tag{3.3.1}$$

where α and β are the LQ model parameters.

The number of lethal events, N_{les}, is the average number of lethal events formed in cellular or subcellular targets (entire cell, cell nucleus, DNA, clonogenic cancer or endothelial cells). It is a quantity representative of a large number of cells irradiated with the same dose D (Zygmanski et al., 2013a; Friedrich et al., 2012). The standard LQ model assumes a homogeneous dose distribution over the irradiated cells. To take into account a heterogeneous distribution of dose around an ionized NP, the LEM is typically used. The LEM is based on the principal assumption that in the local biologic effect, $N_{les}\left[D_t(\vec{r})\right]d\vec{r}$, the number of lethal events in a small subvolume

$d\vec{r}$ of the cell, is determined by the expected value of the local dose $D_t\left(\vec{r}\right)$ deposited in this subvolume (Elsässer et al., 2008). Similarly to the heavy ion version of LEM, the average number of lesions formed by photon radiation assisted with NPs can be expressed as an integral over the cell target:

$$N_{les,NP} = \frac{1}{V_t}\int N_{les}\left[D_t\left(\vec{r}\right)\right]d\vec{r} = -\frac{1}{V_t}\int \log S_{ph}\left[D_t\left(\vec{r}\right)\right]d\vec{r}, \tag{3.3.2}$$

where S_{ph} denotes the photon dose–response curve in (3.3.1) and V_t is the cell target volume.

Equation (3.3.2) is the most general formulation of the NP version of the LEM. It links the biological effect of the reference photon radiation (without NPs) and any additional radiation created by the NPs. The second part of the equation is expressed in terms of the survival dose response of the cell without NPs. The effect produced by the NPs is included in the inhomogeneous local dose distribution $D_t(\vec{r})$, which is determined by a given distribution of NPs over cells. Using the LQ model for the photon dose-response curve (3.3.1), the average number of lesions for a cell loaded with NPs (3.3.2) can be rewritten as:

$$N_{les,NP} = \frac{1}{V_t}\int\left[\alpha D_t(\vec{r}) + \beta D_t^2(\vec{r})\right]d\vec{r}\,. \tag{3.3.3}$$

Similar to ICRP publication 92 (Valentin, 2003, p. 89), one can suppose that the survival curve for cells with NPs exposed to the prescribed photon dose D_0 can be expressed in terms of a modified LQ response:

$$S_{NP}(D_0) = \exp\left(-N_{les,NP}\right) = \exp(-\alpha_{NP}D_0 - \beta_{NP}D_0^2), \tag{3.3.4}$$

where α_{NP} and β_{NP} are the new NP-related LQ model parameters that quantify the decrease of the cell survival due to the increase of deposited dose in a cell culture with embedded NPs.

3.4 Dose distribution in a cell loaded with NPs.

Let us consider a cell loaded with high-Z NPs and suppose that the dose distribution around the ionized NP is spherically symmetric and is described by a monotonously decreasing function $D_{NP}(r)$, where r is the distance from the NP center. We also assume that the cell nucleus is the critical target and use a coordinate system with the origin located at the nucleus center. The local dose deposited at a certain point $\vec{r}$ of the cell target by an ensemble of NPs within or/and close to

a cell is equal to the sum of the prescribed dose D_0 from an external source of photons and the additional local dose from all ionized NPs:

$$D_t\left(\vec{r}\right) = D_0 + \sum_{j=1}^{N_{NP}} n_{ion,j} D_{NP}\left(\left|\vec{r} - \vec{r}_j\right|\right), \tag{3.4.1}$$

where $n_{ion,j}$ is the number of photon interactions with a NP in the point $\vec{r}_j$, and N_{NP} is the total number of NPs in the cell.

The probability of ionization in a single NP embedded in water is directly proportional to the dose D_0:

$$P_{ion} = P_{Gy} D_0, \tag{3.4.2}$$

where P_{Gy} is the probability of ionization of a single NP per Gy described in the subchapter 3.2.

For clarity, we will refer to all NPs that have interacted with photons after delivering the dose D_0 as ionized NPs, keeping in mind that, in fact, the ionized NPs quickly return to the neutral state after emitting secondary electrons and photons. The total number of ionized NPs that affect the target is proportional to the prescribed dose and can be presented as

$$N_{ion} = P_{Gy} D_0 N_{NP}. \tag{3.4.3}$$

The literature data (see subchapter 2.3.2) and our calculations (subchapter 5.2) show that the probability of ionization per NP per Gy is very low; therefore, the number of interactions with any single NP is expected to be only zero or one. This allows us to consider only those NPs that have interacted with impinging photons only once and to rewrite (3.4.1) as follows:

$$D_t\left(\vec{r}\right) = D_0 + \sum_{j=1}^{N_{ion}} D_{NP}\left(\left|\vec{r} - \vec{r}_j\right|\right). \tag{3.4.4}$$

The summation in (3.4.4) is taken over the ionized NPs only and implicitly includes all information about the spatial distribution of NPs in cells. As was underlined by Elsässer and Scholz (2010), the term ‘‘local dose’’ in the LEM refers to the expected value of the dose deposition on the nanometer scale rather than the actual dose distribution. In that sense, the additional local dose related to a NP in the point $\vec{r}_j$, $D_{NP}\left(\left|\vec{r} - \vec{r}_j\right|\right)$, represents the average over a large number of individual dose distributions deposited by various secondary electrons ejected from NPs by impinging photons. It could be considered a unique function for all NPs having the same shape and size.

3.5 Average number of lethal lesions and the survival probability

The average number of lesions formed in the cell target can be obtained, in accordance with (3.3.3), by integration of $D_t\left(\vec{r}\right)$ and $D_t^2\left(\vec{r}\right)$ over the entire cell target volume:

$$N_{les,NP} = \frac{\alpha}{V_t}\int\left[D_0 + \sum_{i=1}^{N_{ion}} D_{NP}\left(\left|\vec{r}-\vec{r}_i\right|\right)\right]d\vec{r} + \frac{\beta}{V_t}\int\left[D_0 + \sum_{i=1}^{N_{ion}} D_{NP}\left(\left|\vec{r}-\vec{r}_i\right|\right)\right]^2 d\vec{r}\,. \qquad (3.5.1)$$

Expanding square brackets and interchanging the order of summation and integration in (3.5.1), the average number of lesions can be present as a sum of three terms:

$$N_{les,NP} = N_{les,0} + N_{les,1} + N_{les,2}\,, \qquad (3.5.2)$$

where

$$N_{les,0} = \frac{1}{V_t}\int\left[\alpha D_0 + \beta D_0^2\right]d\vec{r} = \alpha D_0 + \beta D_0^2\,, \qquad (3.5.3)$$

is the average number of lesions in the irradiated cell due to the prescribed dose D_0,

$$N_{les,1} = \left(\alpha + 2\beta D_0\right)\sum_{i=1}^{N_{Gy}D_0}\frac{1}{V_t}\int D_{NP}\left(\left|\vec{r}-\vec{r}_i\right|\right)d\vec{r} \qquad (3.5.4)$$

and

$$N_{les,2} = \beta\sum_{i=1}^{N_{Gy}D_0}\sum_{j=1}^{N_{Gy}D_0}\frac{1}{V_t}\int D_{NP}\left(\left|\vec{r}-\vec{r}_i\right|\right)D_{NP}\left(\left|\vec{r}-\vec{r}_j\right|\right)d\vec{r}\,. \qquad (3.5.5)$$

The sums in the second and third terms describe the total dose, and the total dose squared deposited by all ionized NPs in the cell target, respectively. Being the average number of lesions created by all ionized NPs in the cell target equal to

$$\Delta N_{les} = \left(\alpha + 2\beta D_0\right)\sum_{i=1}^{N_{ion}}\frac{1}{V_t}\int D_{NP}\left(\left|\vec{r}-\vec{r}_i\right|\right)d\vec{r} + \beta\sum_{i=1}^{N_{ion}}\sum_{j=1}^{N_{ion}}\frac{1}{V_t}\int D_{NP}\left(\left|\vec{r}-\vec{r}_i\right|\right)D_{NP}\left(\left|\vec{r}-\vec{r}_j\right|\right)d\vec{r} \qquad (3.5.6)$$

The integral

$$I_{lin}\left(\vec{r}_i\right) = \frac{1}{V_t}\int D_{NP}\left(\left|\vec{r}-\vec{r}_i\right|\right)d\vec{r} \qquad (3.5.7)$$

presents the average dose deposited by an ionized NP located in the point $\vec{r}_i$ in the cell.

Analogously, the integral

$$\frac{1}{V_t}\int D_{NP}\left(\left|\vec{r}-\vec{r}_i\right|\right)D_{NP}\left(\left|\vec{r}-\vec{r}_j\right|\right)d\vec{r} \tag{3.5.8}$$

presents the composition of the doses deposited by two ionized NPs located in the points $\vec{r}_i$ and $\vec{r}_j$ in the cell.

Taking into account that the probability of ionization per Gy is low, we can ignore the terms corresponding to the overlapping of the volumes around different ionized NPs and reduce the second integral in (3.5.6) to the average of the squared dose deposited by an ionized NP located in the point $\vec{r}_i$ in the cell as:

$$I_{sq}\left(\vec{r}_i\right)=\frac{1}{V_t}\int D_{NP}^2\left(\left|\vec{r}-\vec{r}_i\right|\right)d\vec{r}\,. \tag{3.5.9}$$

As a result, the average number of lesions formed in the cell target after delivering the prescribed dose D_0 takes the form:

$$N_{les,NP}=\alpha D_0+\beta D_0^2+\left(\alpha+2\beta D_0\right)N_{ion}D_{lin}+\beta N_{ion}D_{sq}^2\,. \tag{3.5.10}$$

where

$$D_{lin}=\frac{1}{N_{ion}}\sum_{i=1}^{N_{ion}}I_{lin}\left(\vec{r}_i\right)\quad and\quad D_{sq}^2=\frac{1}{N_{ion}}\sum_{i=1}^{N_{ion}}I_{sq}\left(\vec{r}_i\right) \tag{3.5.11}$$

are the average dose and the average of the squared dose deposited by **all** ionized NPs in the cell target per **one** ionized NP, respectively.

The sums in (3.5.11) implicitly determine the dependence of the average doses on the NP distribution and allow one, in principle, to evaluate these sums using available information related to the presence of NPs in cells. An example of MC simulations of the radiosensitization effect as a function of NP concentration, size, and clustering can be found in an article by Rudek et al., 2019.

The explicit way to take into account the heterogeneity in NP distribution inside a cell and across a cell population is to introduce the average density of **all** NPs (not only ionized), $n_{NP}\left(\vec{r}\right)$ in the subvolume $d\vec{r}$ of a cell and to present the sums in (3.5.11) as

$$\sum_{i=1}^{N_{ion}}I_{lin}\left(\vec{r}_i\right)=P_{Gy}D_0\int I_{lin}\left(\vec{r}_i\right)n_{NP}\left(\vec{r}\right)d\vec{r}\quad and\quad \sum_{i=1}^{N_{ion}}I_{sq}\left(\vec{r}_i\right)=P_{Gy}D_0\int I_{sq}\left(\vec{r}_i\right)n_{NP}\left(\vec{r}\right)d\vec{r}\,. \tag{3.5.15}$$

The integrals in (3.5.15) determine the average and average squared doses deposited by one NP (supposing that all NPs are ionized) distributed over a cell with a probability distribution $n_{NP}\left(\vec{r}\right)\Big/N_{NP}$. Multiplication of these integrals with the probability of ionization $P_{Gy}D_0$ produces the average doses deposited only by ionized NPs stochastically distributed over the cell. Therefore, the average doses deposited by **all** NPs per **one** ionized NP in the cell target (3.5.11) can be rewritten as

$$D_{lin}=\frac{1}{N_{ion}}P_{Gy}D_0\int I_{lin}\left(\vec{r}_i\right)n_{NP}\left(\vec{r}\right)d\vec{r}\quad and\quad D_{sq}^2=\frac{1}{N_{ion}}P_{Gy}D_0\int I_{sq}\left(\vec{r}_i\right)n_{NP}\left(\vec{r}\right)d\vec{r}\,. \tag{3.5.16}$$

It is important to underline that integrals (3.5.16) summarize average and average squared doses from all NPs, both ionized and nonionized, and thereafter they are multiplied with $P_{Gy}D_0$ taking into account that any NP in the cell has an equal probability of being ionized by impinging radiation.

3.6 The NP-related LQ model parameters, survival probability, and RBE.

As it follows from (3.4.2), the total number of ionized NPs depends linearly on the dose. Therefore, to obtain the explicit dependence on the prescribed dose D_0, the average number of lesions (3.3.4) should be rewritten in terms of the modified response parameters, α_{NP}, and β_{NP} for the cell culture with embedded NPs. Combine (3.3.4) and (3.5.10), we can rewrite (3.5.10) as:

$$N_{les,NP}=\alpha_{NP}D_0+\beta_{NP}D_0^2=\alpha D_0+\beta D_0^2+\left(\alpha+2\beta D_0\right)N_{ion}D_{lin}+\beta N_{ion}D_{sq}^2\,. \tag{3.6.1}$$

Introducing the coefficient

$$C_{ion}=\frac{N_{ion}}{D_0}=\frac{P_{ion}N_{NP}}{D_0}=P_{Gy}N_{NP}\,. \tag{3.6.2}$$

The total number of ionized NPs in the cell per the prescribed dose D_0, we replace N_{ion} in (3.6.1) with $C_{ion}D_0$ and present the modified response parameters as

$$\alpha_{NP}=\alpha\left(1+C_{ion}D_{lin}\right)+\beta C_{ion}D_{sq}^2,\quad \beta_{NP}=\beta\left(1+2C_{ion}D_{lin}\right). \tag{3.6.3}$$

It is important to underline that the coefficient C_{ion} does not depend on the NP distribution over the cell. On the other hand, the doses D_{lin} and D_{sq}^2 are the average doses deposited by **all** ionized NPs per **one** ionized NP, which implicitly depend on a specific distribution of NPs over and near the cell.

Substitution of the modified response parameters (3.6.3) into (3.3.4) gives the explicit expression for the survival probability of a NP loaded cell irradiated with the prescribed dose D_0:

$$S_{NP}(D_0) = \exp\left[-\alpha\left(1 + C_{ion}D_{lin} + \frac{\beta}{\alpha}C_{ion}D_{sq}^2\right)D_0 - \beta\left(1 + 2C_{ion}D_{lin}\right)D_0^2 \right]. \quad (3.6.4)$$

There are a number of quantities: Relative Biological Effectiveness (RBE), Sensitizer Enhancement Ratio (SER), Dose Modification Ratio, Radiosensitivity Enhancement Factor, and Radiation enhancement ratio that can be evaluated from the comparison of clonogenic survival data measured with and without NPs (Subiel et al., 2016). In this thesis, we will consider only the RBE that, for the combination of irradiation and NPs, is defined as the ratio D_{ref}/D_0. Here the reference dose D_{ref} is the dose of standard radiation (usually X-rays), which, after irradiation of cells without NPs, produces the same biological effects as the irradiation with the prescribed dose D_0 in the presence of NPs. Equating the survivals (3.3.1) and (3.3.4) gives:

$$\alpha D_{ref} + \beta D_{ref}^2 = \alpha_{NP}D_0 + \beta_{NP}D_0^2 . \quad (3.6.5)$$

Straightforward solution of the quadratic equation (3.6.5) with respect to D_0 gives:

$$D_0 = \frac{\sqrt{\alpha_{NP}^2 + 4D_{ref}\alpha\beta_{NP} + 4D_{ref}^2\beta\beta_{NP}} - \alpha_{NP}}{2\beta_{NP}}, \quad (3.6.6)$$

Therefore, the RBE can be calculated by using the formula:

$$RBE = \frac{D_{ref}}{D_0} = \frac{2D_{ref}\beta_{NP}}{\sqrt{\alpha_{NP}^2 + 4D_{ref}\alpha\beta_{NP} + 4D_{ref}^2\beta\beta_{NP}} - \alpha_{NP}}, \quad (3.6.7)$$

in which the NP-related LQ model parameters α_{NP} and β_{NP} are expressed by equation (3.6.3). Equation (3.6.7) allows the evaluation of the RBE for different schemes of irradiation treatment of cell cultures assisted with high Z- NPs.

CHAPTER 4

Radiosensitization effect in a spherical cell target

Among the number of parameters needed for applying the general integral equations derived in the previous chapter for evaluating the effect of NPs on the survival of a specific population of cells, the cell geometry is the first set of parameters that should be specified. In this section, we will consider the energy deposition in a spherical cell target from ionized NPs of radius R_{NP}. Additionally, we will assume that the dose distribution around the NP is spherically symmetric and described by a decreasing function $D_{NP}(r)$, where r is the distance from the NP center. These two assumptions allow one to take the triple integrals (3.3.7) and (3.3.9) and derive explicit expressions for the average dose and the average of the squared dose in the cell target.

4.1 Average doses deposited by one ionized NP

Because of simple geometry, the three-dimensional NP position $\vec{r}_i$ in the triple integrals (3.5.7) and (3.5.9) can be replaced with the distance l and both integrals can be easily reduced to iterated integrals with the integration over the spherical coordinates r, θ, and φ:

$$\begin{aligned} I_{lin}(l) &= \frac{1}{V_t}\int_{R_{\min}}^{R_{\max}} drr^2 D(r) \int_0^{\theta_{max}(r)} d\theta \sin\theta \int_0^{2\pi} d\phi \\ I_{sq}(l) &= \frac{1}{V_t}\int_{R_{\min}}^{R_{\max}} drr^2 D^2(r) \int_0^{\theta_{max}(r)} d\theta \sin\theta \int_0^{2\pi} d\phi \end{aligned}, \tag{4.1.1}$$

where R_{min}, R_{max} and θ_{max} are the limits of integration.

The integration over φ gives 2π. Taking into account that $d\theta\sin\theta = -d(\cos\theta)$ and

$$V_t = \frac{4\pi}{3}R_t^3 \tag{4.1.2}$$

we can rewrite (4.1.1) as

$$\begin{aligned} I_{lin}(l) &= \frac{3}{2R_t^3}\int_{R_{\min}}^{R_{\max}} drr^2 D(r)\left[1-\cos\theta_{max}(r)\right] \\ I_{sq}(l) &= \frac{3}{2R_t^3}\int_{R_{\min}}^{R_{\max}} drr^2 D^2(r)\left[1-\cos\theta_{max}(r)\right] \end{aligned}. \tag{4.1.3}$$

Direct fitting of MC simulations of McMahon et al. (2016) and our own MC simulations (see chapter 5) show that the additional local dose deposited by secondary electrons emitted from an ionized NP decreases rapidly with distance and can be approximated by the power law function:

$$D_{NP}(r) = D_s\left(R_{NP}\right)\left(\frac{R_{NP}}{r}\right)^{2+a}, \tag{4.1.4}$$

where $D_s\left(R_{NP}\right)$ is the dose near the NP surface, and *a* is the coefficient expressing the deviation of the RDD power law exponent from the exponent 2.

Substitution of (4.1.4) in (4.1.3) produces the integrals that express the average dose and the average of the squared dose for the RDD described by the power law function:

$$\begin{aligned} I_{lin}\left(l\right) &= \frac{3D_s\left(R_{NP}\right)R_{NP}^2}{2R_t^3}\int_{R_{\min}}^{R_{\max}} dr\left(\frac{R_{NP}}{r}\right)^{a}\left[1-\cos\theta_{max}\left(r\right)\right] \\ I_{sq}\left(l\right) &= \frac{3D_s^2\left(R_{NP}\right)R_{NP}^2}{2R_t^3}\int_{R_{\min}}^{R_{\max}} dr\left(\frac{R_{NP}}{r}\right)^{2+2a}\left[1-\cos\theta_{max}\left(r\right)\right] \end{aligned}. \tag{4.1.5}$$

The derived integrals are fairly simple and can be evaluated explicitly. However, *the* integral evaluation depends on the position of a NP with respect to the cell target and will be considered in the next two subchapters.

4.1.1 NP located outside of the cell target

In the case of $l > R_t + R_{NP}$, the NP is located outside the cell target. The sketch presenting this case is shown in Fig. 4.1. The NP is centered at the origin O of a spherical coordinate system. The polar angle θ is measured from the z-axis that passes through the cell target center O_1. The dashed line shows the sphere at distance r, near which the dose has the constant value D(r). The polar angle at which this surface crosses the structure surface determines the upper limit in the iterated integral over the angle, θ_{max}. The integrated limits in the iterated integrals over *r* are the closest, $R_{min} = l - R_t$, and the farthest, $R_{max} = l + R_t$, distances from the NP center to the closest surface of the cell and to the farthest surface of the cell target, respectively.

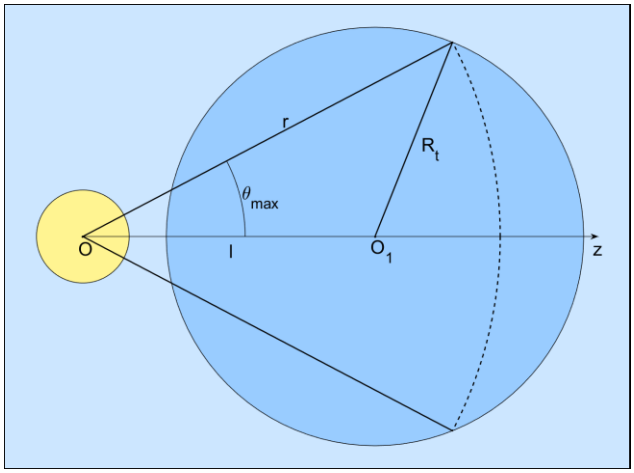

Figure 4.1. The geometry assumed for calculating the average dose and the average of the squared dose when a NP is located outside the cell target (see explanation in the text).

The angle θ_{max} is a function of the current radius r in the target sphere. The dependence of θ_{max} on r can be found with the cosine theorem:

$$\cos\theta_{\max} = \frac{r^2 + l^2 - R_t^2}{2rl}. \tag{4.1.6}$$

Substitution of (4.1.6) in (4.1.5) produces:

$$\begin{aligned} I_{lin,out}(l) &= \frac{3D_s(R_{NP})R_{NP}^2}{2R_t^3}\int_{l-R_t}^{l+R_t}\left(\frac{R_{NP}}{r}\right)^a\left(1-\frac{r^2+l^2-R_t^2}{2rl}\right)dr \\ I_{sq,out}(l) &= \frac{3D_s^2(R_{NP})R_{NP}^2}{2R_t^3}\int_{l-R_t}^{l+R_t}\left(\frac{R_{NP}}{r}\right)^{2a+2}\left(1-\frac{r^2+l^2-R_t^2}{2rl}\right)dr \end{aligned}. \tag{4.1.7}$$

Normalizing all lengths on the target radius is convenient, introducing dimensionless parameters $x = r/R_t$, $r_{NP} = R_{NP}/R_t$ and $q = l/R_t$. Then,

$$\cos\theta_{\max} = \frac{x^2 + q^2 - 1}{2xq} \tag{4.1.8}$$

and (4.1.7) can be presented as:

$$\begin{aligned} I_{lin,out}(l) &= \frac{3D_s(R_{NP})}{2}\left(\frac{R_{NP}}{R_t}\right)^{2+a}Q_{lin,out}(q) \\ I_{sq,out}(l) &= \frac{3D_s^2(R_{NP})}{2}\left(\frac{R_{NP}}{R_t}\right)^{4+2a}Q_{sq,out}(q) \end{aligned}, \tag{4.1.9}$$

where

$$Q_{lin,out}(q)=\int_{q-1}^{q+1}\left(\frac{1}{x}\right)^{a}\left(1-\frac{x^2+q^2-1}{2xq}\right)dx$$
$$Q_{sq,out}(q)=\int_{q-1}^{q+1}\left(\frac{1}{x}\right)^{2+2a}\left(1-\frac{x^2+q^2-1}{2xq}\right)dx \qquad (4.1.10)$$

are the dimensionless parameters depending on the relative position q of a NP with respect to the target.

The straightforward integration of (4.1.10) was performed with the Maple computer algebra system [Maple, URL: https://www.maplesoft.com/]. The resulting expressions describing the average dose and the average of the squared dose deposited in the cell target by one NP located at a given distance $l > R_t + R_{NP}$ ($q > 1 + r_{NP}$) from the target center are the following:

$$Q_{lin,out}(q)=\frac{(a+q-1)(q+1)^{1-a}+(a-1-q)(q-1)^{1-a}}{a(2-a)(1-a)q},$$
$$Q_{sq,out}(q)=\frac{(2a+q+1)(q+1)^{-1-2a}+(2a-q+1)(q-1)^{-1-2a}}{4a(1+2a)(1+a)q}, \qquad (4.1.11)$$

4.1.2 NP located inside of the cell target

In the case of $l < R_t - R_{NP}$, the NP is located inside the cell target. The sketch presenting this case is shown in Fig. 4.2. As in the case considered above, the simple spherical geometry provides the ability to reduce the three-dimensional integrals (3.5.7) and (3.5.9) to the iterated integrals (4.1.5), with being the only difference the integration limits.

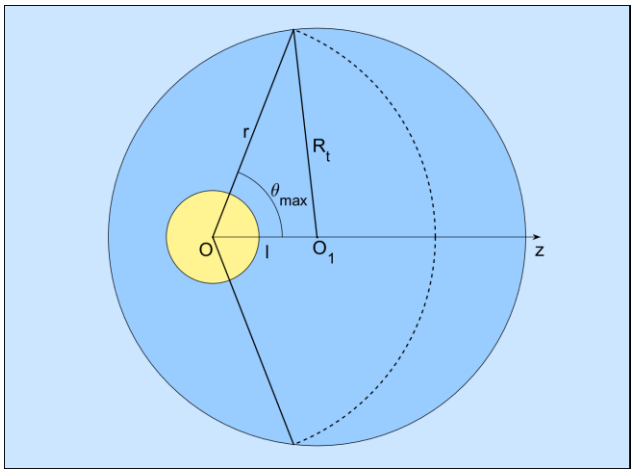

Figure 4.2. The geometry assumed for calculating the average dose and the average of the squared dose when a NP is located inside the cell target (see explanation in the text).

It is possible to see from Fig. 4.2 that the iterated integral over r should be divided into two integrals. The first one corresponds to the condition $R_{NP} < r < R_t - l$, for which the angle θ can take any value, and θ_{max} equals π. For the condition $R_t - l < r < R_t + l$, the angle θ_{max} is described by (4.1.6). As a result, the integrals (4.1.5) are presented as the sums of two iterated integrals over r:

$$\begin{aligned} I_{lin,in}(l) &= \frac{3D_s(R_{NP})R_{NP}^2}{2R_t^3}\left[2\int_{R_{NP}}^{R_t-l}\left(\frac{R_{NP}}{r}\right)^a dr + \int_{R_t-l}^{R_t+l}\left(\frac{R_{NP}}{r}\right)^a\left(1-\frac{r^2+l^2-R_t^2}{2rl}\right)dr\right] \\ I_{sq,in}(l) &= \frac{3D_s^2(R_{NP})R_{NP}^2}{2R_t^3}\left[2\int_{R_{NP}}^{R_t-l}\left(\frac{R_{NP}}{r}\right)^{2a+2} dr + \int_{R_t-l}^{R_t+l}\left(\frac{R_{NP}}{r}\right)^{2a+2}\left(1-\frac{r^2+l^2-R_t^2}{2rl}\right)dr\right] \end{aligned}. \quad (4.1.12)$$

Similarly, to the case considered in the previous subchapter, the integrals (4.1.12) can be presented as:

$$\begin{aligned} I_{lin,in}(l) &= \frac{3D_s(R_{NP})}{2}\left(\frac{R_{NP}}{R_t}\right)^{2+a} Q_{lin,in}(q) \\ I_{sq,in}(l) &= \frac{3D_s^2(R_{NP})}{2}\left(\frac{R_{NP}}{R_t}\right)^{4+2a} Q_{sq,in}(q) \end{aligned}, \quad (4.1.13)$$

where

$$\begin{aligned} Q_{lin,in}(q) &= 2\int_{r_{NP}}^{1-q}\left(\frac{1}{x}\right)^a dx + \int_{1-q}^{1+q}\left(\frac{1}{x}\right)^a\left(1-\frac{x^2+q^2-1}{2xq}\right)dx \\ Q_{sq,in}(q) &= 2\int_{r_{NP}}^{1-q}\left(\frac{1}{x}\right)^{2a+2} dx + \int_{1-q}^{1+q}\left(\frac{1}{x}\right)^{2a+2}\left(1-\frac{x^2+q^2-1}{2xq}\right)dr \end{aligned}. \quad (4.1.14)$$

The straightforward integration performed with the Maple computer algebra system gives the resulting expressions describing the average dose and the average of the squared dose deposited in the cell target by one NP located at a given distance $l < R_t - R_{NP}$ ($q < 1 - r_{NP}$) from the target center:

$$\begin{aligned} Q_{lin,in}(q) &= \frac{(a+q-1)(1+q)^{1-a} - (a-1-q)(1-q)^{1-a}}{a(2-a)(1-a)q} - \frac{2r_{NP}^{1-a}}{1-a} \\ Q_{sq,in}(q) &= \frac{(2a+q+1)(1+q)^{-2a-1} - (2a-q+1)(1-q)^{-2a-1}}{4a(1+2a)(1+a)q} + \frac{2r_{NP}^{-2a-1}}{2a+1} \end{aligned}, \quad (4.1.15)$$

4.2 Average doses deposited by an ensemble of NPs

Equations (4.1.9) and (4.1.13) describe the average doses deposited in a spherical cell target by one ionized NP located outside and inside the target at a given distance l from the target center. Assuming the spherical symmetry of the NP distribution around the target center, the introduced in subchapter 3.3 distribution probability $n_{NP}\left(\vec{r}\right)\Big/N_{NP}$ can be replaced with the spherically symmetric distribution $n_{NP}\left(l\right)\Big/N_{NP}$ describing the probability of finding a NP (ionized or not) at a given distance l from the target center. That allows us to integrate the average doses (4.1.9) and (4.1.13) over the target and present the average doses deposited by **all** NPs per **one** ionized NP in the cell target by the integrals:

$$\begin{aligned} D_{lin} &= \frac{3}{2} D_s\left(R_{NP}\right)\left(\frac{R_{NP}}{R_t}\right)^{2+a} \int 4\pi Q_{lin}\left(\frac{l}{R_t}\right)\frac{n_{NP}\left(l\right)}{N_{NP}} l^2 dl \\ D_{sq}^2 &= \frac{3}{2} D_s^2\left(R_{NP}\right)\left(\frac{R_{NP}}{R_t}\right)^{4+2a} \int 4\pi Q_{sq}\left(\frac{l}{R_t}\right)\frac{n_{NP}\left(l\right)}{N_{NP}} l^2 dl \end{aligned} . \qquad (4.2.1)$$

Here $Q_{lin}(q)$ and $Q_{sq}(q)$ are the dimensionless parameters depending on the relative position of a NP with respect to the target center, $q = l/R_t$ describing by (4.1.11) and (4.1.13) for $q > 1 + r_{NP}$ and $q < 1 - r_{NP}$, respectively.

The integral expressions (4.2.1) allow one to calculate the average and average squared doses deposited by an ensemble of NPs (ionized or not) per one ionized NP with the average NP density $n_{NP}(l)$ at a given distance l distributed over a cell. For a spherically symmetrical distribution of NPs, the simplest case is a thin spherical shell at a given distance l loaded with N NPs. The average density for this case is presented by the delta function, and (4.2.1) is reduced to (4.1.9) or (4.1.13).

Another simple case is the uniform random distribution of N_t NPs in the cell target volume. This case describes the NP distribution in the nucleus and was used in MC simulations of NP-induced radiosensitization and cell survival (Ferrero et al., 2017; Lin et al., 2015; Xie et al., 2015). The average concentration of NPs in an inner shell between l and l + dl is proportional to the shell volume divided by the target volume:

$$n\left(l\right)dl = N_t \frac{4\pi l^2 dl}{V_t} = N_t \frac{4\pi l^2 dl}{4\pi R_t^3/3} = N_t \frac{3l^2}{R_t^3} dl \, . \qquad (4.2.2)$$

The last case we will consider here is the uniform random distribution of N_{sh} NPs in an outer shell concentric with the target. This case describes the NP distribution in the cell cytoplasm and was used by (Lin et al., 2015; Xie et al., 2015; Yang et al., 2018; Rieck et al., 2019).Similar to (4.2.2), the average concentration of NPs in a shell between l and l + dl is proportional to the shell volume divided by the whole outer shell volume:

$$n(l)\,dl = N_{sh}\,\frac{3l^2}{R_{sh,out}^3 - R_{sh,in}^3}\,dl\,, \tag{4.2.3}$$

where $R_{sh,in}$ and $R_{sh,out}$ are the inner and outer radii of the considered shell.

The obtained expression in this chapter are used in the following chapters to evaluate the biological outcomes of irradiation treatments assisted with GNPs in the case of these particular distributions of NPs.

CHAPTER 5

MC simulations of RDD around irradiated gold NP

The analytical expressions presented in chapter 4 describe the energy deposition in a spherical cell target from a number of ionized NPs distributed in a cell and the additional average number of lesions formed in the cell target due to these NPs. In this section, we will simulate RDDs around GNPs of different radii per one ionization using the MC technique and fit the simulated RDDs to the power law function (4.1.4).

5.1 MC simulations

Monte Carlo (MC) simulations were performed using TOPAS (version 3.5, Perl et al., 2012), which is based on Geant 4, a toolkit for the simulation of the passage of particles through matter [https://geant4.web.cern.ch]. In addition, the Livermore physics model (G4EmLivermorePhysics) was also selected for the simulations in the NP and the water phantom. The Livermore library implements a low-energy model that allows the simulation of electrons and photons from 250 eV to 1 GeV and is based on publicly available evaluated data tables from the Livermore data library (EADL, EEDL, EPDL) (Perkins and Cullen, 1994). The model includes elements with atomic number Z from 1 to 100, allowing the simulation of the atomic relaxation process (fluorescence and Auger) for elements with an atomic number $Z > 5$ (EADL transition data). In our simulations, the production cut was 200 eV, and the same energy was used for the tracking cut. The step size is automatically selected by TOPAS using logic from Geant4 that takes into consideration the local geometry and physics (Perl et al., 2012).

The simulation of RDD around a single spherical GNP of a given diameter suspended in water was split into two simulation steps. In the first step, the NP is irradiated with a parallel circular beam of matching NP size, with a total of $N_{ph} = 8 \times 10^8$ primary photons. The Auger, AugerCascade, and Fluorescence modes were enabled to simulate atomic relaxation processes, and the production threshold of Auger and fluorescence electrons was disabled without setting a lower limit. The electrons produced within the GNP that reached its surface were scored as phase space, identifying the process that led to their ejection from gold atoms and including information on their initial kinetic energy, position, and momentum.

The obtained spectrum of electrons emitted from the NP was used as the source of irradiation in the second step of the simulation. For this, the source of electrons was placed at the center of a spherical water phantom, and the escaped electrons were propagated through the phantom. Deposited doses were scored in 15 concentric 1 nm shells uniformly distributed on a logarithmic scale from 1 nm to 3 μm and normalized on the number of ionizations. The calculated statistical uncertainty in the dose deposited in the shell was, in all cases, less than 1.5%.

The number of ionizations in a GNP irradiated with mono- and polyenergetic photon beams $N_{ion,NP}$ was calculated as a sum of ejected photoelectrons and Compton electrons. Because the radius of the photon beam was matched to the GNP radius, the photon fluence was calculated using the formula $\Phi = N_{ph} \big/ \pi R_{NP}^2$. The prescribed dose D_0 corresponding to the calculated fluence was found using equation (3.2.8). As a result, the probability of ionizations in a single NP per prescribed dose D_0 was calculated as $P_{Gy} = N_{ion,NP}/D_0$.

5.2 Probability of ionization of a single gold NP per Gy

Fig. 5.1 presents the dependences of the probability of ionizations in single NPs of 2, 10, 20, 50,a nd 100 nm diameters on the incident photon energy. The probabilities are normalized to the absorbed dose deposited in pure water (without NPs), which is usually named the prescribed dose. The solid curves are calculated with Eq. (3.2.10), while the points present the MC simulation data found in the literature (crosses and rectangles) and obtain in this thesis (circles). Because the probabilities are proportional to the NP mass, all the curves have the same shape, which is similar to the well-known ratio of the coefficients widely presented in the literature devoted to the radiation dose enhancement of GNPs (see, for instance, McMahon et al., 2016).

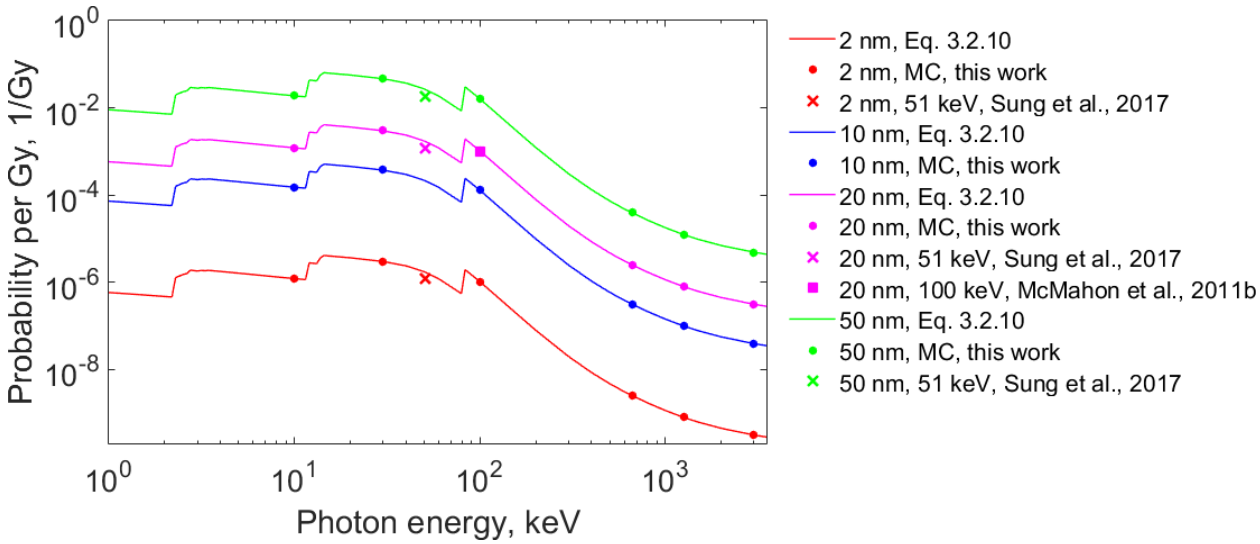

Figure 5.1. Probability of ionization per irradiation dose in single NPs of indicated diameters as a function of the photon energy. The lines present the data calculated with Eq. (3.2.10). The MC simulation performed in this work and data found in the literature (McMahon et al., 2011a; Sung et al., 2017).

The probability of ionization in NPs irradiated with polyenergetic x-ray spectra is shown in Fig. 5.2. The left panel presents the 150 and 250 kVp photon energy spectra. The spectra consist of a broad bremsstrahlung continuum and two sharp lines at about 59 and 67 keV corresponding to the K_α and K_β characteristic lines of tungsten. The right panel presents the probability of ionization per irradiation dose as a function of the NP radius. The straight lines are calculated with Eq. (3.2.9) and reflect the cubic dependences of the probability on the NP radius. The markers show the results of MC simulations carried out in this work as described in subchapter 5.1 (circles) by Lin et al., 2015 (crosses) and Sung et al., 2017 (triangles).

As can be seen from Figs. 5.1 and 5.2, the probabilities of ionization calculated analytically for monoenergetic photons and polyenergetic x-ray spectra are in good agreement with those found by MC simulations obtained in this work and presented in the literature that confirms the performance of the simple Eqs. (3.2.9) and (3.2.10).

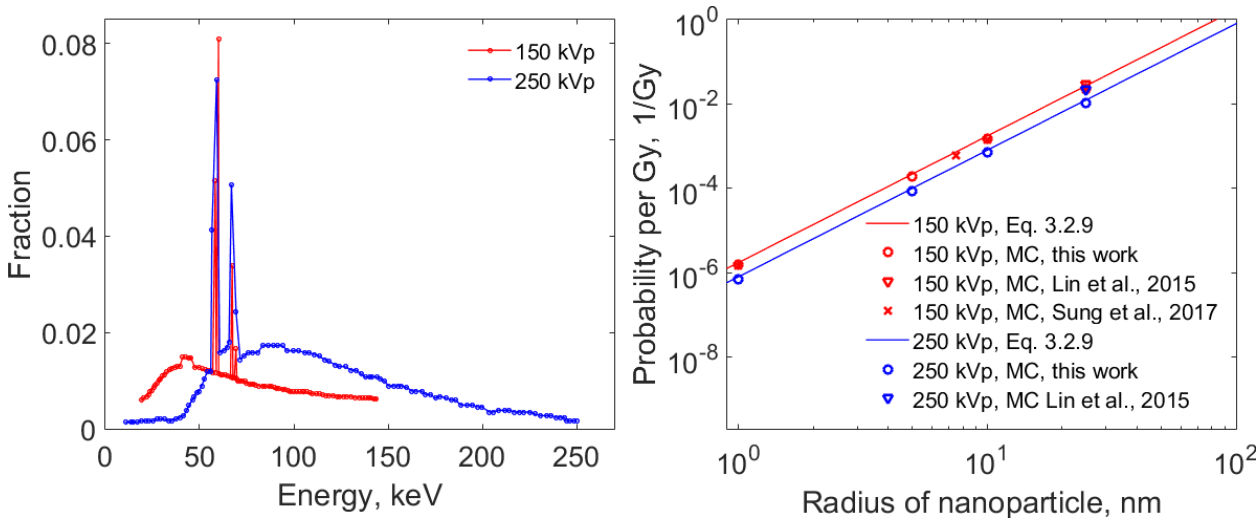

Figure 5.2. Probability of ionization in single NPs irradiated with polyenergetic x-ray spectra. Left. 150 and 250 kVp photon energy spectra were taken from Xie et al., 2015 and Poludniowski et al., 2009 in terms of relative frequency per photon energy for the 150 and 250 kVp spectra, respectively. Right. The probability of ionization per irradiation dose as a function of the NP radius. The lines present the data calculated with Eq. (3.2.9). The points are the MC simulation performed in this work and the data found in the literature.

5.3 RDD around a 20 nm GNP irradiated with 100 keV photons

First, a GNP of 20 nm diameter irradiated with 100 keV photons was considered aiming to compare the simulated RDD with the energy deposition data presented in the supplementary information by McMahon et al., 2016. Our simulation results and the data of McMahon et al., 2016 are shown in Fig. 5.3. Both RDDs are practically the same and monotonically decrease as the distance from the NP increases. As it follows from the energy deposition data presented in the supplementary information by McMahon et al., 2016, Auger electrons account for the most significant contribution to the dose deposition. The contribution of the photoelectrons becomes noticeable at distances more than 150 nm, while the contribution of Compton electrons is negligible.

Despite the weak ‘waviness’ of the RDD caused by the different penetration of the emitted Auger and photoelectrons of different energies; the RDD, on the whole, is close to a straight line in the double logarithmic scale and, therefore, could be approximated by the power law function (4.1.4). The result of such approximation with the parameters D_s = 3000 Gy and a = 0.4 is drawn with a bold black line. It can be seen that the power law reasonably fits the simulated RDD at

distances less than 100 nm and more than 600 nm. The maximal deviation from the simulated RDD (about two times higher) is observed at 200 nm.

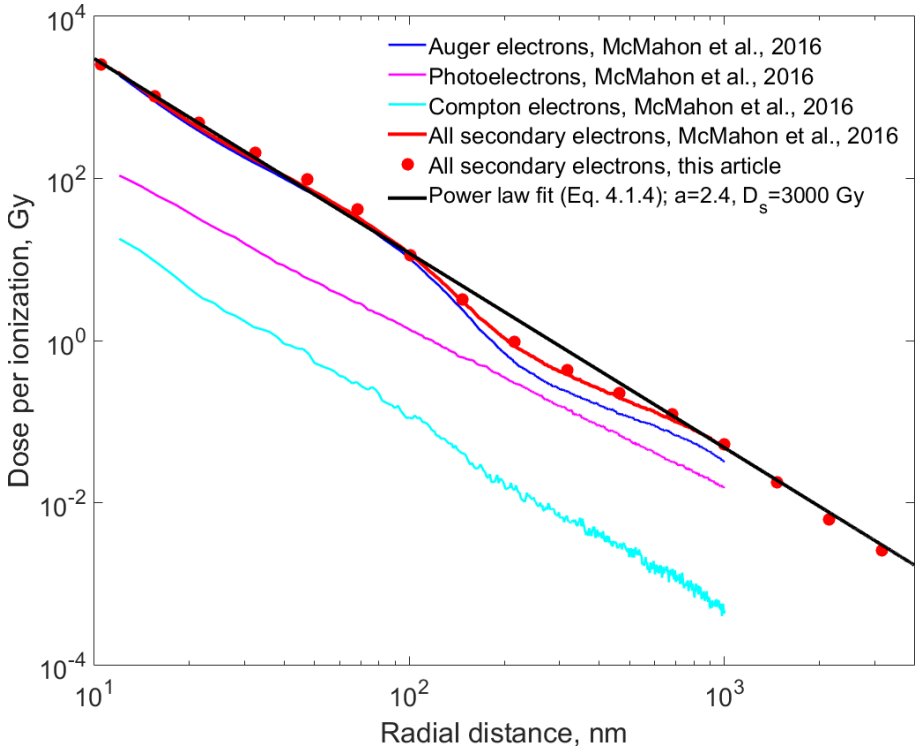

Figure 5.3. Radial dose distribution per one ionization around GNPs of 20 nm diameter. The bold red line and red points present the MC simulated RDDs performed by McMahon et al., 2016 and by us, respectively. The thin lines show the contribution of indicated groups of emitted electrons simulated in (McMahon et al., 2016). The bold straight line is the power law fit with the indicated parameters.

5.3 RDD around ionized NPs of various radii irradiated with keV and MeV photons

Radial dose distributions around ionized GNPs of 1, 5, 10, 25, and 50 nm radii are shown in Fig. 5.4. Each panel in the figure presents the RDDs simulated for monoenergetic photon beams of six selected energies: namely 10, 30, 100, 661 (^{137}Cs) 1252 (^{60}Co) and 3000 keV. The RDDs for given photon energy do not depend practically on the GNP radius and can be fitted well by the power law function (4.1.4) from the NP surface to 3000 nm. The only exception is the RDD for 10 keV photons, which can be fitted up to 1500 nm and then decreases sharply due to the limited range of secondary electrons emitted from the GNPs. The RDDs for 1 nm GNPs irradiated with 1252 (^{60}Co) and 3000 keV are lower than those for the GNPs of greater radii. The reason for such

discrepancy is unclear and could be explained by low ionization probability that results in insufficient precision of the MC simulations.

The parameters of the power law function, the dose near the NP surface D_s (at 1 nm), and the exponent 2+a are presented in Table 5.1. The fitting results show that the simulated RDDs are not only the same for GNPs of different radii, but they are also similar for photon energies ranging from 10 to 3000 keV. The exponent equals 2.4 for photon energies of 10, 30, and 100 keV and a little greater (2.6) for higher energies. The parameter D_s varies from the maximal value of 8.5×10^5 Gy for 30 and 100 keV photons and decreases to 2.0×10^5 for 3000 keV photons. It should be noted that the parameter D_s presented in Table 5.1, and Eq. 4.1.4 can be used only for calculating RDDs around GNPs with a radius of 1 nm. To use this parameter for GNPs with greater radii, Eq. 4.1.4 should be rewritten as:

$$D_{NP}(r) = D_s\,(1\,nm)\left(\frac{1\,nm}{r,nm}\right)^{2+a}, \qquad (5.3.1)$$

where r is the radial distance from the GNP center expressed in nm.

Table 5.1. The parameters of the power law function (Eq. 4.1.4) for MC simulated RDDs around ionized GNPs irradiated by monoenergetic photons.

Photon energy, keV	10	30	100	661 (^{137}Cs)	1252 (^{60}Co)	3000
2 + a	2.4	2.4	2.4	2.6	2.6	2.6
D_s(1 nm), Gy	6.5×10^5	8.5×10^5	8.5×10^5	5.0×10^5	5.0×10^5	2.0×10^5

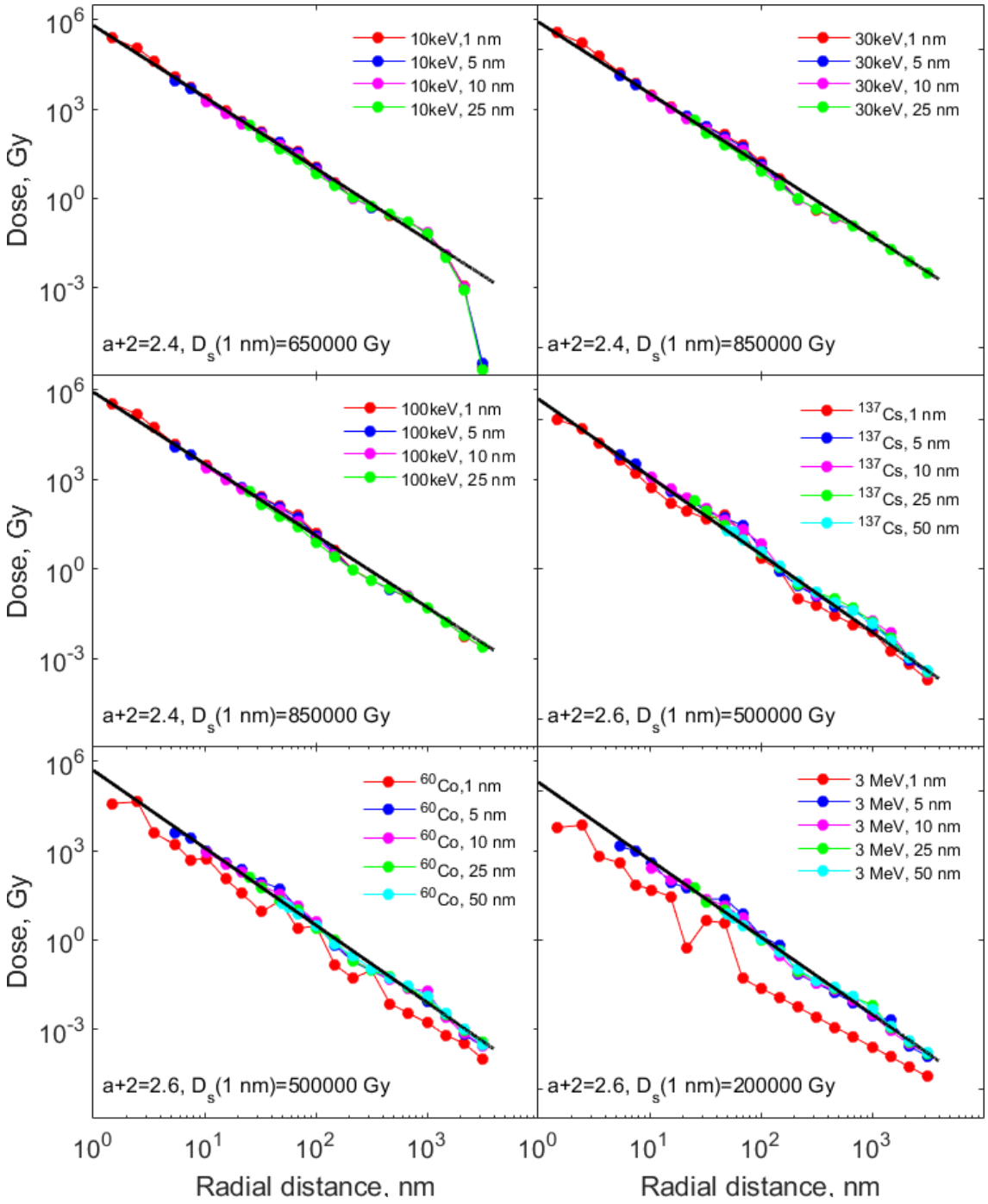

Figure 5.4. Radial dose distributions around ionized GNPs irradiated by monoenergetic photons as a function of the radial distance from the GNP center. The points present the MC simulated RDDs for GNP radii of 1,5,10, 24, and 50 nm. The bold straight lines show the power law fit (Eq. 4.1.4) with the indicated parameters.

Radial dose distributions around ionized GNPs of 2, 10, 20, and 50 nm diameters irradiated by polyenergetic X-ray beams are shown in Fig. 5.5. The left and right panels of the figure present

the RDDs simulated for the 150 and 250 kVp X-ray spectra, respectively. The RDDs are very similar to those simulated for monoenergetic photons of 10, 30, and 100 keV and can be fitted well by the power law function (4.1.4) from the NP surface to 3000 nm. The exponent equals 2.4 for both X-ray spectra, while the parameter D_s equals 2.0×10^6 and 1.0×10^6 for the 150 and 250 kVp X-ray spectra, respectively.

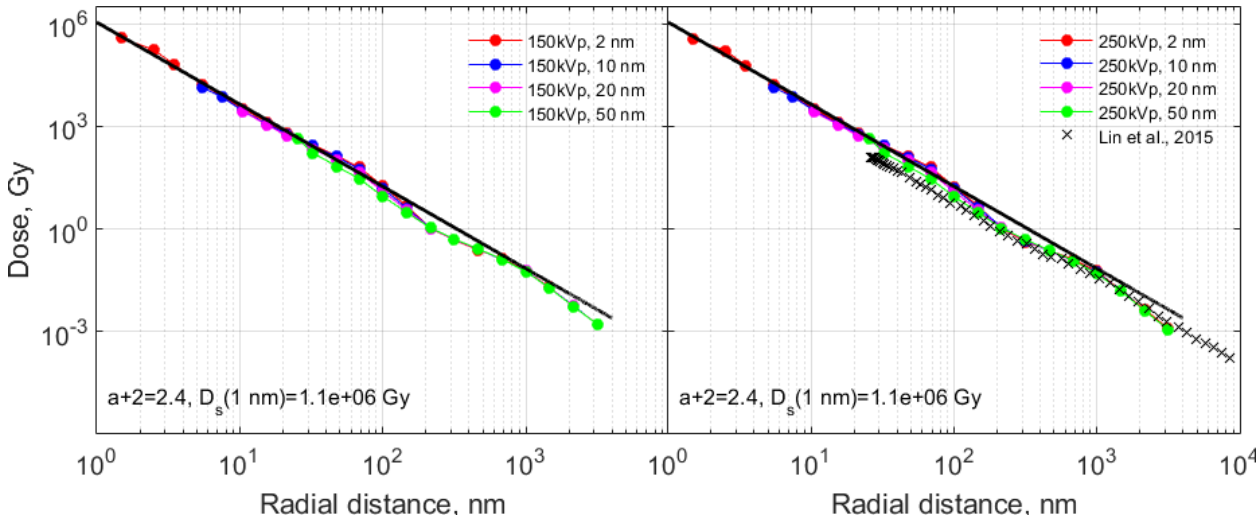

Figure 5.5. Radial dose distributions around ionized GNPs irradiated by 150 (left) and 250 kVp (right) x-ray beams as a function of the radial distance from the GNP center. The points present the MC simulated RDDs for GNP diameters of 2, 10, 20, and 50 nm. The crosses are the RDDs for 50 nm diameter GNP MC simulated by Lin et al., 2015. The bold straight lines show the power law fit (equation 2.21) with the indicated parameters.

CHAPTER 6

Radiosensitization effect in a spherical MDA-MB-231 cell with embedded GNPs

In this chapter, we will apply these expressions to predict the radiosensitization effect in spherical cells with embedded GNPs irradiated with X-rays. A human breast cancer cell MDA-MB-231, for which an extended set of α and β LQ parameters for various combinations of GNPs and irradiation modalities can be found in literature, was selected. A simple spherical cell model was used. The cell was modeled as a water sphere of radius R_{cell} = 6750 nm (Coulter et al., 2012) with a cell nucleus of radius R_t = 3500 nm (Fu et al., 2012) concentric to the cell. The shell between R_t and R_{cell} models the cell cytoplasm. Additionally, a water shell with inner and outer radii of R_{cell} and $R_{out} = R_{cell}$ + 2500 nm was added outside the cell to represent the extracellular media region. The explicit analytical expressions derived in chapter 4 and fitted in chapter 5 by the power law RDDs around GNPs were used to calculate the average doses and average of the squared doses deposited in the cell nucleus by ionized NPs. The additional average number of lesions formed in the cell target due to these NPs, NP-related LQ model parameters, survival curves, and RBEs of the cancer cell MDA-MB-231 were calculated using the analytical expressions derived in chapter 3.

There are a number of the LQ parameters for tumors published in clinical radiotherapy studies (see, for instance, a review by van Leeuwen et al., 2018). In this work, we will use the parameters α = 0.019 1/Gy and β = 0.052 $1/Gy^2$ for MDA-MB-231 breast cancer cells irradiated with 160 kVp photons (Jain et al., 2011). These parameters were also used by (McMahon et al., 2011; Lin et al., 2015; Sung et al., 2017; Sung and Schuemann, 2018; Rieck et al., 2019; Bannister et al., 2020) for MC simulations of the radiobiological response of NPs combined with radiotherapy.

6.1 Average doses and doses squared deposited in the cell target by ionized NP.

The explicit analytical expressions (4.1.9) and (4.1.13) describe the average doses, $I_{lin}(l)$, and the average of the squared doses, $I_{sq}(l)$, deposited one ionized NP located outside and inside the target (cell nucleus) at a given distance l from the target center, respectively. The expressions are directly proportional to the dimensionless parameters $Q_{lin}(q)$ and $Q_{sq}(q)$, which depend on the relative position of a NP with respect to the target center, $q = l/R_t$ and described by Eq. 4.1.11 and

4.1.15 for $q > 1 + r_{NP}$ and $q > 1 + r_{NP}$, respectively. The proportional factors contain only four parameters: the target (nucleus) radius and the other three related to the power law approximation of the NP RDDs, which are the NP radius R_{NP}, the dose per one ionization at the NP surface, D_s, and the exponent a.

The average dose and the average of the squared dose deposited in the cell nucleus by one ionized GNP of 20 nm diameter located in and outside the nucleus are shown in figure 6.1 by solid lines. As was expected, maximal averages of the doses are deposited by a NP located in the nucleus center and gradually decrease as the distance to the nucleus center increases. The average of the squared dose from the NP located in the nucleus is practically independent of the location of NP because for small $q = l/R_t$, the second term in Eq. 4.1.15 (that is independent of q) is much larger than the first one.

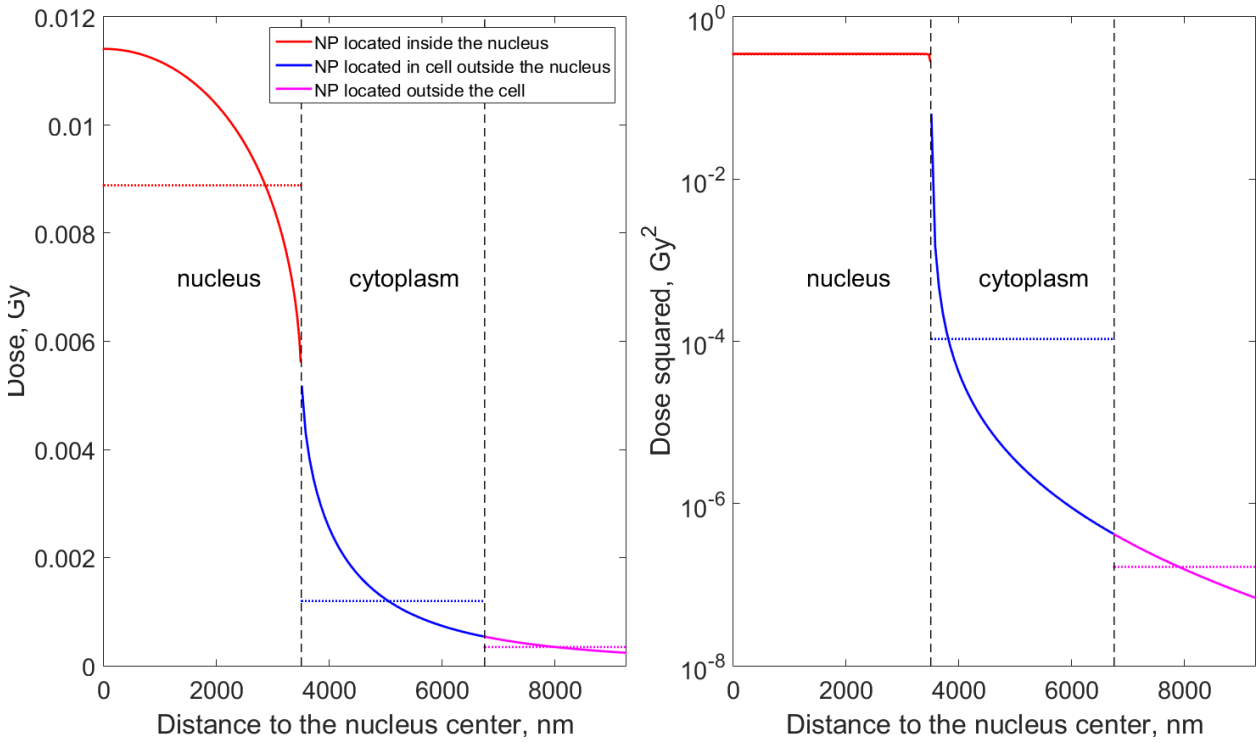

Figure 6.1. The average dose (left) and the average of the squared dose (right, semi-logarithmic scaled) deposited by one ionized NP in the cell target. The solid lines present the dependences of the doses on the distance between the position of the NP in the cell and the target center. The dotted lines mark the doses deposited by one randomly placed NP in the target (red dotted line), in the cytoplasm (blue lines), and the extracellular media region (magenta lines).

The integral expressions (4.2.1) allow one to calculate the average and average squared doses deposited by an ensemble of NPs (ionized or not) per one ionized NP with the average NP

density $n_{NP}(l)$ at a given distance l distributed over a cell. The dotted lines in Fig. 6.1 mark the average doses deposited in the cell target by one randomly placed NP in the two cell regions, the nucleus, and cytoplasm, and in one extracellular media region. These averages were calculated by integrating the doses drawn in figure 6.1 with the corresponding solid lines using Eqs. 4.2.2 and 4.2.3, respectively, and as a result of such integration, were found to be equal to intermediate values of doses deposited by NPs located at given positions.

Here we want to recall again that the calculated average doses and the averaged squared doses are not actual doses deposited by ionized NPs. Instead, as was underlined by Elsässer and Scholz, 2010, there are expected values for the dose deposition on the nanometer scale rather than an actual dose distribution.

6.2 Average number of lesions due to the NP presence

As was derived in chapter 3, the average number of lesions created in the cell target by one ionized NP described by Eq. 3.5.10 consists of three terms: the average number of lesions in the irradiated cell due to the direct action of the prescribed dose D_0 on the cell target and two terms due to the creation of lesions by the additional dose from ionized NPs. The additional number of lesions per total number of NPs in the cell can be presented as:

$$\frac{\Delta N_{les,NP}}{N_{NP}} = \left(\alpha + 2\beta D_0\right) P_{Gy} D_0 D_{lin} + \beta P_{Gy} D_0 D_{sq}^2, \tag{6.2.1}$$

where in accordance with (3.4.2) and (3.6.2)

$$P_{Gy} D_0 = P_{ion} = \frac{N_{ion}}{N_{NP}}, \tag{6.2.2}$$

is the probability of ionization in a single NP irradiated with the prescribed dose D_0.

As it follows from (6.2.1), the additional number of lesions is the linear combination of the average dose D_{lin} and the average of the squared dose D_{sq}^2 delivered by **all** NP per **one** ionized NP. The coefficients of proportionality of the dose and squared dose terms are equal to $\left(\alpha + 2\beta D_0\right) P_{Gy} D_0$ and $\beta P_{Gy} D_0$; therefore, only the LQ model parameters α and β and the ionization rate, P_{Gy} are needed for the calculation of the additional average number of lesions for a given dose D_0. For a specific case of 20 nm in diameter GNP irradiated with 100 keV photons, the ionization rate was found to be equal to 9.6×10^{-4} 1/Gy (McMahon et al., 2011a) and 1.0×10^{-3} (Melo-Bernal et al., 2018), respectively.

Fig. 6.2 presents the average number of additional lesions normalized on the total number of NP located at a given distance l from the nucleus center. Average doses were calculated using Eqs. 4.1.9 and 4.1.13 for l values outside and inside the nucleus, respectively. The left panel in Fig. 6.2 shows the first and second terms in (6.2.1) and their sum for a dose of 10 Gy as a function of the distance from the location of a NP to the target center. When a NP is located inside the nucleus, both terms contribute to creating additional lesions. However, for NPs located outside the target, the contribution of the second (squared) term is negligible compared to the first (linear) term. The right panel in Fig. 6.2 presents the additional average number of lesions for several doses. Two trends can be noted. The first one is the monotonous increase of the lesion numbers with the dose, mainly due to the increase in the number of ionized NP. The second trend is the sharp decrease of the lesion numbers as the distance increases between the NPs and the target due to $1/r^{2.4}$ and $1/r^{4.8}$ radial dependences of the linear and squared RDDs around ionized NP.

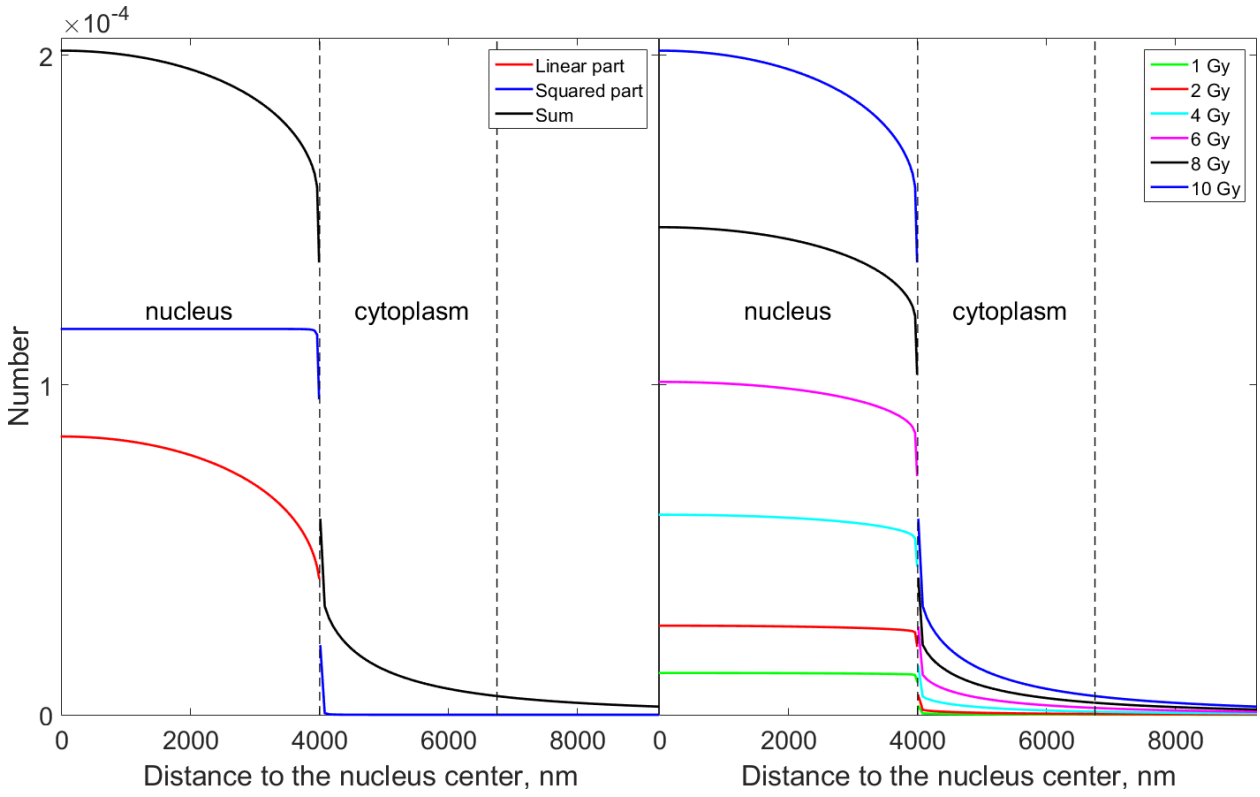

Figure 6.2. The additional average number of lesions created in the cell target per total number of NPs in a shell located at a given distance as a function of the distance between the position of the NPs and the target center. Left: The figure shows the additional numbers for a prescribed dose of 10 Gy corresponding to linear and squared terms in Eq. 6.2.1. Right: The additional numbers of lesions for indicated values of the prescribed dose.

6.3 NP-related LQ model parameters, survival curves, and RBE

The explicit expression (3.6.4) for the survival probability of a NP loaded cell irradiated with the prescribed dose D_0 contains only five parameters: the LQ model parameters α and β fitting a cell survival curve in the absence of NPs, the total number of ionized NPs in the cell per the prescribed dose C_{ion}, and the average dose D_{lin} and the average of the squared dose D_{sq}^2 deposited in the cell target by **all** NPs per **one** ionized NP. The coefficient C_{ion} does not depend on the NP distribution over the cell, while the average doses implicitly depend on a specific distribution of NPs over and near the cell. The number of ionized NPs in an irradiated cell is proportional to the dose. The proportionality coefficient, ionization rate, is the important parameter that strongly influences the dose deposition to the cell target. The last two parameters, the average dose and the average of the squared dose deposited in the cell target by one ionized NP, are of vital importance for the proposed approach. Unfortunately, no *in vitro* works known to us devoted to studies of GNP radiosensitization effects contain complete information describing the NP distribution in cell structures. This does not allow us to calculate the experimental measured survival NP-related LQ model parameters and survival curves. Therefore, the simplified spherically symmetrical distributions of NPs considered in subchapter 4.2 were used.

Fig. 6.3 presents the NP-related LQ model parameters and corresponding cell survival curves for irradiated with 100 keV photons cells with randomly distributed 20 nm GNPs. The left panel presents the case when the NPs are randomly distributed in the target. In contrast the middle and right panels present the cases corresponding to the randomly distributed NP in the cytoplasm and extracellular media, respectively. The mass fractions of gold in the cell (water) were selected to equal 1, 3, and 10 mg g^{-1}. The total numbers of NP in the cell regions, as well as the corresponding NP concentration, are presented in Table 1.

Table 1. 20 nm diameter GNPs concentrations and numbers in three concentric spherical cell regions. The NP concentration is expressed as a mass fraction of the NP element in water C_m, a NP molarity C_M, and a NP number concentration C_N. The relationships between NP concentrations are derived in subchapter 3.1.

Cell region	V, cm^3	C_w, mg/g	Molarity, M	C_N, cm^{-3}	NP number
Nucleus, 3500 nm*	1.80×10^{-10}	1	2.05×10^{-8}	1.24×10^{13}	2.22×10^{3}
		3	6.16×10^{-8}	3.71×10^{13}	6.66×10^{3}
		10	2.05×10^{-7}	1.24×10^{14}	2.22×10^{4}
Cytoplasm, 6750 nm*	1.11×10^{-9}	1	2.05×10^{-8}	1.24×10^{13}	1.37×10^{4}
		3	6.16×10^{-8}	3.71×10^{13}	4.11×10^{4}
		10	2.05×10^{-7}	1.24×10^{14}	1.37×10^{5}
Extracellular media, 9250 nm*	2.02×10^{-9}	1	2.05×10^{-8}	1.24×10^{13}	2.51×10^{4}
		3	6.16×10^{-8}	3.71×10^{13}	7.52×10^{4}
		10	2.05×10^{-7}	1.24×10^{14}	2.51×10^{5}
Perinuclear region 3550 nm*	7.81×10^{-12}	100	2.05×10^{-6}	1.24×10^{15}	9.66×103
		200	4.11×10^{-6}	2.47×10^{15}	1.93×104
		300	6.16×10^{-6}	3.71×10^{15}	2.90×104

*outer radius

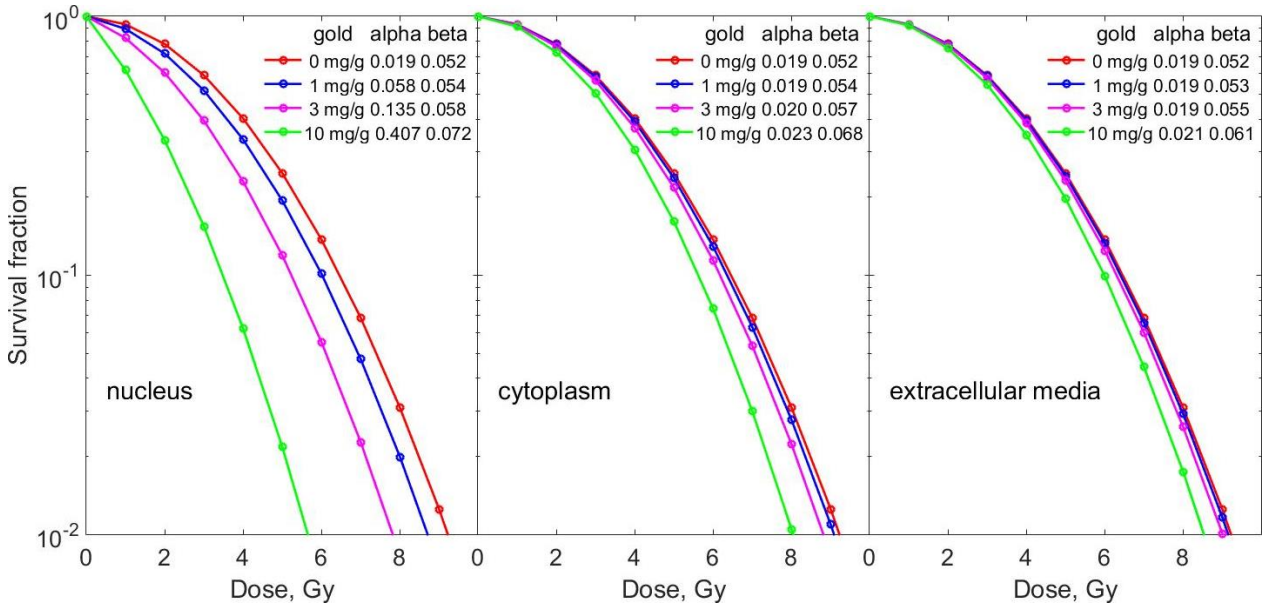

Figure 6.3. Survival curves for cells irradiated with 100 keV photons and 20 nm GNPs randomly distributed in the nucleus (left) and cytoplasm (middle) and extracellular media (right). The legends show the values of the NP-related LQ model parameters, αNP, and βNP, calculated for indicated mass fractions of gold in the corresponding regions.

As was expected, the calculated NP-related LQ model parameters systematically increase, and the survival curves show a significant reduction in the survival fraction of cells with increasing NP concentration. For a given mass fraction of gold, both effects are most pronounced for NPs

distributed in the target. Both effects are most pronounced for NPs distributed in the target for a given mass fraction of gold. The effect of NPs distributed in the cytoplasm and extracellular region on the LQ parameters and cell survival becomes noticeable when the mass fractions of gold exceed 3 and 10 mg g^{-1}, respectively.

The survival curves presented in Fig. 6.3 demonstrate that NPs located inside the target could have a noticeable cell-killing effect. It is widely accepted now that NPs are able to cross the cell membrane and penetrate the cellular cytosol; however, they do not pervade the cell nucleus (Falk et al., 2020). Therefore, it is evident that among NPs distributed over the cytosol, the most efficient will be the NPs located near the nucleus. To consider such a case, survival curves for cells loaded with 20 nm GNPs randomly distributed in a perinuclear region of 50 nm width and irradiated with 100 keV photons were calculated. Fig. 6.4 presents the survival curves calculated for total numbers of GNPs equal to 9.7×10^3, 1.9×10^4 and 2.9×10^4 that correspond to the weight fractions of gold in the perinuclear region being of 100, 200, and 300 mg g^{-1}, respectively. The behavior of calculated survival curves and values of the reduction in survival fraction are similar to those of cell survivals presented in the *in-vitro* literature data. However, a quantitative comparison of the analytical results is presented in Figs. 6.3 and 6.4 is not feasible because most of these studies present very limited information on the NP distribution in cells.

The inset in Fig. 6.4 shows the dependence of RBE on the weight fraction of gold in the perinuclear region calculated with Eq. 3.6.7 using the values of the NP-related LQ model parameters, α_{NP} and β_{NP} presented in the main Fig. 6.4. Zygmanski et al., 2013a have summarized experimental parameters of LQ model for different cell lines in the presence and absence of GNPs and the corresponding experimental RBE values. All the presented RBE values for cells irradiated with X-rays are higher than 1.3. To reach such RBE values, the total amount of gold in the perinuclear region must exceed 5×10^4 GNPs of 20 nm diameter or 520 mg g^{-1}. The cytoplasm and the perinuclear region volume ratio is 142 for our cell model (see Table 1).This means that the effective weight fraction of gold in the cytoplasm (assuming the homogenous distribution of GNPs) should be higher than 520/142 = 3.7 mg g^{-1} or 74 nM. Toxicological studies of GNPs show that gold atom concentrations ranging from nM to μM are most common when studying toxicity (Alkilany and Murphy, 2010). Therefore, the concentration of GNPs in the perinuclear region of the cell at the level of 100 nM and higher is reasonably achievable. The case considered above could be applied to the modeling of survival curves and related quantities (RBE, SER, Dose

Modification Ratio, Radiosensitivity Enhancement Factor, among others) evaluated during the performance of *in vitro* studies of radiosensitization effects.

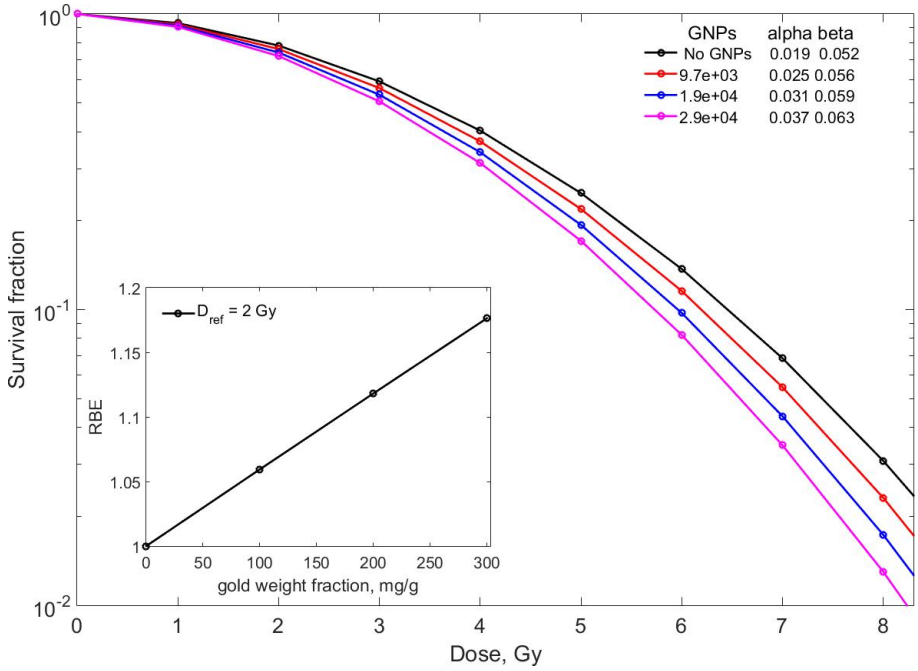

Figure 6.4. Survival curves for 100 keV photon irradiated cells loaded with 20 nm GNPs randomly distributed in a perinuclear region of 50 nm width. The legend shows the values of the NP-related LQ model parameters, αNP and βNP calculated for indicated total numbers of GNPs in the perinuclear region. The inset shows the RBE dependence on the gold weight fraction calculated with Eq. 3.6.7. The points in the inset correspond to the numbers of GNPs indicated in the main figure.

6.4 Validation of the proposed framework

A direct way to validate the proposed framework is to provide specific calculations of the survival curves and/or RBE and to compare the obtained results with available experimental studies. For example, Chen et al., 2020; Penninckx et al., 2020; Zygmanski et al. 2013a summarized existing *in vitro* studies regarding GNP radiosensitization effects. However, these studies do not contain all the necessary information related to irradiation conditions and NP distribution in the cells, which does not allow us to simulate the observed effects. Therefore, to test the proposed analytical scheme and derived equations in this subsection, we repeated the systematic MC study of RBE for X-ray irradiated MDA-231 cells in the presence of GNPs provided by (McMahon et al., 2011a).

Fig. 6.5 presents the predicted RBE values for irradiated MDA-MB-231 cells in the presence of 0.5 mg g^{-1} of GNPs. The left panel shows the dependence of RBE on the GNP diameter

for 40 keV X-rays irradiation, while the right panel presents a variation of RBE with photon energy for 20 nm GNP. The RDDs around GNPs with a diameter of 20 nm, for photon energies between 10 and 150 keV, were assumed to be described by Eq. 4.1.4 with the parameters $D_s(R_{NP}) = 3.3\times10^3$ Gy and a = 0.4 for all the photon energies.

The RBE, as a function of the NP diameter, monotonically increases as the diameter decreases; this is directly related to the increasing contribution of Auger electrons in RDDs for smaller NPs. For NP diameters less than 20 nm, the RBE calculated by us (line) exhibits a more pronounced growth than the RBE simulated by McMahon et al., 2011a. In our opinion, the overestimation of RBE in our calculations comes from the presence of extremely high doses near the surfaces of small NPs. Such high doses at distances less than 10 nm (with doses of thousands of Gy and higher) take into account only initial radiation interactions and do not represent the diffusion of potentially damaging biological and chemical species (Buch et al., 2018; McMahon et al., 2016). The variation of RBE with photon energy reflects the energy dependence of the probability of ionization per irradiation dose in single NPs presented in Fig. 5.1. The jumps in the energy dependence correspond to the sharp increase of the mass-energy absorption coefficient at the L-edges (11.9, 13.8, 14.3 keV) and the K-edge (81.0 keV) of gold. As can be seen from Fig. 6.5, the results obtained using the combined MC simulations and the analytical approach proposed in this work are in excellent agreement with the results of McMahon et al., 2011a.

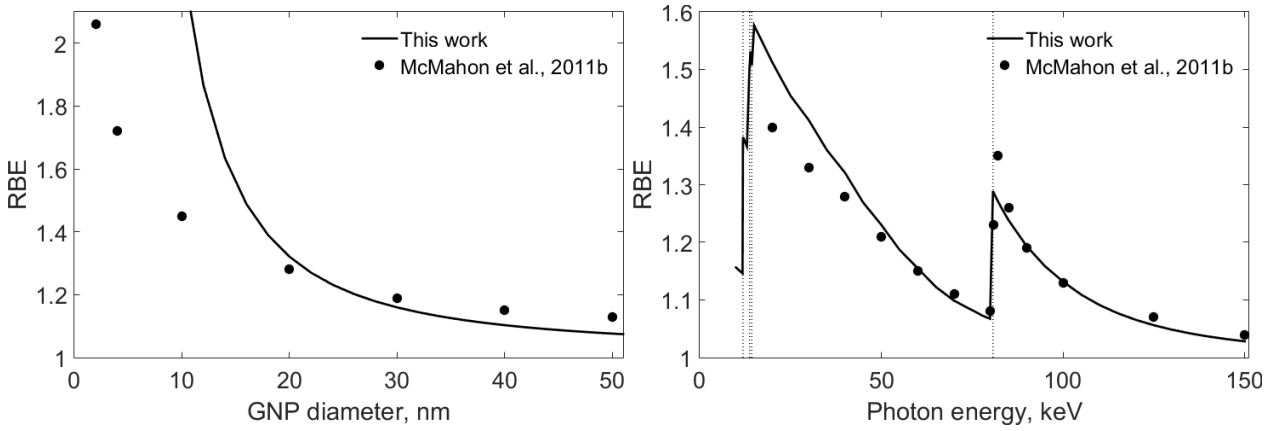

Figure 6.5. Predicted RBE values for irradiated MDA-MB-231 cells in the presence of 0.5 mg/g of GNPs calculated in this work using the proposed framework (lines) and MC simulated by McMahon et al., 2011a (points). Left panel: the dependence of RBE on the GNP diameter for irradiation with 40 keV X-rays. Right panel: a variation of RBE with photon energy for 20 nm diameter GNP. The dotted lines mark the photon energies of the L-edges (11.9, 13.8, 14.3 keV) and the K-edge (81.0 keV) of gold.

CHAPTER 7

Conclusions and future work

7.1 Thesis conclusions

The combined framework proposed in the thesis is developed to describe the radiosensitization effect of high-Z NPs on photon-radiated cells. The framework combines MC simulation of the RDD around a single high-Z NP and analytical evaluation of the average number of lethal lesions in a cell target by a set of ionized NPs aiming to predict the NPs radiosensitization effects. The framework incorporates information regarding the source of irradiation and characteristics of the NPs, such as the size, concentration, cell line, and NP distribution over a cell to assess the extent of the biological outcomes. The analytical approach is based on the LEM extension of the LQ model for NPs loaded cells, developed over the last ten years by several research groups. The main quantity assessed using this approach is the average number of additional lesions formed in a cell target by secondary electrons liberated from ionized NPs. A schematic flowchart representing the process of the cell survival calculation is presented in Appendix 2.

Among a number of models proposed to predict radiobiological response, the linear-quadratic (LQ) model is the best validated by experimental and clinical data and the most used for the representation the cell response to the irradiation treatment, to estimate equivalent radiotherapy schedules, to predict tumor control probability and normal tissue complication probability (van Leeuwen et al., 2018). The LQ model is highly empirical and not comprehensive model. It does not attempt to correlate microscopic effects with cell survival rate and formally is not a mechanistic model. However, in the literature, there have been various attempts at mechanistic modeling of radiation responses (McMahon, 2019; McMahon and Prise, 2019). In our opinion, a promising way to bridge the gap between the interaction of radiation with the cell matter and the local dose deposition in cell structures is to combine MC simulations with an analytical approach. An example of such a hybrid computational framework can be found in an article by Jayarathna et al., 2019 devoted to estimating dose distributions around clustered GNPs irradiated by photons from a Yb-169 source and 6 MV photon beam.

In this work, the MC simulations were used to evaluate the RDD around a single spherical GNP with diameters of 2, 5, 10 and, 50 nm suspended in water irradiated with 10, 30, 100, and

662 keV monoenergetic photon beams and 150 and 250 kVp polyenergetic x-ray beams. For both sets of GNP diameters and photon beams, the MC simulated RDDs were found to be close to straight lines in the double logarithmic scale and were approximated by the power law function (2.21). Moreover, the parameters D_s and a were found to be almost the same for the considered GNP radii and photon energies. Therefore, a simple $1/r^{2+a}$ radial dependence of approximated RDDs allowed us to take the triple integrals and derive explicit expressions for the average dose and the average of the squared dose in a spherical target. The analysis of the data available in the literature on MC simulations of RDDs shows that not all of them can be fitted by the power law function with reasonable precision. However, if that is so, the triple integrals, as well as the integrals expressing the average dose and the average of the squared dose deposited by one ionized NP randomly placed in or outside the target, could be evaluated numerically.

The probability of NP ionization per dose is an essential parameter for the NP extension of the LEM because it determines the efficiency of NP radiosensitization. It can be found using the calculated rate of photoelectric and Compton absorption based on ionization cross-sections for monoenergetic photons or directly by MC calculations. In this work, we have used both methods and have shown that ionization probabilities calculated analytically for monoenergetic photons and polyenergetic x-ray spectra are in good agreement with those found by MC simulations by other researchers, which confirms the performance of the simple analytical approach.

Modern MC simulation packages guarantee a precise calculation of the dose deposition at the nanoscale level (Li et al., 2020). However, they have some disadvantages, such as time-consuming computer simulations or difficulty in simulating the dose deposition from tens or hundreds of millions of NPs within a cellular volume (McMahon et al., 2011b) or clustered NPs. The combined consideration of the radiosensitization effect allows for splitting the problem into two independent steps. Firstly, to find the RDD around a single NP ionized by a photon beam with a given energy spectrum using MC simulation and, after that, analytically evaluate the average dose and the average of the squared dose deposited in the target by a set of ionized NPs. The proposed framework can be applied to evaluate dose enhancement due to the irradiation of NP-loaded cells with a photon beam of any given spectrum. Only two things are needed for this: the simulation of the RDD around a single NP and the calculation of the probability of NP ionization (relative number of ionization events inside NPs per their number) per dose.

The analytical expressions describing average doses deposited in a spherical cell target and fitted by the power law RDDs around GNPs were applied to predict the radiosensitization effect in spherical cells with embedded GNPs irradiated with x-rays. A human breast cancer cell MDA-MB-231, for which an extended set of α and β LQ parameters for various combinations of GNPs and irradiation modalities, was modeled as a water sphere of radius 6.75 μm with a cell nucleus of radius 3 μm concentric to the cell. Additionally, a water shell 2.5 μm width was added outside of the cell to represent the extracellular media region. The calculated NP-related LQ model parameters systematically increase, and the survival curves show a significant reduction in the survival fraction of cells with increasing NP concentration. Both effects are most pronounced for NPs distributed in the target for a given mass fraction of gold. The effect of NPs distributed in the cytoplasm and extracellular region on the LQ parameters and cell survival becomes noticeable when the mass fractions of gold exceed 3 and 10 mg/g, respectively. Taking into account that NPs can not pervade the cell nucleus, the most efficient will be the NPs located near the nucleus. To consider such a case, survival curves for cells loaded to 100, 200, and 300 mg/g of 20 nm GNPs randomly distributed in a perinuclear region of 0.05 μm width and irradiated with 100 keV photons were calculated. The behavior of calculated survival curves and values of the reduction in survival fraction was found to be similar to those of cell survivals presented in the *in-vitro* literature data.

Metrics such as the SER, the mean inactivation dose ratio, and especially the RBE are widely used to quantify the biological effects of the radiation treatment assisted with NPs. In this thesis, we have considered only the RBE quantity. We did not use other metrics because they directly depend on the survival fraction and/or the αNP and βNP parameters. The model results would need additional algebraic manipulations to report such metrics.

Numerous experimental RBE values summarized in the literature for cells loaded with GNPs and irradiated with x-rays are higher than 1.3. Our calculations have shown that to reach such RBE values, the total amount of gold in the perinuclear region must exceed 5×10^4 GNPs of 20 nm diameter or 520 mg/g. The ratio of the cytoplasm and the perinuclear region volumes is equal to 142 for our cell model. This means that the effective weight fraction of gold in the cytoplasm (assuming the homogenous distribution of GNPs) should be higher than 520/142 = 3.7 mg/g or 74 nM. Toxicological studies of GNPs show that gold atom concentrations ranging from nM to μM are most common when studying toxicity (Alkilany and Murphy, 2010). Therefore, the concentration of GNPs in the perinuclear region of the cell at the level of 100 nM and higher is

quite achievable. The case considered above could be applied to the modeling of survival curves and related quantities (RBE, SER, and others) evaluated during the performance of *in vitro* studies of radiosensitization effects. The slight discrepancy between our obtained RBE values and the reported *in vitro* studies can be attributed to the chemical and biological stages of the radiation response enhanced by the GNPs, which were not directly taken into consideration in this approach.

A direct way to validate the proposed framework is to provide specific calculations of the survival curves and/or RBE and to compare the obtained results with available experimental studies. However, these studies do not contain all the necessary information related to irradiation conditions and NP distribution in the cells, which does not allow us to simulate the observed effects. Therefore, to test the proposed analytical scheme and derived equations in this subsection, we repeated the systematic MC study of RBE for x-ray irradiated MDA-231 cells in the presence of 0.5 mg/g GNPs provided by (McMahon et al., 2011a). For the comparison, the dependence of RBE on the GNP diameter for 40 keV x-rays irradiation and a variation of RBE with photon energies between 10 and 150 keV for 20 nm GNP were calculated. The RBE, as a function of the NP diameter, monotonically increases as the diameter decreases; this is directly related to the increasing contribution of Auger electrons in RDDs for smaller NPs. The variation of RBE with photon energy reflects the energy dependence of the probability of ionization per irradiation dose in single NPs. Overall, the results obtained using the combined MC simulations and the analytical approach are in excellent agreement with the results of McMahon et al., 2011a.

Finally, it is worth mentioning that even when the other published models state the basic equations that provide their results, reproducing them is almost impossible. This is due to the use of numerical integration (using various computational frameworks) for assessing the additional number of lesions and the use of internal parameters not reported in the publications. Our reported results can be easily reproduced by substituting the parameters in the presented set of equations. A fast approach to the biological outcomes of specific irradiation treatment assisted with NPs can be easily obtained by replacing a few parameters in the presented equations. Furthermore, the model can be used for whichever nanoparticle composition, allowing the exploration of different materials for the development and proposal of new schemes of radiation therapy assisted with high-Z NPs.

7.2 Future work

The combined framework presented in this thesis may be continued in several different interesting and useful directions. A few promising topics for continued research into high-Z NP radiosensitization are listed below.

(a) The straightforward extension of the developed framework to apply it for quantitative study of the radiobiological response of cells loaded with other NPs, such as with iron oxide, Gd, and, especially, Hf, for which clinical trials are reported.

(b) The explicit analytical expressions were derived for the simplified case of the spherical target and the RDD described by the power law. The proposed framework can be applied to numerical calculations of radiosensitization effects in cells of any 3D geometry with any special distribution of embedded NPs. For this, the average 3D density of NPs in a cell should be specified. After that, the average doses and doses squared deposited in the cell target could be found by numerical integration of corresponding triple integrals.

(c) An essential feature of the proposed analytical approach is the assumption that the squared dose deposited by two ionized NPs located in different cell points can be omitted. This assumption comes from the low probability of NP ionization and is valid for sparsely distributed NPs. On the other hand, it is well known that NPs have a tendency to aggregate and form clusters. Often, large clusters of particles are presented inside vesicles, forming aggregates of hundreds of nanometres in diameter (Peckys and de Jonge, 2011). Clustering leads to overlapping *RDDs* of neighboring NPs that modify the dose enhancement in the vicinity of clusters (Rudek et al., 2019). In this case, it is possible to determine dose distribution around a cluster of NPs as a function of cluster geometry, ensemble size, incident photon energy, and beam angulation with respect to the cluster geometry by MC and, after that, analytically evaluate the average dose and the average of the squared dose deposited by the cluster.

(d) Hadron or ion beam therapy is a specific type of oncological radiotherapy which uses fast hadrons to obtain better dose depositions when compared with the ones of X-rays. It is especially appropriate for cancers with limited treatment options, e.g., eye or brain tumors, tumors

close to the brain stem or spinal cord, etc. The combined framework developed in this thesis can be directly applied to a quantified description of the radiosensitization effect of high-Z NPs on hadron-irradiated cells. For this, the MC simulation of the RDD around a single high-Z NP irradiated with photon beams should be only replaced by the MC simulation for hadron beams.

References

Abdollahi, B.B., Malekzadeh, R., Azar, F.P., Salehnia, F., Naseri, A.R., Ghorbani, M., Hamishehkar, H., Farajollahi, A.R., 2021. Main approaches to enhance radiosensitization in cancer cells by nanoparticles: a systematic review. Adv Pharm Bull 11, 212–223. https://doi.org/10.34172/apb.2021.025

Alejo-Martinez, H., Sevilla-Moreno, A.C., Ondo-Mendéz, A., Quintero, J.H., Páez, C.J., 2019. Comparison of Bi2S3 and Ta2O5 as alternative materials to gold in nanoparticles used as agents to increase the dose in radiotherapy. Presented at the Journal of Physics: Conference Series. https://doi.org/10.1088/1742-6596/1247/1/012050

Alkilany, A.M., Murphy, C.J., 2010. Toxicity and cellular uptake of gold nanoparticles: What we have learned so far? Journal of Nanoparticle Research 12, 2313–2333. https://doi.org/10.1007/s11051-010-9911-8

Bannister, A.H., Bromma, K., Sung, W., Monica, M., Cicon, L., Howard, P., Chow, R.L., Schuemann, J., Chithrani, D.B., 2020. Modulation of nanoparticle uptake, intracellular distribution, and retention with docetaxel to enhance radiotherapy. British Journal of Radiology 93. https://doi.org/10.1259/bjr.20190742

Beasley, M., Driver, D., Dobbs, H.J., 2005. Complications of radiotherapy: Improving the therapeutic index. Cancer Imaging 5, 78–84. https://doi.org/10.1102/1470-7330.2005.0012

Berbeco, R.I., Ngwa, W., Makrigiorgos, G.M., 2011. Localized dose enhancement to tumor blood vessel endothelial cells via megavoltage X-rays and targeted gold nanoparticles: New potential for external beam radiotherapy. International Journal of Radiation Oncology Biology Physics 81, 270–276. https://doi.org/10.1016/j.ijrobp.2010.10.022

Berger, M.J., Coursey, J., Zucker, M., Chang, J., 2017. ESTAR, PSTAR, and ASTAR: Computer programs for calculating stopping-power and range tables for electrons, protons, and helium ions [WWW Document]. https://doi.org/10.18434/T4NC7P

Bodgi, L., Canet, A., Pujo-Menjouet, L., Lesne, A., Victor, J.-M., Foray, N., 2016. Mathematical models of radiation action on living cells: From the target theory to the modern approaches. A historical and critical review. Journal of Theoretical Biology 394, 93–101. https://doi.org/10.1016/j.jtbi.2016.01.018

Bromma, K., Chithrani, D.B., 2020. Advances in gold nanoparticle-based combined cancer therapy. Nanomaterials 10, 1671. https://doi.org/10.3390/nano10091671

Brown, J.M.C., Currell, F.J., 2017. A local effect model-based interpolation framework for experimental nanoparticle radiosensitisation data. Cancer Nanotechnology 8. https://doi.org/10.1186/s12645-016-0025-6

Buch, T., Scifoni, E., Krämer, M., Durante, M., Scholz, M., Friedrich, T., 2018. Modeling radiation effects of ultrasoft X rays on the basis of amorphous track structure. Radiation Research 189, 32–43. https://doi.org/10.1667/RR14653.1

Butterworth, K.T., Coulter, J.A., Jain, S., Forker, J., McMahon, S.J., Schettino, G., Prise, K.M., Currell, F.J., Hirst, D.G., 2010. Evaluation of cytotoxicity and radiation enhancement using 1.9nm gold particles: Potential application for cancer therapy. Nanotechnology 21, 295101. https://doi.org/10.1088/0957-4484/21/29/295101

Butterworth, K.T., McMahon, S.J., Currell, F.J., Prise, K.M., 2012. Physical basis and biological mechanisms of gold nanoparticle radiosensitization. Nanoscale 4, 4830–4838. https://doi.org/10.1039/c2nr31227a

Carter, J.D., Cheng, N.N., Qu, Y., Suarez, G.D., Guo, T., 2007. Nanoscale energy deposition by X-ray absorbing nanostructures. Journal of Physical Chemistry B 111, 11622–11625. https://doi.org/10.1021/jp075253u

Chadwick, K.H., Leenhouts, H.P., 1973. A molecular theory of cell survival. Phys. Med. Biol. 18, 78–87. https://doi.org/10.1088/0031-9155/18/1/007

Chatterjee, A., Magee, J.L., 1985. Theoretical investigation of the production of strand breaks in DNA by water radicals. Radiation Protection Dosimetry 13, 137–140. https://doi.org/10.1093/rpd/13.1-4.137

Chen, Y., Yang, J., Fu, S., Wu, J., 2020. Gold nanoparticles as radiosensitizers in cancer radiotherapy. International Journal of Nanomedicine 15, 9407–9430. https://doi.org/10.2147/IJN.S272902

Chernov, V., Chernov, G., Barboza-Flores, M., 2012. Analytical approximation of the nanoscale dose distribution in an irradiated medium with an embedded nanoparticle. J. Phys.: Conf. Ser. 393, 012035. https://doi.org/10.1088/1742-6596/393/1/012035

Chithrani, B.D., Stewart, J., Allen, C., Jaffray, D.A., 2009. Intracellular uptake, transport, and processing of nanostructures in cancer cells. Nanomedicine: Nanotechnology, Biology and Medicine 5, 118–127. https://doi.org/10.1016/j.nano.2009.01.008

Cho, S.H., 2005. Estimation of tumour dose enhancement due to gold nanoparticles during typical radiation treatments: a preliminary Monte Carlo study. Physics in Medicine & Biology 50, N163. https://doi.org/10.1088/0031-9155/50/15/N01

Choi, J., Kim, G., Cho, S.B., Im, H.-J., 2020. Radiosensitizing high-Z metal nanoparticles for enhanced radiotherapy of glioblastoma multiforme. Journal of Nanobiotechnology 18, 122. https://doi.org/10.1186/s12951-020-00684-5

Chow, J.C.L., 2018. Recent progress in Monte Carlo simulation on gold nanoparticle radiosensitization. AIMS Biophysics 5, 231–244. https://doi.org/10.3934/biophy.2018.4.231

Chow, J.C.L., 2016. Characteristics of secondary electrons from irradiated gold nanoparticle in radiotherapy, in: Handbook of Nanoparticles. pp. 41–65. https://doi.org/10.1007/978-3-319-15338-4_10

Cole, A., 1969. Absorption of 20-eV to 50,000-eV electron beams in air and plastic. Radiation research 38, 7–33. https://doi.org/10.2307/3572707

Corde, S., Joubert, A., Adam, J.F., Charvet, A.M., Le Bas, J.F., Estève, F., Elleaume, H., Balosso, J., 2004. Synchrotron radiation-based experimental determination of the optimal energy for cell radiotoxicity enhancement following photoelectric effect on stable iodinated compounds. British Journal of Cancer 91, 544–551. https://doi.org/10.1038/sj.bjc.6601951

Coulter, J.A., Jain, S., Butterworth, K.T., Taggart, L.E., Dickson, G.R., McMahon, S.J., Hyland, W.B., Muir, M.F., Trainor, C., Hounsell, A.R., O'Sullivan, J.M., Schettino, G., Currell, F.J., Hirst, D.G., Prise, K.M., 2012. Cell type-dependent uptake, localization, and cytotoxicity of

1.9 nm gold nanoparticles. International Journal of Nanomedicine 7, 2673–2685. https://doi.org/10.2147/IJN.S31751

Cucinotta, F.A., Katz, R., Wilson, J.W., Dubey, R.R., 1995. Heavy ion track-structure calculations for radial dose in arbitrary materials. Robert Katz Publications.

Cui, L., Tse, K., Zahedi, P., Harding, S.M., Zafarana, G., Jaffray, D.A., Bristow, R.G., Allen, C., 2014. Hypoxia and cellular localization influence the radiosensitizing effect of gold nanoparticles (AuNPs) in breast cancer cells. Radiation Research 182, 475–488. https://doi.org/10.1667/RR13642.1

Delaney, G.P., Barton, M.B., 2015. Evidence-based Estimates of the Demand for Radiotherapy. Clinical Oncology 27, 70–76. https://doi.org/10.1016/j.clon.2014.10.005

Detappe, A., Tsiamas, P., Ngwa, W., Zygmanski, P., Makrigiorgos, M., Berbeco, R., 2013. The effect of flattening filter free delivery on endothelial dose enhancement with gold nanoparticles. Medical Physics 40. https://doi.org/10.1118/1.4791671

Elsässer, T., Krämer, M., Scholz, M., 2008. Accuracy of the Local Effect Model for the Prediction of Biologic Effects of Carbon Ion Beams In Vitro and In Vivo. International Journal of Radiation Oncology Biology Physics 71, 866–872. https://doi.org/10.1016/j.ijrobp.2008.02.037

Elsässer, T., Scholz, M., 2007. Cluster effects within the local effect model. Radiation Research 167, 319–329. https://doi.org/10.1667/RR0467.1

Elssser, T., Scholz, M., 2010. Comments on "formalization and theoretical analysis of the local effect model" by beuve (Radiat. Res. 172, 394402, 2009). Radiation Research 173, 855–856. https://doi.org/10.1667/RR2089.1

Falk, M., Wolinsky, M., Veldwijk, M.R., Hildenbrand, G., Hausmann, M., 2020. Gold nanoparticle enhanced radiosensitivity of cells: considerations and contradictions from model systems and basic investigations of cell damaging for radiation therapy Nanopart. Enhanced Radiat. Ther 10, 1–25.

Ferrero, V., Visonà, G., Dalmasso, F., Gobbato, A., Cerello, P., Strigari, L., Visentin, S., Attili, A., 2017. Targeted dose enhancement in radiotherapy for breast cancer using gold nanoparticles, part 1: A radiobiological model study. Medical physics 44, 1983–1992. https://doi.org/10.1002/mp.12180

Francis, Z., Incerti, S., Capra, R., Mascialino, B., Montarou, G., Stepan, V., Villagrasa, C., 2011. Molecular scale track structure simulations in liquid water using the Geant4-DNA Monte-Carlo processes. Applied Radiation and Isotopes 69, 220–226. https://doi.org/10.1016/j.apradiso.2010.08.011

Friedrich, T., Durante, M., Scholz, M., 2012. Modeling cell survival after photon irradiation based on double-strand break clustering in megabase pair chromatin loops. Radiation Research 178, 385–394. https://doi.org/10.1667/RR2964.1

Fu, Y., Chin, L.K., Bourouina, T., Liu, A.Q., Vandongen, A.M.J., 2012. Nuclear deformation during breast cancer cell transmigration. Lab on a Chip 12, 3774–3778. https://doi.org/10.1039/c2lc40477j

Gadoue, S.M., Toomeh, D., Zygmanski, P., Sajo, E., 2017. Angular dose anisotropy around gold nanoparticles exposed to X-rays. Nanomedicine: Nanotechnology, Biology, and Medicine 13, 1653–1661. https://doi.org/10.1016/j.nano.2017.02.017

Gong, L., Zhang, Y., Liu, C., Zhang, M., Han, S., 2021. Application of radiosensitizers in cancer radiotherapy. IJN 16, 1083–1102. https://doi.org/10.2147/IJN.S290438

Guo, T., 2018. X-ray nanochemistry: Concepts and development. Springer.

Hainfeld, J.F., Slatkin, D.N., Smilowitz, H.M., 2004. The use of gold nanoparticles to enhance radiotherapy in mice. Physics in Medicine and Biology 49, N309–N315. https://doi.org/10.1088/0031-9155/49/18/N03

He, C., Chow, J.C.L., 2016. Gold nanoparticle DNA damage in radiotherapy: A Monte Carlo study. Bioengineering 2016, Vol. 3, Pages 352-361. https://doi.org/10.3934/bioeng.2016.3.352

Her, S., Jaffray, D.A., Allen, C., 2017. Gold nanoparticles for applications in cancer radiotherapy: Mechanisms and recent advancements. Advanced Drug Delivery Reviews 109, 84–101. https://doi.org/10.1016/j.addr.2015.12.012

Hossain, M., Su, M., 2012. Nanoparticle location and material-dependent dose enhancement in X-ray radiation therapy. Journal of Physical Chemistry C 116, 23047–23052. https://doi.org/10.1021/jp306543q

ICRU Report 85, 2011. Fundamental quantities and units for ionizing radiation (revised). Oxford University Press. https://doi.org/10.1093/jicru/ndr012

ICRU Report 86, 2011. Quantification and reporting of low-dose and other heterogeneous exposures. Oxford Academic. https://doi.org/10.1093/jicru/ndr028

Jabeen, M., Chow, J.C.L., 2021. Gold nanoparticle DNA damage by photon beam in a magnetic field: A Monte Carlo study. Nanomaterials 11, 1751. https://doi.org/10.3390/nano11071751

Jain, S., Coulter, J.A., Hounsell, A.R., Butterworth, K.T., McMahon, S.J., Hyland, W.B., Muir, M.F., Dickson, G.R., Prise, K.M., Currell, F.J., O'Sullivan, J.M., Hirst, D.G., 2011. Cell-Specific Radiosensitization by gold nanoparticles at megavoltage radiation energies. International Journal of Radiation Oncology Biology Physics 79, 531–539. https://doi.org/10.1016/j.ijrobp.2010.08.044

Jayarathna, S., Manohar, N., Ahmed, M.F., Krishnan, S., Cho, S.H., 2019. Evaluation of dose point kernel rescaling methods for nanoscale dose estimation around gold nanoparticles using Geant4 Monte Carlo simulations. Scientific Reports 9. https://doi.org/10.1038/s41598-019-40166-9

Joiner, M.C., Kogel, A. van der, 2018. Basic clinical radiobiology, Fifth edition. CRC Press.

Jones, B.L., Krishnan, S., Cho, S.H., 2010. Estimation of microscopic dose enhancement factor around gold nanoparticles by Monte Carlo calculations. Medical Physics 37, 3809–3816. https://doi.org/10.1118/1.3455703

Jung, S., Sung, W., Ye, S.-J., 2018. Low-energy electron dose-point kernels and radial dose distributions around gold nanoparticles: Comparison between MCNP6.1, PENELOPE2014 and Geant4-DNA. Nuclear Instruments and Methods in Physics Research, Section B: Beam

Interactions with Materials and Atoms 430, 18–22. https://doi.org/10.1016/j.nimb.2018.06.001

Kempson, I., 2021. Mechanisms of nanoparticle radiosensitization. WIREs Nanomedicine and Nanobiotechnology 13, e1656. https://doi.org/10.1002/wnan.1656

Kirkby, C., Koger, B., 2020. Nanoparticle-aided radiation therapy: challenges of treatment planning, in: Nanoparticle Enhanced Radiation Therapy. IOP Publishing, pp. 6–1. https://doi.org/10.1088/978-0-7503-2396-3ch6

Kraft, G., Scholz, M., Bechthold, U., 1999. Tumor therapy and track structure. Radiat Environ Biophys 38, 229–237. https://doi.org/10.1007/s004110050163

Kuncic, Z., Lacombe, S., 2018. Nanoparticle radio-enhancement: Principles, progress and application to cancer treatment. Physics in Medicine and Biology 63. https://doi.org/10.1088/1361-6560/aa99ce

Kwatra, D., Venugopal, A., Anant, S., 2013. Nanoparticles in radiation therapy: A summary of various approaches to enhance radiosensitization in cancer. Translational Cancer Research 2, 330–342. https://doi.org/10.3978/j.issn.2218-676X.2013.08.06

Lampe, N., Karamitros, M., Breton, V., Brown, J.M.C., Kyriakou, I., Sakata, D., Sarramia, D., Incerti, S., 2018. Mechanistic DNA damage simulations in Geant4-DNA part 1: A parameter study in a simplified geometry. Physica Medica: European Journal of Medical Physics 48, 135–145. https://doi.org/10.1016/j.ejmp.2018.02.011

Lechtman, E., Chattopadhyay, N., Cai, Z., Mashouf, S., Reilly, R., Pignol, J.P., 2011. Implications on clinical scenario of gold nanoparticle radiosensitization in regards to photon energy, nanoparticle size, concentration and location. Physics in Medicine and Biology 56, 4631–4647. https://doi.org/10.1088/0031-9155/56/15/001

Lechtman, E., Mashouf, S., Chattopadhyay, N., Keller, B.M., Lai, P., Cai, Z., Reilly, R.M., Pignol, J.-P., 2013. A Monte Carlo-based model of gold nanoparticle radiosensitization accounting for increased radiobiological effectiveness. Physics in Medicine and Biology 58, 3075–3087. https://doi.org/10.1088/0031-9155/58/10/3075

Leung, M.K.K., Chow, J.C.L., Chithrani, B.D., Lee, M.J.G., Oms, B., Jaffray, D.A., 2011. Irradiation of gold nanoparticles by x-rays: Monte Carlo simulation of dose enhancements and the spatial properties of the secondary electrons production. Medical Physics 38, 624–631. https://doi.org/10.1118/1.3539623

Li, W.B., Belchior, A., Beuve, M., Chen, Y.Z., Di Maria, S., Friedland, W., Gervais, B., Heide, B., Hocine, N., Ipatov, A., Klapproth, A.P., Li, C.Y., Li, J.L., Multhoff, G., Poignant, F., Qiu, R., Rabus, H., Rudek, B., Schuemann, J., Stangl, S., Testa, E., Villagrasa, C., Xie, W.Z., Zhang, Y.B., 2020. Intercomparison of dose enhancement ratio and secondary electron spectra for gold nanoparticles irradiated by X-rays calculated using multiple Monte Carlo simulation codes. Physica Medica 69, 147–163. https://doi.org/10.1016/j.ejmp.2019.12.011

Lin, Y., McMahon, S.J., Paganetti, H., Schuemann, J., 2015. Biological modeling of gold nanoparticle enhanced radiotherapy for proton therapy. Physics in Medicine and Biology 60, 4149–4168. https://doi.org/10.1088/0031-9155/60/10/4149

Lin, Y., McMahon, S.J., Scarpelli, M., Paganetti, H., Schuemann, J., 2014. Comparing gold nano-particle enhanced radiotherapy with protons, megavoltage photons and kilovoltage photons: A Monte Carlo simulation. Physics in Medicine and Biology 59, 7675–7689. https://doi.org/10.1088/0031-9155/59/24/7675

Maeda, H., Wu, J., Sawa, T., Matsumura, Y., Hori, K., 2000. Tumor vascular permeability and the EPR effect in macromolecular therapeutics: A review. Journal of Controlled Release 65, 271–284. https://doi.org/10.1016/S0168-3659(99)00248-5

Martinov, M.P., Thomson, R.M., 2017. Heterogeneous multiscale Monte Carlo simulations for gold nanoparticle radiosensitization: Medical Physics 44, 644–653. https://doi.org/10.1002/mp.12061

Matsudaira, H., Ueno, A.M., Furuno, I., 1980. Iodine contrast medium sensitizes cultured mammalian cells to X rays but not to γ rays. Radiation Research 84, 144–148. https://doi.org/10.2307/3575225

McMahon, S.J., 2019. The linear quadratic model: Usage, interpretation and challenges. Physics in Medicine and Biology 64. https://doi.org/10.1088/1361-6560/aaf26a

McMahon, S.J., Currell, F.J., 2013. Gold nanoparticles for imaging and radiotherapy. Frontiers of Nanoscience 5, 65–93. https://doi.org/10.1016/B978-0-08-098338-7.00003-0

McMahon, S.J., Hyland, W.B., Muir, M.F., Coulter, J.A., Jain, S., Butterworth, K.T., Schettino, G., Dickson, G.R., Hounsell, A.R., O'Sullivan, J.M., Prise, K.M., Hirst, D.G., Currell, F.J., 2011a. Biological consequences of nanoscale energy deposition near irradiated heavy atom nanoparticles. Scientific Reports 1. https://doi.org/10.1038/srep00018

McMahon, S.J., Hyland, W.B., Muir, M.F., Coulter, J.A., Jain, S., Butterworth, K.T., Schettino, G., Dickson, G.R., Hounsell, A.R., O'Sullivan, J.M., Prise, K.M., Hirst, D.G., Currell, F.J., 2011b. Nanodosimetric effects of gold nanoparticles in megavoltage radiation therapy. Radiotherapy and Oncology 100, 412–416. https://doi.org/10.1016/j.radonc.2011.08.026

McMahon, S.J., Paganetti, H., Prise, K.M., 2016. Optimising element choice for nanoparticle radiosensitisers. Nanoscale 8, 581–589. https://doi.org/10.1039/c5nr07089a

McMahon, S.J., Prise, K.M., 2019. Mechanistic modelling of radiation responses. Cancers 11. https://doi.org/10.3390/cancers11020205

McQuaid, H.N., Muir, M.F., Taggart, L.E., McMahon, S.J., Coulter, J.A., Hyland, W.B., Jain, S., Butterworth, K.T., Schettino, G., Prise, K.M., 2016. Imaging and radiation effects of gold nanoparticles in tumour cells. Scientific reports 6, 19442. https://doi.org/10.1038/srep19442

Meesungnoen, J., Jay-Gerin, J.-P., Filali-Mouhim, A., Mankhetkorn, S., 2002. Low-energy electron penetration range in liquid water. Radiation Research 158, 657–660. https://doi.org/10.1667/0033-7587(2002)158[0657:LEEPRI]2.0.CO;2

Melo-Bernal, W., Chernov, V., Chernov, G., Barboza-Flores, M., 2018. Nanoscale dose deposition in cell structures under X-ray irradiation treatment assisted with nanoparticles: An analytical approach to the relative biological effectiveness. Applied Radiation and Isotopes 138, 50–55. https://doi.org/10.1016/j.apradiso.2017.05.020

Mesbahi, A., 2010. A review on gold nanoparticles radiosensitization effect in radiation therapy of cancer. Reports of Practical Oncology and Radiotherapy 15, 176–180. https://doi.org/10.1016/j.rpor.2010.09.001

Mirkin, C., Meade, T.J., Petrosko, S.H., Stegh, A.H. (Eds.), 2015. Nanotechnology-based precision tools for the detection and treatment of cancer, Cancer Treatment and Research. Springer International Publishing. https://doi.org/10.1007/978-3-319-16555-4

Misawa, M., Takahashi, J., 2011. Generation of reactive oxygen species induced by gold nanoparticles under x-ray and UV Irradiations. Nanomedicine: Nanotechnology, Biology and Medicine 7, 604–614. https://doi.org/10.1016/j.nano.2011.01.014

Moradi, F., Rezaee Ebrahim Saraee, K., Abdul Sani, S.F., Bradley, D.A., 2021. Metallic nanoparticle radiosensitization: The role of Monte Carlo simulations towards progress. Radiation Physics and Chemistry 180, 109294. https://doi.org/10.1016/j.radphyschem.2020.109294

Neira, S., Gago-Arias, A., Guiu-Souto, J., Pardo-Montero, J., 2020. A kinetic model of continuous radiation damage to populations of cells: comparison to the LQ model and application to molecular radiotherapy. Phys. Med. Biol. 65, 245015. https://doi.org/10.1088/1361-6560/aba21d

Ngwa, W., Boateng, F., Kumar, R., Irvine, D.J., Formenti, S., Ngoma, T., Herskind, C., Veldwijk, M.R., Hildenbrand, G.L., Hausmann, M., Wenz, F., Hesser, J., 2017. Smart radiation therapy biomaterials. International Journal of Radiation Oncology, Biology, Physics 97, 624–637. https://doi.org/10.1016/j.ijrobp.2016.10.034

Ngwa, W., Makrigiorgos, G.M., Berbeco, R.I., 2010. Applying gold nanoparticles as tumor-vascular disrupting agents during brachytherapy: Estimation of endothelial dose enhancement. Physics in Medicine and Biology 55, 6533–6548. https://doi.org/10.1088/0031-9155/55/21/013

Noireaux, J., Grall, R., Hullo, M., Chevillard, S., Oster, C., Brun, E., Sicard-Roselli, C., Loeschner, K., Fisicaro, P., 2019. Gold nanoparticle uptake in tumor cells: quantification and size distribution by sp-ICPMS Separations 6.

Peckys, D.B., De Jonge, N., 2011. Visualizing gold nanoparticle uptake in live cells with liquid scanning transmission electron microscopy. Nano Letters 11, 1733–1738. https://doi.org/10.1021/nl200285r

Penninckx, S., Heuskin, A.-C., Michiels, C., Lucas, S., 2020. Gold nanoparticles as a potent radiosensitizer: A transdisciplinary approach from physics to patient. Cancers 12, 1–361. https://doi.org/10.3390/cancers12082021

Perkins, S.T., Cullen, D.E., 1994. ENDL type formats for the LLNL evaluated atomic data library, (EADL), for the evaluated electron data library, (EEDL), and for the evaluated photon data library, (EPDL). ENDL Type Formats for the LLNL Evaluated Atomic Data Library, EADL, for the Evaluated Electron Data Library, EEDL, and for the Evaluated Photon Data Library, EPDL.

Perl, J., Shin, J., Schümann, J., Faddegon, B., Paganetti, H., 2012. TOPAS: An innovative proton Monte Carlo platform for research and clinical applications. Medical Physics 39, 6818–6837. https://doi.org/10.1118/1.4758060

Pfuhl, T., Friedrich, T., Scholz, M., 2020. Prediction of cell survival after exposure to mixed radiation fields with the local effect model. Radiation Research 193, 130–142. https://doi.org/10.1667/RR15456.1

Pimblott, S.M., Siebbeles, L.D.A., 2002. Energy loss by non-relativistic electrons and positrons in liquid water. Nuclear Instruments and Methods in Physics Research Section B: Beam Interactions with Materials and Atoms 194, 237–250. https://doi.org/10.1016/S0168-583X(02)00693-6

Podgorsak, E.B., 2014. Compendium to radiation physics for medical physicists: 300 problems and solutions. Springer-Verlag, Berlin Heidelberg. https://doi.org/10.1007/978-3-642-20186-8

Poignant, F., Charfi, H., Chan, C.-H., Dumont, E., Loffreda, D., Testa, É., Gervais, B., Beuve, M., 2020. Monte Carlo simulation of free radical production under keV photon irradiation of gold nanoparticle aqueous solution. Part I: Global primary chemical boost. Radiation Physics and Chemistry 172. https://doi.org/10.1016/j.radphyschem.2020.108790

Poludniowski, G., Landry, G., Deblois, F., Evans, P.M., Verhaegen, F., 2009. SpekCalc: A program to calculate photon spectra from tungsten anode x-ray tubes. Physics in Medicine and Biology 54, N433–N438. https://doi.org/10.1088/0031-9155/54/19/N01

Pyrz, W.D., Buttrey, D.J., 2008. Particle size determination using TEM: A discussion of image acquisition and analysis for the novice microscopist. Langmuir 24, 11350–11360. https://doi.org/10.1021/la801367j

Rabus, H., Gargioni, E., Li, W.B., Nettelbeck, H., Villagrasa, C., 2019. Determining dose enhancement factors of high-Z nanoparticles from simulations where lateral secondary particle disequilibrium exists. Physics in Medicine and Biology 64. https://doi.org/10.1088/1361-6560/ab31d4

Rahman, W.N., Bishara, N., Ackerly, T., He, C.F., Jackson, P., Wong, C., Davidson, R., Geso, M., 2009. Enhancement of radiation effects by gold nanoparticles for superficial radiation therapy. Nanomedicine: Nanotechnology, Biology, and Medicine 5, 136–142. https://doi.org/10.1016/j.nano.2009.01.014

Rahman, W.N., Corde, S., Yagi, N., Aziz, S.A.A., Annabell, N., Geso, M., 2014. Optimal energy for cell radiosensitivity enhancement by gold nanoparticles using synchrotron-based monoenergetic photon beams. IJN 9, 2459–2467. https://doi.org/10.2147/IJN.S59471

Retif, P., Pinel, S., Toussaint, M., Frochot, C., Chouikrat, R., Bastogne, T., Barberi-Heyob, M., 2015. Nanoparticles for radiation therapy enhancement: the key parameters. Theranostics 5, 1030. https://doi.org/10.7150/thno.11642

Rieck, K., Bromma, K., Sung, W., Bannister, A., Schuemann, J., Chithrani, D.B., 2019. Modulation of gold nanoparticle mediated radiation dose enhancement through synchronization of breast tumor cell population. British Journal of Radiology 92. https://doi.org/10.1259/bjr.20190283

Roeske, J.C., Nuñez, L., Hoggarth, M., Labay, E., Weichselbaum, R.R., 2007. Characterization of the theorectical radiation dose enhancement from nanoparticles. Technology in Cancer Research and Treatment 6, 395–401. https://doi.org/10.1177/153303460700600504

Rudek, B., McNamara, A., Ramos-Méndez, J., Byrne, H., Kuncic, Z., Schuemann, J., 2019. Radio-enhancement by gold nanoparticles and their impact on water radiolysis for x-ray, proton and carbon-ion beams. Physics in Medicine and Biology 64. https://doi.org/10.1088/1361-6560/ab314c

Ryschich, E., Schmidt, E., Maksan, S.-M., Klar, E., Schmidt, J., 2004. Expansion of endothelial surface by an increase of vessel diameter during tumor angiogenesis in experimental hepatocellular and pancreatic cancer. World Journal of Gastroenterology 10, 3171–3174. https://doi.org/10.3748/wjg.v10.i21.3171

Sajo, E., Cifter, F., Zygmanski, P., 2020a. Deterministic computation benchmarks of nanoparticle dose enhancement—part I. Nanometer scales. Nanoparticle Enhanced Radiation Therapy, 2053-2563. https://doi.org/10.1088/978-0-7503-2396-3ch2

Sajo, E., Cifter, F., Zygmanski, P., 2020b. Deterministic computation benchmarks of nanoparticle dose enhancement—part II. Microscopic to macroscopic scales, in: Nanoparticle Enhanced Radiation Therapy. IOP Publishing, pp. 3–1. https://doi.org/10.1088/978-0-7503-2396-3ch3

Sajo, E., Zygmanski, P., 2020. Nanoparticle enhanced radiation therapy; principles, methods and applications. IOP Publishing. https://doi.org/10.1088/978-0-7503-2396-3

Sakata, D., Belov, O., Bordage, M.-C., Emfietzoglou, D., Guatelli, S., Inaniwa, T., Ivanchenko, V., Karamitros, M., Kyriakou, I., Lampe, N., Petrovic, I., Ristic-Fira, A., Shin, W.-G., Incerti, S., 2020. Fully integrated Monte Carlo simulation for evaluating radiation induced DNA damage and subsequent repair using Geant4-DNA. Sci Rep 10, 20788. https://doi.org/10.1038/s41598-020-75982-x

Scholz, M., 2006. Chapter 1 - dose response of biological systems to low- and high-LET radiation, in: Horowitz, Y. (Ed.), Microdosimetric Response of Physical and Biological Systems to Low- and High-LET Radiations. Elsevier Science, Amsterdam, pp. 1–73. https://doi.org/10.1016/B978-044451643-5/50013-7

Scholz, M., Friedrich, T., Magrin, G., Colautti, P., Ristić-Fira, A., Petrović, I., 2020. Characterizing Radiation Effectiveness in Ion Beam Therapy Part I: Introduction and Biophysical Modeling of RBE Using the LEMIV. Frontiers in Physics 8. https://doi.org/10.3389/fphy.2020.00272

Schuemann, J., Bagley, A.F., Berbeco, R., Bromma, K., Butterworth, K.T., Byrne, H.L., Chithrani, B.D., Cho, S.H., Cook, J.R., Favaudon, V., Gholami, Y.H., Gargioni, E., Hainfeld, J.F., Hespeels, F., Heuskin, A.-C., Ibeh, U.M., Kuncic, Z., Kunjachan, S., Lacombe, S., Lucas, S., Lux, F., McMahon, S., Nevozhay, D., Ngwa, W., Payne, J.D., Penninckx, S., Porcel, E., Prise, K.M., Rabus, H., Ridwan, S.M., Rudek, B., Sanche, L., Singh, B., Smilowitz, H.M., Sokolov, K.V., Sridhar, S., Stanishevskiy, Y., Sung, W., Tillement, O., Virani, N., Yantasee, W., Krishnan, S., 2020. Roadmap for metal nanoparticles in radiation therapy: current status, translational challenges, and future directions. Phys. Med. Biol. 65, 21RM02. https://doi.org/10.1088/1361-6560/ab9159

Schuemann, J., Berbeco, R., Chithrani, D.B., Cho, S.H., Kumar, R., McMahon, S.J., Sridhar, S., Krishnan, S., 2016. Roadmap to clinical use of gold nanoparticles for radiation sensitization. International Journal of Radiation Oncology Biology Physics 94, 189–205. https://doi.org/10.1016/j.ijrobp.2015.09.032

Seltzer, S.M., Bartlett, D.T., Burns, D.T., Dietze, G., Menzel, H.-G., Paretzke, H.G., Wambersie, A., 2011. . J. ICRU 11 NP.2 85.

Shahhoseini, E., Ramachandran, P., Patterson, W.R., Geso, M., 2018. Determination of dose enhancement caused by AuNPs with Xoft® Axxent® Electronic (eBx^{TM}) and conventional brachytherapy: in vitro study. International journal of nanomedicine 13, 5733. https://doi.org/10.2147/IJN.S174624

Shang, J., Gao, X., 2014. Nanoparticle counting: Towards accurate determination of the molar concentration. Chemical Society Reviews 43, 7267–7278. https://doi.org/10.1039/c4cs00128a

Subiel, A., Ashmore, R., Schettino, G., 2016. Standards and methodologies for characterizing radiobiological impact of high-Z nanoparticles. Theranostics 6, 1651–1671. https://doi.org/10.7150/THNO.15019

Sung, W., Schuemann, J., 2018. Energy optimization in gold nanoparticle enhanced radiation therapy. Physics in Medicine and Biology 63. https://doi.org/10.1088/1361-6560/aacab6

Sung, W., Ye, S.-J., McNamara, A.L., McMahon, S.J., Hainfeld, J., Shin, J., Smilowitz, H.M., Paganetti, H., Schuemann, J., 2017. Dependence of gold nanoparticle radiosensitization on cell geometry. Nanoscale 9, 5843–5853. https://doi.org/10.1039/c7nr01024a

Thanekar, A.M., Sankaranarayanan, S.A., Rengan, A.K., 2021. Role of nano-sensitizers in radiation therapy of metastatic tumors. Cancer Treatment and Research Communications 26, 100303. https://doi.org/10.1016/j.ctarc.2021.100303

Tran, H.N., Karamitros, M., Ivanchenko, V.N., Guatelli, S., McKinnon, S., Murakami, K., Sasaki, T., Okada, S., Bordage, M.C., Francis, Z., El Bitar, Z., Bernal, M.A., Shin, J.I., Lee, S.B., Barberet, Ph., Tran, T.T., Brown, J.M.C., Nhan Hao, T.V., Incerti, S., 2016. Geant4 Monte Carlo simulation of absorbed dose and radiolysis yields enhancement from a gold nanoparticle under MeV proton irradiation. Nuclear Instruments and Methods in Physics Research Section B: Beam Interactions with Materials and Atoms 373, 126–139. https://doi.org/10.1016/j.nimb.2016.01.017

Uehara, S., Nikjoo, H., Goodhead, D.T., 1999. Comparison and assessment of electron cross sections for monte carlo track structure codes. Radiation Research 152, 202–213. https://doi.org/10.2307/3580095

Valentin, J., Cox, R., Kellerer, A.M., 2003. Relative biological effectiveness (RBE), quality factor (Q), and radiation weighting factor (wR). Annals of the ICRP 33, 1–121. https://doi.org/10.1016/S0146-6453(03)00024-1

van Leeuwen, C.M., Oei, A.L., Crezee, J., Bel, A., Franken, N.A.P., Stalpers, L.J.A., Kok, H.P., 2018. The alfa and beta of tumours: A review of parameters of the linear-quadratic model, derived from clinical radiotherapy studies. Radiation Oncology 13. https://doi.org/10.1186/s13014-018-1040-z

Verhaegen, F., Seuntjens, J., 2003. Monte Carlo modelling of external radiotherapy photon beams. Physics in Medicine and Biology 48, R107–R164. https://doi.org/10.1088/0031-9155/48/21/R01

Villagomez-Bernabe, B., Currell, F.J., 2019. Physical Radiation Enhancement Effects Around Clinically Relevant Clusters of Nanoagents in Biological Systems. Scientific Reports 9. https://doi.org/10.1038/s41598-019-44482-y

Vlastou, E., Diamantopoulos, S., Efstathopoulos, E.P., 2020. Monte Carlo studies in gold nanoparticles enhanced radiotherapy: The impact of modelled parameters in dose enhancement. Physica Medica: European Journal of Medical Physics 80, 57–64. https://doi.org/10.1016/j.ejmp.2020.09.022

Wang, H., Mu, X., He, H., Zhang, X.-D., 2018. Cancer Radiosensitizers. Trends in Pharmacological Sciences 39, 24–48. https://doi.org/10.1016/j.tips.2017.11.003

Wang, S., Liu, Y., Feng, Y., Zhang, J., Swinnen, J., Li, Y., Ni, Y., 2019. A review on curability of cancers: More efforts for novel therapeutic options are needed. Cancers 11. https://doi.org/10.3390/cancers11111782

Wilson, W.E., Miller, J.H., Lynch, D.J., Lewis, R.R., Batdorf, M., 2004. Analysis of low-energy electron track structure in liquid water. Radiation Research 161, 591–596. https://doi.org/10.1667/RR3179

Xie, W.Z., Friedland, W., Li, W.B., Li, C.Y., Oeh, U., Qiu, R., Li, J.L., Hoeschen, C., 2015. Simulation on the molecular radiosensitization effect of gold nanoparticles in cells irradiated by x-rays. Physics in Medicine and Biology 60, 6195–6212. https://doi.org/10.1088/0031-9155/60/16/6195

Yang, C., Bromma, K., Sung, W., Schuemann, J., Chithrani, D., 2018. Determining the radiation enhancement effects of gold nanoparticles in cells in a combined treatment with cisplatin and radiation at therapeutic megavoltage energies. Cancers 10. https://doi.org/10.3390/cancers10050150

Zhang, S.X., Gao, J., Buchholz, T.A., Wang, Z., Salehpour, M.R., Drezek, R.A., Yu, T.-K., 2009. Quantifying tumor-selective radiation dose enhancements using gold nanoparticles: A monte carlo simulation study. Biomedical Microdevices 11, 925–933. https://doi.org/10.1007/s10544-009-9309-5

Zheng, L., Zhu, R., Chen, L., Fu, Q., Li, J., Chen, C., Song, J., Yang, H., 2021. X-ray sensitive high-Z metal nanocrystals for cancer imaging and therapy. Nano Res. https://doi.org/10.1007/s12274-021-3337-8

Zygmanski, P., Hoegele, W., Tsiamas, P., Cifter, F., Ngwa, W., Berbeco, R., Makrigiorgos, M., Sajo, E., 2013a. A stochastic model of cell survival for high-Z nanoparticle radiotherapy. Medical Physics 40. https://doi.org/10.1118/1.4773885

Zygmanski, P., Liu, B., Tsiamas, P., Cifter, F., Petersheim, M., Hesser, J., Sajo, E., 2013b. Dependence of Monte Carlo microdosimetric computations on the simulation geometry of gold nanoparticles. Physics in Medicine and Biology 58, 7961–7977. https://doi.org/10.1088/0031-9155/58/22/7961

Zygmanski, P., Sajo, E., 2016. Nanoscale radiation transport and clinical beam modeling for gold nanoparticle dose enhanced radiotherapy (GNPT) using X-rays. British Journal of Radiology 89. https://doi.org/10.1259/bjr.20150200

APPENDIX 1

Monte Carlo Simulation of the transport of particles in TOPAS

1.1 Generalities of Monte Carlo Method for photon and electron transport.

The Monte Carlo method is defined by (Bielajew., 2000) as a numerical solution to a problem that models objects interacting with other objects or their environment based on simple object-object or object-environment relationships. Therefore, it represents an attempt to model nature through direct simulation of the essential dynamics of the system in question. In this sense, the Monte Carlo method is essentially simple in its approach – a solution to a macroscopic system through simulation of its microscopic interactions.

The Monte Carlo particle transport tries to mimic the natural behavior of particles traveling through matter. In the process of mimicking the transport of radiation through matter, some components are required: a particle source (for example, an X-ray tube, LINAC, proton beam), an irradiated object (and its geometry), a compound of a defined material or mix of materials (e.g., water like tissue, gold), the physical relevant process to consider and the definition of the scorers that will store the information that the experimenter wants to collect.

Intending to understand the software and not use it as a "black box" that must be taken on faith, in this appendix, we are going clarify the functions being performed by the various components of the software. The reader will be able to understand the different stages of the simulations and have examples of some of the capabilities of the software and the codes of the simulations we run.

Ingredients of a MC transport simulation.

- A random number generator
- Methods for sampling random quantities from a probability distribution function (pdf) (e.g., sampling the distance to the next interaction)
- Bookkeeping (accumulate results)
- Geometry description
- Physics input: Total and differential cross sections.

1.2 MC simulations in TOPAS.

Topas (TOPAS) extend the Geant4 simulation software providing an application straightforward to use in medical physics scenarios. It is able to be modified or expanded to suit the needs of a particular calculation. TOPAS was developed by a collaboration of MGH, SLAC, and UCSF is based on the Geant4 toolkit, and was designed to be flexible and easy to use.
The software is available at http://www.topasmc.org/, and the documentation is presented at https://topas.readthedocs.io/en/latest/.

The simulation is defined by a single text file (control document or parameter file) that significantly simplifies the set of files used in Geant4. The advantage of the sole parameter control document of TOPAS is that it allows the assembly and manipulation of a flexible library of simulation objects such as the geometries, sources of particles, scorers, physical processes, etc. With no need to write C++ code.

To simplify the control document, we adopt the "hierarchical" structure of the different simulation components introduced in the examples of TOPAS, even if there is no hierarchy in the order of the components.
The components of the control document of our simulations were the following:
- Physics definitions.
- Geometrical components and material composition.
- Beam location and spectral components.
- Scorers definition.
- Visualization.

In the following paragraphs, we briefly explain the function of each one of the components of our control document and the parameters that we set for the optimal simulation of our systems of interest. It is worth mentioning that TOPAS has a set of default parameters that allow the easy use of the software and do not appear explicitly in the control document designed by the user. These parameters do not affect the performance of the simulation, and they can be easily modified if they provide better performance or extra and advanced information for the researcher; these default parameters can be found in the TOPAS documentation.

The control document file is a text file (.txt) that defines the simulation setup; the parameters are defined following a well-defined syntaxis. For example, the structure to define a parameter is *Parameter_Type: Parameter_Name = Parameter_Value # optional comment or description*. The information after the # is omitted by the software while compiling and processing; it is an option to describe the criteria for selecting specific values for the parameters.

The parameters are of different types:

- s: string
- b: Boolean quantity
- d: dimensional number
- i: integer
- u: unitless number
- v: vector, (requires type and number of elements)

A convention of parameter names is used to facilitate the readability of the control document sections:

-Ma/ Materials

-So/ Particle Source

-Gr/ Graphics

-El/ Elements

-Ph/ Physics

-Tf/ Time features

-Vr/ Variance Reduction

-Ts/ Topas overall control

-Ge/ Geometry components

-Sc/ Scoring

TOPAS was built with a set of pre-defined parameters that include:

* Overall control (seed of generator of random numbers, the number of treads used for the simulation, ...)

* World volume (10x10x10 m3 of air) These are the default dimensions of the space in which you can locate your objects and sources

* Chemical elements and standard materials. All Elements have been pre-defined with natural isotope abundance from the NIST database. The user can also use any of the Materials and Compounds defined by default in Geant4 or define their own.
* Particle source of mono-energetic protons beam of 169.23 MeV proton
* Physics settings in which they set the physics modules that will propagate the particles and parameters as the minimum energy to propagate a particle.

A complete list of defined default parameters can be found in the TOPAS User Guide.

Physics definitions.
Defines the type of interactions and physical models for each particle type. The transport thresholds and variance reduction parameters are also defined.
This component states the physics modules that TOPAS uses to run the simulation. For this research, we use the low-energy electromagnetic packages Livermore and Penelope. In the low-energy Livermore library, the evolution of photons and electrons from 10eV up to 1 GeV is available based on publicly available evaluated tables from the Livermore data library. It includes elements from Z=1 to Z=100, the atomic effects (fluorescence, Auger), and atomic relaxation for Z > 5 (EADL transition data).

The Penelope package includes the low-energy models for electrons, positrons, and photons from the Monte Carlo code PENELOPE (PENetration and Energy LOss of Positrons and Electrons) version 2008. (Nucl. Instrum. Meth. B 207 (2003) 107-123) It allows the evolution of photons, electrons, and positrons from 100 eV up to 1GeV, in this effort is dedicated to the low-energy description of atomic effects, fluorescence, and doppler broadening.

The modules state the processes through which the particles can interact. The photon processes include: γ conversion into e+ e- pair, Compton scattering, Photoelectric effect, and Rayleigh scattering. The electron and positron processes include: ionization, Coulomb scattering, Bremsstrahlung, and positron annihilation. A physical process can be simulated according to several models, for example, G4LivermoreComptonModel. Models can be assigned to *specific* energy ranges and special regions and provide the computation of cross section and

stopping power, sample selection of atom in *the compound* and final states (kinematics, production of secondaries, etc.) (Koi.,2016)

The probability of each interaction is given by its cross sections; different tables with this information are used depending on the physics model. The distance each particle penetrates in the volume before interacting is a random quantity (generated by random numbers) and requires sampling from a probability density function PDF. In the interaction, secondary particles can be created and need to be further transported, e.g., scattered photons, auger electrons, and electrons in the Coulomb scattering.

In both of our simulations, the physics library used was "g4em-Livermore" for the score of the ejected spectrum of electrons as for the scoring of the dose deposition in the water phantom that surrounds the irradiated GNP.

Charged Particle Transport.

Unlike photons, charged particles undergo a huge number of collisions (in the order of 10 ^6 for a typical Radio therapy energy range electron) until being absorbed. Therefore, an event-by-event simulation is not practical even on a current computer.

As most interactions lead to a small change in energy and/or direction, it is possible to combine the effect of many small change of these collisions into a single one of large effect (a virtual interaction); this strategy is known as Condensed History (CH) simulation. The probability density function for such large-effect interactions is obtained from multiple scattering theories; as this approach spares time and computing resources, the CH technique is incorporated by all general-purpose MC packages. The CH applies different theories to model the net effect of many successive interactions at a given distance. Groups the minor collisions with small energy losses and deflections consider the discrete simulations of major/catastrophic events. (Dupree.,2012)

The alternative to CH is the Track Structure Monte Carlo. In this, every interaction event is simulated, accounting for a detailed history of the particle's trajectory. It is commonly used in particle transport simulation on microscopic scales and is prohibitive computation time for macroscopic simulations (e.g., patient dimensions). This is implemented in microdosimetry models as the Geant4-DNA project, in which further advances and adaptations of the general

purpose Geant4 Monte Carlo toolkit had been performed for the simulation of the interactions of radiation with biological systems at cellular and DNA level in an energy range (eV – a few 100 MeV)

These models are valid for liquid water medium only; they include elastic scattering, excitation (electronic + vibrations), ionizations, and charge exchange. The cross-section data are generated by purely analytical methods or using interpolation, and all the interactions are explicitly simulated. The energy is deposited at the end of each simulation step.

Atomic deexcitation is initiated by other electromagnetic processes, e.g., photo-electric effect, Compton, ionization by e- and ions, leaving the atom in an excited state. Therefore, atomic deexcitation is compatible with Standard and Low Energy electromagnetic physics categories (Mantero et al.,2011). *The EADL data provide* the transition probabilities for radiative: fluorescence and non-radiative: Auger electrons: initial and final vacancies in different sub-shells and Coster-Kronig electrons: identical sub-shells.

The production cuts for secondaries are specified as range cuts. The ones that are converted at initialization time into energy thresholds for secondary gamma, electron, positron, and proton production. A default value for the range cut is set and can be easily modified to better describe the de-excitation processes, generating a more CPU-intensive simulation.

In the simulation, to obtain the ejected spectrum of electrons from the nanoparticle, the modifications implemented were: turning on the Auger, Auger cascade, and fluorescence process. Ignore the deexcitation cut and set a range cut for all particles. Also, the physics module used to propagate the particles was selected. The complete control document and the parameters that we use to run our simulations are presented in the following section of this appendix.

In the same section, we set some TOPAS overall control parameters among the principal ones, the number of threads used to run the simulation, the seed of random numbers used to run the simulation (each seed provides a different set of random numbers allowing a completely different evolution of the initial particles in the irradiation beam). We also keep a record of the CPU time spent in running each simulation.

Geometrical components and material composition.

The geometry defines the components where the particles will be transported *and establish* the elements and materials. Each geometry component is defined by *shape*, location, and composition. A global volume known as "World" is used as the absolute reference system.

The World is a box with default dimensions in the order of meters; we resize the World to a few nm to match the scale of our system of interest, a visualization of the placement of the different components is presented in Figure1. App1. The material composition of the World was set to vacuum. The center of the rectangular coordinate system is located in the center of the World. The location of whichever other object in the World will be done with respect to this coordinate origin.

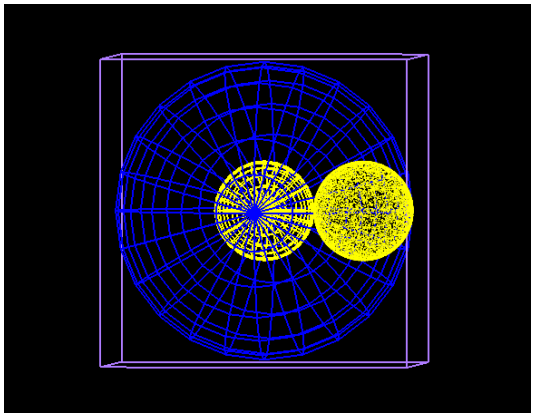

Figure 1. App 1. Geometrical components of the simulation performed to obtain the phase space of ejected electrons from the GNP. The white box is the World, the blue meshed sphere is the water phantom, and the yellow spheres are GNPs.

Simulation to obtain the phase space.

A second object, a sphere of water, was placed in the center of the world to mimic the water-like tissue. All the components maintain a parent-child hierarchy; therefore, when defining that a geometrical object is the parent of another (the child), the location of the last is described concerning the parent. Each geometrical component has three translation and three rotation parameters. These give the position of the component in the coordinate system of its parent component; in this case, the parent is the World and the child the water sphere. Due to the symmetry of our system, the rotation and change of position of the components were not necessary. In the center of the water sphere, we locate the GNP. The molecular composition of the

water and gold was adopted as the predefined values by TOPAS with natural isotope abundance from the NIST database.

Simulation to obtain the dose deposition.

To simulate the propagation of the phase space of ejected electrons, a spherical water phantom with *a radius of* 3.19 µm was located in the center of the world (whose size was increased to be a box of 6.4 µm side). In this case, no GNP was simulated.

The water sphere was split virtually into concentric spherical shells assigned to "parallel world". Such components can superimpose the mass world and can be used for scoring without having an effect on physics. Eighteen of such 1nm spherical shells were defined to score the dose deposition across the water phantom.

Beam location and spectral components.

In this section of the control document, we define the initial set of (primary) particles to be transported (Phase space, Beam, isotropic source). TOPAS allows the use of several sources, but we adopt a planar beam source in our system. By default, the source is centered in the associated geometrical component (the world in this case). The beam position was translated to start on the surface of the GNP, and no beam rotation was required due to the system's symmetry.

Simulation to obtain the phase space.

A flat source with a circular shape matching radius of the nanoparticle was defined. The emitted particle by the source were monoenergetic photons in the case of (10, 30, 100, and 662 keV) or poly-energetic in the case of (150 and 250 kVp). In both cases, the angular distribution was deactivated to have a beam propagating directly toward the GNP. The number of primary particles was also set in this section; we selected the maximum number of primaries to run each simulation.

Simulation to obtain the dose deposition.

In this simulation, the irradiation source was the phase space of ejected electrons scored in the first simulation. When the software source is a phase space, it starts a set of particles from the saved positions, with the recorder particle type (in our case, electrons), momentum, and energy. It is possible to evolve only a part of the phase space, but we replay the whole scored phase space in this case.

Scorers' definition.

In this segment, we defined how the information is accumulated and scored for analysis. The qualities susceptible to being scored include energy deposition, dose, fluence, etc. Each volume in the geometry can be associated with a scorer, and any surface of a given volume can be used for surface scoring.

Simulation to obtain the phase space.

In the first part of the simulations, we defined a surface scorer that collects the information of the ejected electrons from the nanoparticle in the form of phase space. We save the phase space in ASCII format and set the option to record the creator process of the electrons and the vertex information (information about the initial kinetic energy, position, and momentum of the electron at the creation point).

When we save a phase space, a surface is defined, and the position, particle type, energy, and momentum of some or all particles (in our case, all electrons) crossing that surface are saved. The output of the scorer is two files a .header file that tells the number of histories (events recorded), the number of saved particles, and the order of information in the other file (the .phsp file). The .phsp file contains all the saved particles' details (data).

We save the phase space in ASCII format; this provides particle information in an easy-to-read simple text file, in which the data are encoded as a series of columns of text. The header file tells the contents and column order per particle. (The binary format is also available and recommended in case the ASCII format produces a large file).

Ten quantities were scored for each particle: X position, Y position, Z position, U (direction cosine of momentum with respect to X), V (direction cosine of momentum with respect to Y), Energy in MeV, Weight, Particle ID, Flag to tell if Third Direction Cosine is Negative (1 means true)
and a Flag to tell if this is the First Scored Particle from this History (1 means true). It is important to note that the positions are reported relative to the center of coordinates (the World center).

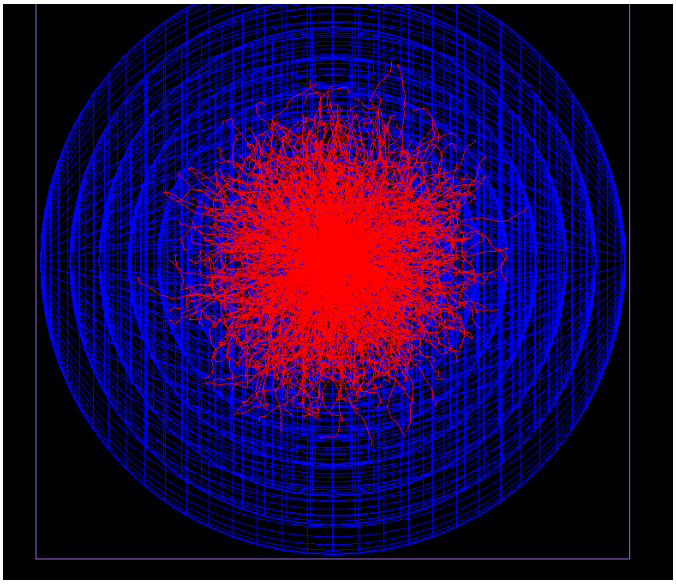

Figure 2. App 1. Geometrical components of the simulation performed to obtain the dose deposition in the water phantom. The white box is the World; the blue meshed concentric spheres are the parallel volumes that divide the water phantom, and the red tracks are the evolution of the electrons in the phantom after being created in the locations reported by the phase space.

Simulation to obtain the dose deposition.

Each one of the spherical shells defined in the parallel world and placed overlaying the water sphere was defined as a scorer. The dose to medium in the 1nm thick shells was the scored quantity and recorded the sum, mean, variance, and standard deviation of the dose to medium. A visualization of the simulation is provided in *Figure 2. App 1*

Visualization.

As the graphics can be the slowest part of a simulation, we disabled it when we *ran* the whole simulation. We use the visualization in trials with a small number of primary particles to check the objects' placement, the beams' orientation, and that the particles evolve in the phantom. The visualization parameters we set are presented in the following section of examples of the control document.

1.3 Executed simulations to obtain the results used in this thesis.

Simulation to obtain the phase space.

The following is an example of the command document (.txt) used in TOPAS to score the Phase space of electrons ejected from an irradiated GNP. The information that follows a (#) are commentaries to understand the selected parameters. To have a complete description of each one of the parameters defined, we recommend that the reader check the documentation of TOPAS.

```
#Physics List Modifications
b:Ph/Default/Auger = "True" # Set to true to turn on Auger
b:Ph/Default/AugerCascade = "True" # Set to true to turn on AugerCascade
b:Ph/Default/DeexcitationIgnoreCut = "True" # Set to true to implement DeexcitationIgnoreCut
b:Ph/Default/Fluorescence = "True"
b:Ph/listProcesses = "True"
i:Ts/NumberOfThreads = 0
i:Ts/ShowHistoryCountAtInterval = 1000
i:Ts/Seed = 1
i:Ts/RunVerbosity = 1
b:Ts/ShowCPUTime = "True"
d:Ph/Default/CutForAllParticles = 0.01 nm # single range cut to use for all particles
sv:Ph/Default/Modules = 1 "g4em-livermore"

#The World Volume
s:Ge/World/Type="TsBox"
s:Ge/World/Material="Vacuum"
d:Ge/World/HLX= 8.5 nm # Half Length
d:Ge/World/HLY= 8.5 nm
d:Ge/World/HLZ= 8.5 nm

#Water Sphere inside the world
s:Ge/MySphere/Parent="World"
s:Ge/MySphere/Type="TsSphere"
s:Ge/MySphere/Material="G4_WATER"
s:Ge/MySphere/Color = "blue"
d:Ge/MySphere/Rmax= 8. nm

#Volume to assess the spectrum (GNP)
s:El/Gold/Symbol="Au"
s:Ge/ParticleCounter/Material = "G4_Au"
s:Ge/Phantom/Parent = "MySphere"
```

s:Ge/Phantom/Type= "TsSphere"

s:Ge/Phantom/Material="G4_Au"

s:Ge/Phantom/Color = "yellow"

d:Ge/Phantom/Rmax = 5 nm

#Beam Position

s:Ge/BeamPosition/Parent="World"

s:Ge/BeamPosition/Type="Group"

d:Ge/BeamPosition/TransX= 0. m

d:Ge/BeamPosition/TransY=0. m

d:Ge/BeamPosition/TransZ= -5 nm

d:Ge/BeamPosition/RotX= 0. deg

d:Ge/BeamPosition/RotY= 0. deg

d:Ge/BeamPosition/RotZ= 0. deg

#Beam

s:So/Default/Type = "Beam"

s:So/Default/Component = "BeamPosition"

s:So/Default/BeamParticle = "gamma"

d:So/Default/BeamEnergy = 100.0 keV

u:So/Default/BeamEnergySpread = 0.

s:So/Default/BeamPositionDistribution = "Flat"

s:So/Default/BeamPositionCutoffShape = "Ellipse"

d:So/Default/BeamPositionCutoffX = 5. nm

d:So/Default/BeamPositionCutoffY = 5. nm

d:So/Default/BeamPositionSpreadX = 0.1 nm

d:So/Default/BeamPositionSpreadY = 0.1 nm

s:So/Default/BeamAngularDistribution = "None" # Flat or Gaussian

d:So/Default/BeamAngularCutoffX = 90. deg

d:So/Default/BeamAngularCutoffY = 90. deg

d:So/Default/BeamAngularSpreadX = 0.0032 rad

d:So/Default/BeamAngularSpreadY = 0.0032 rad

i:So/Default/NumberOfHistoriesInRun = 800000000

#Scoring Spectrum of ejected e- from NP

s:Sc/PSpace/Surface="Phantom/OuterCurvedSurface"

s:Sc/PSpace/Quantity = "PhaseSpace"

s:Sc/PSpace/OutputType = "ASCII"

s:Sc/PSpace/IfOutputFileAlreadyExists = "Overwrite"

sv:Sc/PSpace/OnlyIncludeParticlesNamed = 1 "e-"

b:Sc/PSpace/IncludeCreatorProcess="True"

b:Sc/PSpace/IncludeVertexInfo = "True" # Initial KE, Position and Momentum
sv:Sc/PSpace/OnlyIncludeIfParticleOrAncestorInteractedInVolume = 1 "Phantom"
s:Sc/PSpace/OnlyIncludeParticlesGoing = "out"
s:Sc/PSpace/OutputFile = "Spectrum"
b:Sc/PSpace/OutputToConsole = "True"

#Visualization
s:Gr/ViewA/Type = "OpenGL"
i:Gr/ViewA/WindowSizeX = 800
i:Gr/ViewA/WindowSizeY = 800
u:Gr/ViewA/Zoom = 2.
Ts/PauseBeforeQuit = "True"
b:Gr/Enable = "False"

Simulation to obtain the dose deposition.

The following is an example of the command document (.txt) used in TOPAS to score the dose deposited in the water phantom by the ejected electrons scaping the GNP. We clarify that to save some space, only two of the 18 spherical shells in the parallel world (and the corresponding scorer) are defined in the example.

#Physics List Modifications
b:Ph/Default/Auger="True" #Turn on Auger
b:Ph/listProcesses = "True"
i:Ts/ShowHistoryCountAtInterval = 1000
i:Ts/RunVerbosity = 1
i:Ts/NumberOfThreads = 0
i:Ts/Seed = 1
b:Ts/ShowCPUTime = "True"
sv:Ph/Default/Modules = 1 "g4em-livermore"

#The World Volume
s:Ge/World/Type="TsBox"
s:Ge/World/Material="Vacuum"
d:Ge/World/HLX= 102.0 nm # Half Length
d:Ge/World/HLY= 102.0 nm
d:Ge/World/HLZ= 102.0 nm

 # Water Sphere inside the world
s:Ge/MySphere/Parent="World"
s:Ge/MySphere/Type="TsSphere"
s:Ge/MySphere/Material="G4_WATER"

s:Ge/MySphere/Color = "blue"

d:Ge/MySphere/Rmax= 101.0 nm

i:Ge/MySphere/RBins= 1

 # Spherical Shells in the parallel world

s:Ge/ScoringSphere5/Type = "TsSphere"

s:Ge/ScoringSphere5/Parent = "World"

b:Ge/ScoringSphere5/IsParallel = "TRUE"

d:Ge/ScoringSphere5/RMin = 5 nm

d:Ge/ScoringSphere5/RMax = 6 nm

i:Ge/ScoringSphere5/RBins = 1

s:Ge/ScoringSphere7/Type = "TsSphere"

s:Ge/ScoringSphere7/Parent = "World"

b:Ge/ScoringSphere7/IsParallel = "TRUE"

d:Ge/ScoringSphere7/RMin = 7 nm

d:Ge/ScoringSphere7/RMax = 8 nm

i:Ge/ScoringSphere7/RBins = 1

#Phase Space Source

s:So/MySource/Type = "PhaseSpace"

s:So/MySource/Component = "World"

s:So/MySource/PhaseSpaceFileName = "Spectrum"

 # Scoring 5 nm

s:Sc/DoseDepAtPhantom5/Quantity = "DoseToMedium"

s:Sc/DoseDepAtPhantom5/Component="ScoringSphere5"

i:Sc/DoseDepAtPhantom5/RBins= 1

s:Sc/DoseDepAtPhantom5/OutputFile = "5"

s:Sc/DoseDepAtPhantom5/IfOutputFileAlreadyExists = "Overwrite"

sv:Sc/DoseDepAtPhantom5/Report = 4 "Sum" "Mean" "Variance" "Standard_Deviation"

#Visualization

s:Gr/ViewA/Type = "OpenGL"

i:Gr/ViewA/WindowSizeX = 800

i:Gr/ViewA/WindowSizeY = 800

u:Gr/ViewA/Zoom = 2.

Ts/PauseBeforeQuit = "True"

b:Gr/Enable = "False"